THE LUNAR POLAR REGIONS: ILLUMINATION ENVIRONMENT, SEASONAL WATER CYCLE AND EXOSPHERIC VOLATILE DELIVERY

JACOB L. KLOOS

A DISSERTATION SUBMITTED TO

THE FACULTY OF GRADUATE STUDIES

IN PARTIAL FULFILMENT OF THE REQUIREMENTS

FOR THE DEGREE OF

DOCTOR OF PHILOSOPHY

GRADUATE PROGRAM IN EARTH AND SPACE SCIENCES AND ENGINEERING

YORK UNIVERSITY

TORONTO, ONTARIO

January 2021

Abstract

Permanently shadowed regions (PSRs) at the lunar poles are of unique interest for science and exploration due to their low surface temperatures and potential for volatile sequestration. Spacecraft have indicated the presence of water ice and other volatiles compounds within these locations, yet questions remain as to their stability, abundance and distribution; broadly, this thesis will seek to advance understanding in all three of these areas. First, we examine the spatial, temporal and spectral variability of the diffuse sources of light that reach PSRs. Through development of a comprehensive scattering model, we show that scattered sunlight is the dominant PSR illumination source at visible and IR wavelengths, and that it contributes a considerable supply (up to 35 μW m^2) of far ultraviolet photons as well. The latter finding is significant because the enhanced flux of high energy scattered solar photons to the PSRs, which has previously not been considered, suggests a higher rate of photodesorption and lower adsorption residence times for water molecules than previously proposed. In the second half of this thesis, we apply numerical techniques to explore the seasonal variations in the surface volatile densities and infall into PSR craters. Here, we show that the growth and decay of seasonal shadow throughout the year enforce distinct patterns in the pole-ward migration of water as well as a cyclical variation in the polar surface hydration. As well, we find that northern hemisphere PSRs accumulate more water per unit area than southern hemisphere PSRs. Due to its relatively long lifetime against photolysis, CO_2 is shown to have the largest infall rate of the species examined, where surface concentrations near the poles exceed 2000$\times$ the strength of the source. Using meteoritic supply rates and estimates of thermal and non-thermal loss rates, we show that net deposition of CO_2 and H_2O may be ongoing process within some of the coldest PSR locations. Assuming the meteoritic supply rate to be constant over time, we calculate that up to 1.5×10^{10} g of meteoritic CO_2 would be trapped over a 2 billion year timescale, most of which would reside at the lunar south pole.

Dedication

For Jill, who has shared this journey with me in a way that no one else has.

Acknowledgements

I would first and foremost like to give my sincere gratitude to my supervisor, Dr. John Moores. Looking back on the last 6 years, it is hard to conceive of a person better suited to guide me through the wild worlds of academia and planetary science. I have always admired his unwavering enthusiasm and dedication to his students, and the care and earnestness with which he approaches his work as a scientist and an educator. He has truly been an exceptional supervisor, and I will always be grateful to him for his mentorship.

Second, I would like to thank Dr. Mike Daly and Dr. Isaac Smith for serving as members of my Supervisory Committee for four (long) years. Throughout my degree they have continually provided useful feedback in a constructive and supportive way. I am grateful to them for all of the useful advice and discussions during the REC meetings, and for their time spent reading my reports and listening to my talks. I would also like to thank the other members of my examining committee, Dr. Barbara Cohen and Dr. Michael De Robertis, for taking time out of their busy schedules to take part in my defense.

I would next like to give a special acknowledgement to Dr. Mark Gordon, who, despite undoubtedly having one of the busiest schedules, very kindly accepted my request to serve on my defense committee. I am very grateful to him for this, and for all of the support and feedback that he has given me during my time at York. Of all the courses I have had the opportunity of taking during my graduate and undergraduate career, I consider his course on cloud physics to be one of my favorites.

Next, I would like to say thank you to Dr. Norbert Schorghofer. I have had the great pleasure of working with Norbert on several of the projects discussed in this thesis, and I can say with the utmost certainty that his involvement, with his mastery of planetary physics, has significantly enhanced the quality of these works. It has been a sincere privilege to work alongside such an esteemed scientist, and I will consider myself lucky to someday have made half the contribution to lunar and planetary science that he has made.

To all the PVL members, past and present, thank you for your support and encouragement. I hope the years ahead will be filled with fruitful collaborations, or, at the very least, catching up at conferences and reminiscing about "the good ole days" at PVL.

Last but not least, to my partner Jill, thank you for existing. Our adventures in Toronto, our treks through the mountains and jungles, the ensuing discussions about our lives beyond grad school - these meant everything to me, and provided all the force I needed to keep going. I am so extraordinarily lucky to have you at my side.

Contents

List of Tables

List of Figures

1 Introduction

This thesis is an exploration of the north and south polar regions of the Moon, where volatiles, notably H_2O water ice, are thought to reside (Urey, 1952). Due to the Moon's near-perpendicular spin-axis relative to the ecliptic plane ($< 1.59°$), the floors of some polar impact craters have been shielded from the Sun for over ~2 billion years (Siegler et al., 2015; Ward, 1975) and, in the absence of direct radiative heating, are among the coldest locations in the solar system (Paige et al., 2010). In theory, the persistently low surface temperatures of these areas, referred to as permanently shadowed regions (PSRs), enable them to preserve water and, if sufficiently cold, other volatile compounds over geologic periods of time. Within the last several decades, a multitude of theoretical, laboratory and observational studies have been carried out in an effort to characterize the existence and nature of volatiles within these areas (Arnold, 1979; Colaprete et al., 2010; Gladstone et al., 2012; Hayne et al., 2015; Li et al., 2018; Watson, Murray, & Brown, 1961). While these efforts have largely affirmed the early predictions of water and other ices on the Moon (Urey, 1952), key questions remain unknown regarding the age, form, composition, abundance, distribution and origin of these ice reservoirs.

Interest in lunar volatile ices centers around their utility for science and exploration. As for science, the accumulation of water and other ices over billion-year timescales within concentrated areas would provide a unique record of endogenic and exogenic volatile sources. Detailed study of these ices may shed light on the delivery and retention of water and other volatiles to the inner solar system – and to the Earth-Moon system in particular. Beyond their intellectual value, ice deposits, should they be accessible and present in operationally useful quantities, would be an important resource for sustaining a human presence on the Moon: water ice could be used as a supply of potable drinking water and/or be broken down and used to manufacture breathable air for future human explorers. Additionally, water mined from PSRs could be disassociated into its constituent elements and used as a rocket propellant; the ability to "refuel" rockets on the Moon would help to make transport in the solar system more economically viable. In order to advance these scientific- and exploration-related goals, however, it is necessary to better constrain the bulk quantity, accessibility and spatial and depth distribution of ice reservoirs.

Since lunar PSRs were first theorized to exist nearly 70 years ago (Urey, 1952), much has been learned about their unique thermal environment and capacity for volatile preservation (Lawrence, 2017, and references therein). Following the Apollo missions and laboratory analysis of the returned samples, it was generally concluded that the Moon was anhydrous (Taylor, 1975), yet subsequent studies and observations would later begin to challenge this view. In the late 90's, the Lunar Prospector spacecraft mapped the global hydrogen abundance in the near subsurface and observed enhanced hydrogen at high latitudes near the north and south pole (Feldman et al., 2000; Feldman et al., 1998; Feldman et al., 2001). Assuming this hydrogen is in the form of H_2O ice, Feldman et al. (1998) estimated that up to 3×10^{15}g (3×10^{9}t) of water could be buried at each pole in the upper 2 meters of the surface. Targeting permanently shadowed craters, orbital reflectance spectroscopic measurements from a collection of spacecraft have indicated that some of this ice is exposed at the surface, with measured surficial concentrations in the range of 0-30% wt (Fisher et al., 2017; Gladstone et al., 2010; Hayne et al., 2015; Li et al., 2018). Ground truth to these data has been obtained at one location (Cabeus Crater; 85.3° S, 42.1° W) by the Lunar Crater Observation and Sensing Satellite (LCROSS) impact experiment, which observed 5.5% H_2O in the impact ejecta plume in addition to other cometary volatiles in smaller quantities. Whether or not the observed LCROSS composition is representative of other surface and subsurface PSR locations, however, has yet to be determined, as there are a number of processes operating within PSRs that may lead to heterogeneities in volatile composition, abundance and distribution. A complete review of the available studies will be given in Chapter 2.

The tantalizing evidence of ice on the Moon has spurred further interest in orbital and surface *in-situ* exploration. Indeed, lunar PSRs remain priority science targets in the search for extraterrestrial water, with a number of upcoming missions, both funded and planned, dedicated to their exploration (Cohen et al., 2015; Colaprete et al., 2019; Kruzelecky et al., 2018). Important to the current and future exploration of these areas is knowledge of the illumination environment in and around areas of permanent shadow. Due to the absence of direct solar photons available for observing these areas, PSRs present difficult targets for study. A low-cost, low-power approach to observing these areas, future missions could make use of the available sources of faint and diffuse radiation that illuminate PSRs. Among these sources are starlight, Lyman-alpha (Ly-α, 121.6 nm) radiation from the interplanetary medium (IPM) (Gladstone et al., 2010), sunlight scattered from neighboring topography as well as sunlight reflected from the Earth toward the Moon, referred to as Earthshine (Glenar et al., 2019). Understanding these sources and their spatial, temporal and spectral variability may not only be important for instrument design, but would also help to support mission development, operations and data analysis. Furthermore, quantifying these radiation sources is important for understanding the PSR thermal environment, and in turn the potential effects on surficial and sub-surficial volatile compounds. The PSR illumination environment is the subject of Chapter 3.

Critical to interpreting the age and abundance of lunar ices are efficiencies in lateral vapor transport to the polar regions. Theoretical study of this transport process from both endogenic and exogenic sources may help to constrain volatile source rates and depositional trends within PSRs. As will be discussed in further detail in Chapter 2, a large number of numerical simulations have been performed, which have emphasized different aspects of the migration process, including the influence of surface roughness (Prem et al., 2018), fractionation during transport (Butler, 1997; Moores, 2016; Schorghofer, 2014), diurnal variability (Schorghofer, Lucey, & Williams, 2017) and infall within PSRs (Moores, 2016). A parameter generally ignored thus far, however, is the influence of the lunar obliquity with respect to the ecliptic plane and the associated seasonal patterns in migration. Although small, the lunar obliquity produces a semiannual variation in polar cold trapping area, which may have two important implications for lunar volatile studies: (1) seasonal cold traps constitute localized reservoirs where volatiles may be temporarily stored and exchanged with the exosphere; and (2) for a continual supply of water such as production at the surface via solar wind implantation and subsequent oxygenation, the polar surface concentration of H_2O will oscillate throughout the year as the trapping area expands and recedes. In Chapter 5 we employ an illumination model to assess the seasonal variation and geographic extent of shadowed area at the north and south pole of the Moon (pole-ward of $\pm 80°$). These mapping results are combined with numerical Monte Carlo simulations of vapor transport in order to examine the influence of seasonal shadow on surface migration as well as patterns in deposition within known PSRs in the modern era.

In addition to H_2O, other volatiles have been detected in the exosphere and on the surface. For example, carbon monoxide (CO), carbon dioxide (CO_2) and methane (CH_4) were detected by the Lunar Atmospheric Composition Experiment (LACE) mass spectrometer deployed on the Apollo 17 mission (Stern, 1999), and later from the Lunar Atmosphere and Dust Environment Explorer (LADEE) spacecraft (Benna, Mahaffy, & Hodges, 2014; Hodges Jr, 2016). These compounds were also observed in the LCROSS impact site, in addition to other species such ammonia (NH_3), sulfur dioxide (SO_2) and hydrogen sulfide (H_2S) (Colaprete et al., 2010). The efficiency with which these compounds are transported through the exosphere to the polar regions, however, has not been explored in depth. In Chapter 6, we apply our Monte Carlo model to examine the transport efficiencies of these chemical species. Using Diviner thermal IR data (Williams et al., 2019) and known thermophysical constants, we identify locations within PSRs at the north and south pole where these volatiles are stable against sublimation over long timescales, and quantify the ongoing depositional rates from non-collisional impact sources.

The final chapter, Chapter 7, will investigate the influence of small-scale (μm–mm) roughness on the exospheric velocity distributions. Gas-surface interactions at the scale of regolith grains remains an important yet largely unexplored aspect of exospheric migration. Through grain-to-grain transfers or topographic obstruction, adsorbed particles may make many "hops" before being liberated into the exosphere on a ballistic trajectory. Hopping at these micro scales has consequences for the distribution of velocities of the molecules leaving the regolith, both in terms of the speed and direction of release from the exobase. In addition, roughness effects may have consequences for the efficiency of polar migration and infall to the cold traps, as increasing the number of particle-regolith encounters will increase the probability of finding a high activation energy adsorption grain site or micro cold trap. For thermally accommodated molecules, the launch speed is influenced by the grain temperature, and, as such, the large thermal gradients that exist at small-scales (i.e. Bandfield et al., 2015) will alter the average speeds of molecules in the exosphere. As well, although current exosphere models tend to assume directional uniformity in particle emission, topographic effects – especially at micro scales where roughness is pronounced – should cause non-uniformities in the vertical velocity distribution as particles emitted at large emission angles are more likely to encounter another surface/grain. As will be shown in this work, these roughness effects on the velocity distribution in turn have implications for the near-surface vertical exospheric densities.

2 | Background

2.1 Chapter Overview

This chapter reviews the history of the study of the illumination environment of the lunar polar regions as well as the current understanding of the abundance and distribution of volatiles.

2.2 Characterizing the Moon's Polar Illumination Environment

The prospect of water ice and other volatiles has been a key driver to understand the unique thermal and illumination environment of the Moon's polar regions. Because of the Moon's small axial tilt with respect to the ecliptic plane ($<1.59°$) and its heavily cratered surface, high latitude areas experience extremes in both sunlight and shadow: low elevation surfaces may be continuously shielded from the Sun, while some topographic peaks – in many cases directly adjacent to PSRs – experience sunlight for 80-90% of the year (Gläser et al., 2014; Noda et al., 2008; Speyerer & Robinson, 2013). While PSRs are of interest for their ability to sequester volatiles, areas of prolonged sunlight, sometimes referred to in the literature as *persistently illuminated regions*, are desirable sites for future lunar bases and other solar-powered endeavors.

Initial mapping of PSRs and persistently illuminated regions on the Moon was conducted using visual imagery (250–500 m/pixel resolution) from the Clementine spacecraft (Bussey et al., 2005; Bussey, Spudis, & Robinson, 1999; Nozette et al., 1994; Shoemaker, Robinson, & Eliason, 1994). While these images provided the first glimpse into the unique polar illumination environment and successfully identified a number of permanently shadowed craters, this data set, collected over a 71 day period (∼1/5th of a complete lunar year) during the lunar winter, was significantly limited in its temporal and spatial coverage. Polar altimetry, later acquired through Earth-based radar interferometry, enabled the illumination to be simulated using ray tracing algorithms (Margot et al., 1999). Using these radar-derived digital elevation models (DEMs), binned at a resolution of 150 m/pixel, Margot et al. (1999) modeled the illumination within ∼5° of the poles and identified regions of permanent shadow consistent with Clementine imagery. In addition, these authors found increased PSR area in the southern hemisphere owing to more extreme topography, although the poor viewing geometry at the lunar poles caused a significant fraction of the landscape to be radar-shadowed (particularly farside topography) which prevented a complete assessment of the PSR extent and distribution. The polar orbit of the Selenological and Engineering Explorer (SELENE) spacecraft, launched in 2007 by the Japan Aerospace Exploration Agency, improved the coverage of polar topography with its laser altimeter (LALT) instrument (Araki et al., 2009), allowing for a more thorough characterization of the radiation environment poleward of ±85° (Noda et al., 2008). As well as being limited in spatial coverage, however, the LALT topographic data contained artifacts due to orbital errors that resulted in uncertainties in the illumination modeling.

With the launch of the Lunar Reconnaissance Orbiter (LRO) in 2009 (Chin et al., 2007) and the acquisition of global, high-resolution altimetry from the Lunar Orbiter Laser Altimeter (LOLA) instrument (Smith et al., 2010), the accuracy and geographic coverage of polar illumination modeling was substantially improved. Mazarico et al. (2011) used LOLA topography, binned to 240 m pixel^{-1}, to simulate the polar illumination (pole-ward of ±65°) across multiple lunar precessional cycles (∼18.6 years). The results of this mapping, displayed in Figure 2.1 for regions pole-ward of ±80°, found 12,866 km^2 and 16,055 km^2 of permanently shadowed area at the north and south polar regions, respectively[1]. In addition to containing more total PSR area, the southern polar region contains larger regions of contiguous shadow.

McGovern et al. (2013) utilized higher resolution LOLA topography (100 m/pixel) and extended the geographic coverage to include surfaces pole-ward of ±45°. This study identified PSRs as close to the equator as ±58° latitude, although low-latitude

[1]These estimates were attained by removing PSRs fewer than 8 contiguous pixels due to uncertainties in the illumination modeling.

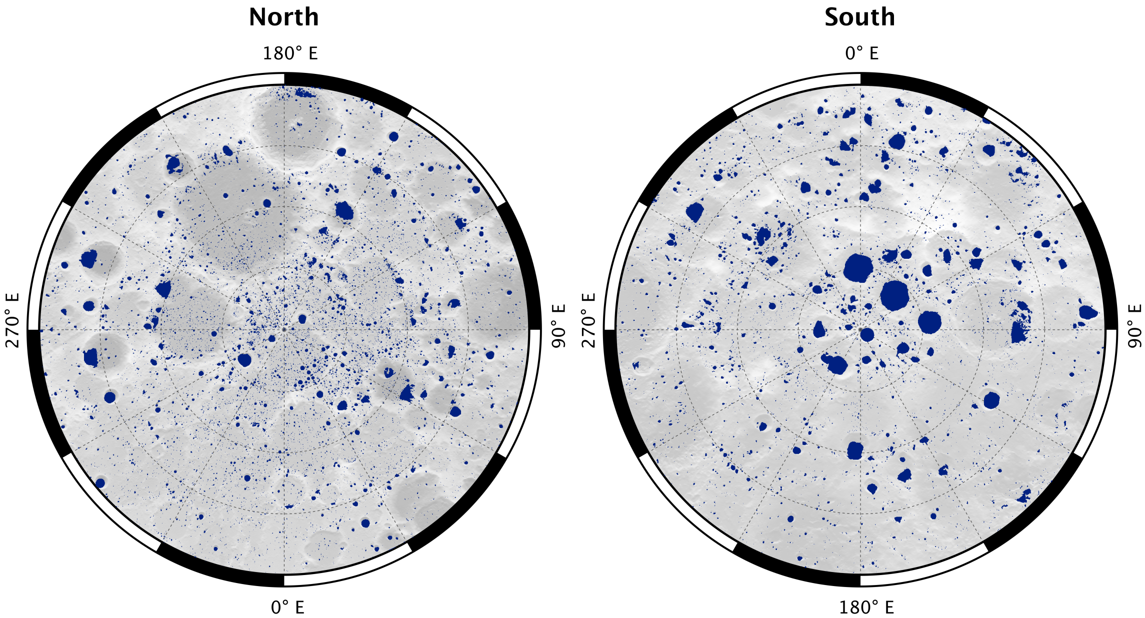

Figure 2.1: Locations of permanent shadow (blue) at the north and south polar regions (poleward of ±80°) of the Moon. Data were taken from Mazarico et al. (2011) and are overlaid on a shaded relief map created using LOLA topography. Lines of latitude are shown every 2.5°.

PSRs are much smaller in size and possess warmer temperatures relative to their high-latitude counterparts. Of course, PSRs are likely to exist at scales below the resolution of the aforementioned studies due to small-scale surface roughness and rock exposures. In fact, at their equatorial landing site (9.0° S, 15.5° E), the Apollo 16 astronauts collected soil samples from a surface estimated to be in permanent shadow due to the presence of a large boulder (nicknamed "Shadow Rock") (Ulrich, Hodges, & Muehlberger, 1981), although topographic data below ∼1m scales and long-period illumination analysis are needed to determine where small-scale, equatorial PSRs could exist. More recently, Hayne, Aharonson, and Schörghofer (2020) have estimated the prevalence of "micro" (i.e. cm-scale) PSRs by simulating the illumination and temperature of Gaussian rough surfaces at a range of polar latitudes, concluding that small-scale shadows may significantly augment the stability regions for H_2O.

Characterization of the radiation environment within PSRs is also valuable for reasons stated in Chapter 1, although few studies have been documented in the literature to date. Using LOLA topography and a simplified scattering model, Mazarico et al. (2011) provided initial estimates of the broadband scattered solar flux reaching a sampling of points within northern and southern hemisphere PSRs. These authors found that all of the selected areas received scattered sunlight, although large disparities in the received flux (about an order of magnitude) were observed between individual craters. More recently, Glenar et al. (2019) characterized the thermal and solar reflectance contributions from Earthshine, and concluded that Earthshine and scattered sunlight were comparable in photon flux. This claim will be examined in greater detail in Chapter 3.

Before proceeding, it is worth briefly noting here that the Moon is not the only body in the solar system known to contain PSRs. Both Mercury (Chabot, Shread, & Harmon, 2018; Deutsch et al., 2016; Slade, Butler, & Muhleman, 1992) and the dwarf planet Ceres (Platz et al., 2016; Schorghofer et al., 2016) possess low obliquities ($\sim 0.03^\circ$ and $\sim 4^\circ$, respectively) and cold, ice-enriched permanently shadowed areas near their poles. PSRs are likely to be found on a myriad of other planetary bodies in the solar system as well, such as asteroids and Kuiper belt objects with low obliquities and topographic relief near the polar regions.

2.3 On the Composition, Abundance and Distribution of Lunar Volatiles

Following the early prediction of ice-enriched PSRs from Urey (1952), the first major theoretical study to examine the details of lunar volatiles was made by Watson, Murray, and Brown (1961). In addition to making estimates of the PSR temperatures and rates of sublimation loss, these authors developed a detailed theory of molecular transport, postulating that the Moon's rarefied atmosphere should permit molecules to move about the surface on ballistic trajectories and accumulate within high latitude cold-traps. Nearly two decades later, Arnold (1979) revived this work and made quantitative estimates on the abundance of water at the lunar poles based on exogenic and endogenic sources (discussed further in section 2.4.1).

The first attempt to detect lunar ice was a bi-static radar experiment carried out in 1994 by the Clementine spacecraft (Nozette et al., 1996; Nozette et al., 1994), where S-band, right-circularly polarized radar signals were transmitted toward the lunar polar regions by the spacecraft and the reflected signals were received at Earth by the Deep Space Network (DSN) antennae. This experiment, performed during 4 orbits at the south pole and 3 orbits at the north pole, found significant enhancement of the circular polarization ratio (CPR) in one of the south polar observations, where the observed enhancement was localized to PSR craters. Within the north polar observations, however, no such CPR enhancement was found. As no single explanation could account for the CPR enhancement at the south pole, a number of possible interpretations were put forth, including the presence of water ice and surface roughness effects. Subsequent radar measurements of the lunar south pole, however, identified a number of radar-enhanced, sunlit impact craters, challenging the interpretation of water ice as the source of the CPR enhancement (Stacy, Campbell, & Ford, 1997).

Following efforts to identify lunar water ice were made using epithermal neutron spectroscopic measurements from the Lunar Prospector spacecraft, which orbited the Moon from January 1998 to July 1999 (Binder, 1998). Operating in a polar orbit, the Lunar Prospector Neutron Spectrometer (LPNS) mapped the global hydrogen abundances in the upper 2-3 m of the surface. From this mapping, neutron suppressions, indicating enhanced hydrogen bearing material, were found at at high latitudes (poleward of $\pm 70°$) (Feldman et al., 1999; Feldman et al., 2000; Feldman et al., 1998). This hydrogen is generally inferred to be in the form of H_2O, although neutron data are unable to determine the chemical form of the hydrogen (only that it is present). The LRO spacecraft also carried a neutron spectrometer – the Lunar Exploration Neutron Detector (LEND) – which performed similar global mapping of the hydrogen abundances and confirmed the polar hydrogen enhancements observed by LPNS (Mitrofanov et al., 2012; Mitrofanov et al., 2010). Unexpectedly, however, the regions of enhanced hydrogen as detected by these instruments were not co-located with cold traps observed in the thermal infrared, excepting one north polar crater (Rozhdestvensky U) and two south polar craters (Shoemaker and Cabeus) (Sanin et al., 2012). One possible explanation put forth for the misalignment between subsurface water and present-day PSRs is the theory of lunar true polar wander, which postulates that the spin axis of the Moon has reoriented from a past position, and that the current distribution of hydrogen is a record from an ancient palaeopole (Siegler et al., 2016). This theory is based on data from the LPNS showing antipodal hydrogen maxima that is offset $\sim 5.5^{\circ}$ from the current spin axis, and assumes that water will preferentially accrete near the instantaneous pole and is capable of migrating beneath the surface to a stable depth.

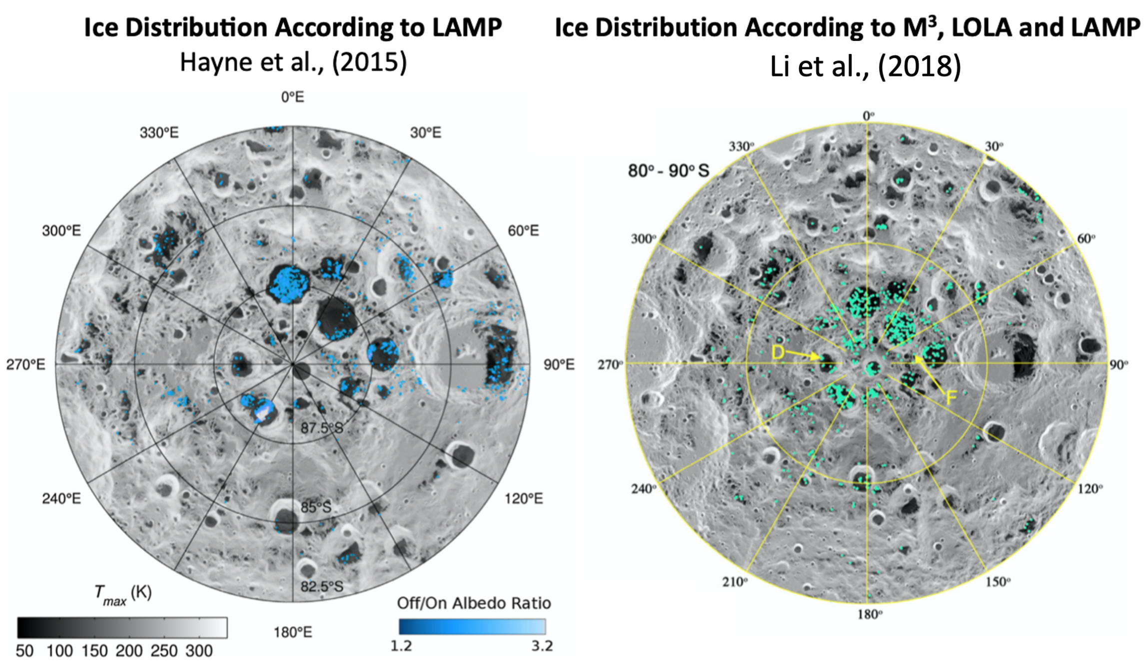

Figure 2.2: Locations of exposed water ice according to Hayne et al. (2015) (left) and Li et al. (2018) (right). In both of these works, Diviner temperatures were used to constrain the data to areas with T_{max}<110 K.

Adding to and in some ways complicating the neutron data are reflectance spectroscopic measurements that report evidence for surface-exposed frost localized within

PSRs. Utilizing IPM Ly-α photons and UV-bright stars as illumination sources, the Lyman Alpha Mapping Project (LAMP) instrument (Gladstone et al., 2010) on LRO has made passive reflectance measurements of lunar PSRs at the south pole[2] at far ultraviolet wavelengths. The LAMP data are consistent with the presence of a patchy distribution of surface ice with concentrations in the range of ~1-10% wt, with the concentration and distribution being strongly governed by temperature (Gladstone et al., 2012; Hayne et al., 2015). A map from Hayne et al. (2015) showing the LRO-LAMP derived ice distribution is provided in Figure 2.2. Active, IR normal albedo measurements at 1,064 nm from the LOLA instrument on LRO have mapped reflectance variations within PSRs in addition to the surrounding sunlit areas, revealing systematically higher reflectivity within PSRs at the south polar region. Like with the LAMP data, temperature-reflectance correlations are observed, with the enhanced LOLA reflections being largely confined to colder PSR locations with T_{max} < 110 K (Fisher et al., 2017; Lucey et al., 2014; Qiao et al., 2019). Spectral observations from the Moon Mineralogy Mapper (M3) instrument on the Chandrayaan-1 lunar orbiter observed larger ice abundances, with reported concentrations up to 30% wt in some locations, although others locations contained no ice signature (Li et al., 2018).

Cameras onboard the SELENE and LRO spacecraft have also succeeded in imaging PSR surfaces while faintly illuminated by diffuse sunlight scattered from the

[2]Due to diminished starlight in the northern ecliptic hemisphere, signal-to-noise ratios of north polar measurements are reduced relative to those in the south (Gladstone et al., 2012). At the time of writing, results from LAMP's north polar observations have not been reported.

nearby topography (Haruyama et al., 2008; Koeber, Robinson, & Speyerer, 2014; Mitchell et al., 2018). From these images, PSR albedo variations can be assessed at optical/NIR wavelengths in order to search for bright, highly reflective ices that are exposed at the surface. Haruyama et al. (2008) presented SELENE panchromatic Terrain Camera images of the permanently shadowed floor of Shackleton crater, which is nearly coincident with the Moon's south pole (89.7° S, 129.8° E) and one of the longest-lived lunar cold-traps (Siegler et al., 2015). Although Shackleton has been observed to be anomalously reflective relative to other nearby craters (Fisher et al., 2017; Zuber et al., 2012), these images did not reveal any conspicuously bright areas indicative of pure water ice deposits. The enhanced brightness of Shackleton has been explained using arguments of mass wasting[3] owing to the steep slopes of its interior walls ($\sim 30°$), yet a small percentage of ice (up to 20%) intimately mixed with the soil cannot be ruled out as a possibility (Haruyama et al., 2008; Zuber et al., 2012). More extensive PSR optical imaging has been performed with the Narrow Angle Cameras (NAC) (Robinson et al., 2010) on LRO (see Figure 2.3). Mitchell et al. (2018) reported on these observations for the north pole along with complementary S-band radar data from the LRO Miniature Radio-Frequency (Mini-RF) instrument. The Mini-RF instrument was used to identify radar-bright PSR craters while the NAC images were used to ascertain whether the enhanced radar backscatter was more likely a result of blockiness within the crater or water ice. Of the four CPR-anomalous craters ex-

[3]Mass wasting is the downslope movement of material due to the gravitational force. The material underneath is generally brighter as it has been less exposed to space weathering.

amined in this study, three craters (Rozhdestvenskiy N, Lovelace E, and Lovelace) contained no observable blocks in their interiors, indicating that water ice may be a reasonable interpretation of the radar signature. The PSR NAC observations will be further discussed in Chapter 4.

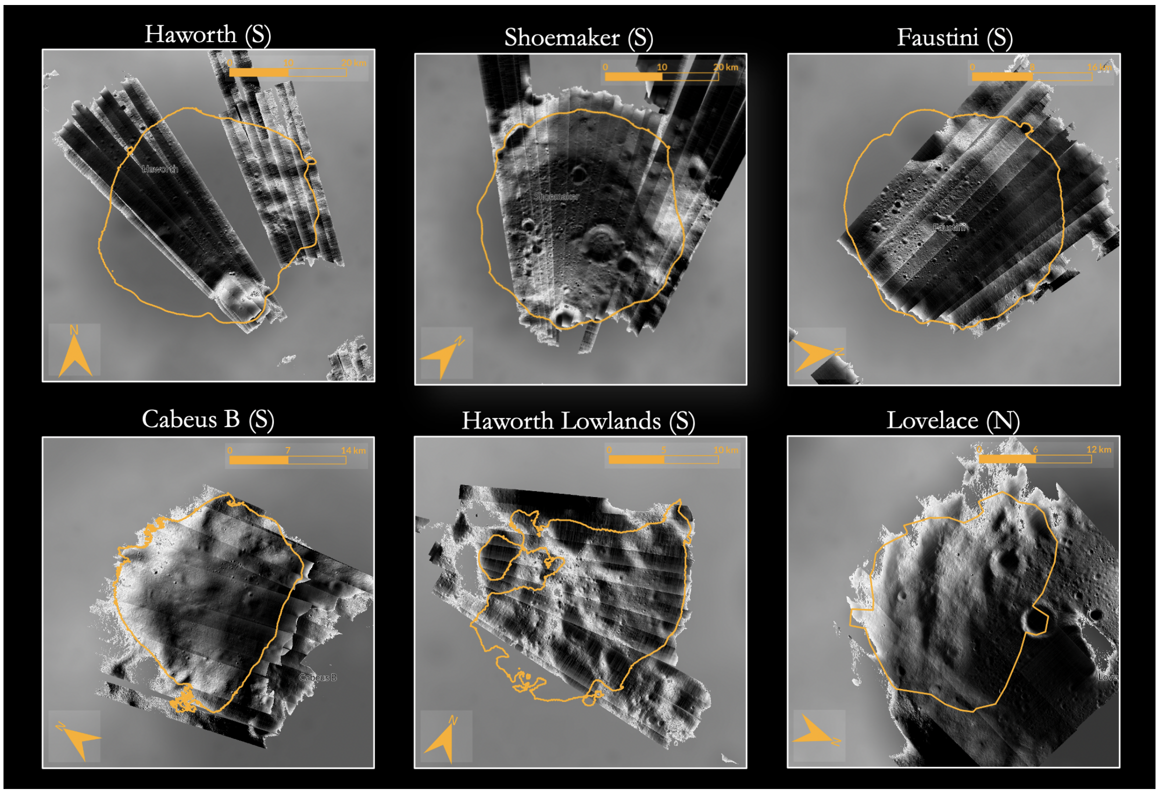

Figure 2.3: Long-exposure Narrow Angle Camera images of selected PSRs. The orange line denotes the PSR boundary as determined by Mazarico et al. (2011). Image Credits: NASA/GSFC/ASU.

Direct evidence of water was provided by the LCROSS impact experiment, which exhumed surface material within Cabeus crater (85.3° S, 42.1° W) down to a depth of 2-3 m. NIR spectral measurements of the impact plume showed the presence of water at a concentration of 5.6 ± 2.9 wt% in addition to other cometary species in lower quantities (Colaprete et al., 2010). A summary of the detected volatiles within the

Table 2.1: Detected volatile within the LCROSS impact plume and their abundances (Colaprete et al., 2010).

Compound	Molecules cm^{-2}	% Relative to H_2O
H_2O	$5.1 \pm 1.4 \times 10^{19}$	100%
H_2S	$8.5 \pm 0.9 \times 10^{18}$	16.75%
NH_3	$3.1 \pm 1.5 \times 10^{18}$	6.03%
SO_2	$1.6 \pm 0.4 \times 10^{18}$	3.19%
C_2H_4	$1.6 \pm 1.7 \times 10^{18}$	3.12%
CO_2	$1.1 \pm 1.0 \times 10^{18}$	2.17%
CH_3OH	$7.8 \pm 42 \times 10^{17}$	1.55%
CH_4	$3.3 \pm 3.0 \times 10^{17}$	0.65%
OH	$1.7 \pm 0.4 \times 10^{16}$	0.03%

LCROSS plume and their reported abundances, taken from Colaprete et al. (2010), is summarized in table 2.1. Beyond the LCROSS data, we currently have very little information about the surficial abundances of non-H_2O volatiles. The only other known study to examine the spectral signature of a volatile other than water was made by Hayne et al. (2019). These authors used LRO-LAMP data to assess the presence of CO_2 within the coldest (T_{max} <55 K) lunar PSRs, and identified Ly-α albedo features consistent with exposed CO_2 at km-scales within Haworth, Faustini and de Gerlache craters.

To summarize, the consensus from the available observational data is that the polar regions of the Moon harbor small, patchy ice deposits exposed at the surface, with concentrations in the range of 1-30% wt (Fisher et al., 2017; Hayne et al., 2015; Li et al., 2018). Larger reservoirs of H_2O are expected in the subsurface (Feldman et al., 1998; Mitrofanov et al., 2012; Rubanenko, Venkatraman, & Paige, 2019), although subsurface deposits are not aligned with cold traps observed in the thermal IR (Sanin et al., 2012). Relative to Mercury, which hosts meters-thick deposits of ice at the polar regions (Chabot, Shread, & Harmon, 2018; Deutsch et al., 2016;

Schorghofer et al., 2016; Slade, Butler, & Muhleman, 1992), the Moon seems relatively depleted in volatiles (Lawrence, 2017). In addition, and crucially, the available lunar remote sensing data sets are not entirely consistent with respect to the abundance and location of water. For example, some data sets (e.g. Li et al. (2018)) indicate up to 30% water ice in Shackleton, Amundsen and Shoemaker craters near the south pole, while others (e.g. Hayne et al., 2015) indicate no ice (see Figure 2.2). These inconsistencies highlight the need for ground truth and for further investigation of these important reservoirs.

2.4 Sources, Transport and Storage of Lunar Volatiles

The abundance, distribution and age of volatile ices within lunar PSRs can ultimately be understood as a synthesis of three equally important, time-varying elements: volatile sources/origins, lateral transport to the polar regions, and storage within cold traps. Here, each of these components is reviewed in turn, with particular attention devoted to transport processes as it is a major subject of this thesis.

2.4.1 Sources

Volatiles within lunar cold traps may derive from a combination of endogenic and exogenic sources, including infall from cometary and meteoritic material, reaction of solar wind particles with minerals in the lunar regolith, and outgassing from the interior. Reviews of these sources can be found in Arnold (1979) and Morgan and

Shemansky (1991).

As is evident in the cratering record, large, volatile-rich bodies such as comets and asteroids have frequently impacted the Moon throughout its history. While comets and asteroids have the potential to deliver large amounts of volatile material (predominantly H_2O and CO_2) to the Moon in a single impact, the frequency with which these impacts have occurred, as well as the impactor mass flux, remain uncertain. Using estimates of size and impact frequency, Arnold (1979) estimated that between 10^{16}–10^{17} g of H_2O would have been delivered to the Moon in the last 2 Ga – the time period over which cold traps have existed (Ward, 1975). Due to their high impact velocities (up to 60 km/s), these impactors uplift a thermally energized plume of material, and much of the volatile material is immediately destroyed through shock heating (Pierazzo & Chyba, 2006). Morgan and Shemansky (1991) estimated that 75% of the plume material would be lost upon impact due to dissociation and direct escape. Ong et al. (2010) used a hydrocode simulation to model the impacts of comets at varying impact speeds to study this parameter on volatile retention. They found that for low impact velocities (5 km s^{-1}), typical for short period comets, nearly all of the water is gravitationally bound, while the inverse was true at high impact velocities (60 km s^{-1}). Integrating over all possible impact speeds, Ong et al. found that 6.5% of the cometary impact material would be retained on the Moon, and estimated that 1.3×10^{14}-10^{15} g of H_2O could have been transported to the polar regions in the last 1 Ga.

A second exogenic source of lunar volatiles is infall from smaller impactors such as micrometeoroids. Unlike cometary impacts which are highly episodic and occur at irregular intervals, micrometeoroid bombardment represents a quasi-steady supply of volatiles as the Earth-Moon system repeatedly pass through micrometeoroid streams, such as the Geminids and Quadrantids. Morgan, Zook, and Potter (1989) and Horanyi and Szalay (2017) estimate a time-averaged mass flux of 57.6 g s^{-1} of meteoritic material impact the Moon, while Morgan and Shemansky (1991) estimate that the H_2O mass fraction of this material is 5%. Using a similar mass estimate, Arnold (1979) proposed that 10^{16} g of water could have been delivered to the surface in the last 2 Ga As with comets, the high impact speeds (20-70 km s^{-1} estimated by Arnold, 1979) of these objects results in rapid loss of at least some, if not a majority (Morgan & Shemansky, 1991), of material via dissociation and gravitational escape. Surviving molecules must be further sustained against photodissociation as they undergo a random walk to the polar cold traps where thermal conditions allow them to persist over long timescales.

The solar wind, composed of charged particles from the Sun, is also thought to act as a source of volatile production. Charged protons from the Sun can become implanted into the lunar regolith on the dayside hemisphere, and some fraction of this hydrogen may bond with oxygen to create water group molecules such OH and H_2O. Once formed, OH/H_2O molecules can be released into the exosphere via thermal desorption or through impact vaporization from micrometeorites and interplanetary dust particles (Benna et al., 2019; Jones et al., 2018). Arnold (1979) estimated that $\sim 10^{17}$ g of H_2O could have been formed via solar wind over the last two billion years.

Finally, a more uncertain source is volatile release from ancient volcanism. Needham and Kring (2017) calculate that the Moon may have experienced peak volcanic outgassing around 3.5 billion years ago, and estimate that up to $\sim 10^{19}$ g of volatiles, including H_2O, CO, CO_2 and S among other species could have been released during this period. They suggest that some fraction of the released material could have been deposited into the permanently shadowed regions, although it is unclear whether PSRs existed on the Moon 3.5 Ga due to instabilities in its obliquity (Ward, 1975).

2.4.2 Exospheric Transport

Transport mechanisms are, of course, necessary for redistributing volatile materials from their point of origin to the polar cold-traps; the manner in which this transport occurs, however, will vary considerably depending on the source. Sufficiently large impactors striking the Moon may generate a transient atmosphere that envelops the lunar globe, wherein atmospheric particle densities may be large enough that gas dynamics are governed by collisions between molecules. Numerical simulations of cometary impacts and transport of the resulting vapor mass have been performed by Stewart et al. (2011), Ong et al. (2010), Prem et al. (2015). These simulations have shown that the transient atmosphere may persist for up to several Earth days (Prem et al., 2015), and, through radiative shielding, may have a protective effect on H_2O

residing within lower layers of the atmosphere. Within the atmosphere, transport to the polar regions occurs primarily as low latitude winds carry material over the day-side. Interestingly, Prem et al. (2015) observed preferential vapor reconvergence near the anitipode of the impact, indicating significantly non-uniform vapor deposition after impact.

In the absence of a transient, collision-induced atmosphere, diffusive molecular transport occurs under different conditions. In the Moon's rarefied atmosphere, technically classified as a surface-bound exosphere, molecular interactions are exceedingly rare, such that atoms and molecules expelled from the surface move independently along ballistic flight paths under a purely gravitational influence (Watson, Murray, & Brown, 1961). If molecules are thermally accommodated with the surface (i.e. achieve thermal equilibrium with the surface), gas-surface interactions are dominated by thermal adsorption and desorption processes. The adsorption residence time, τ, of a molecule in contact with a grain surface is determined principally by the grain temperature, T, and the activation energy of the adsorption site E_a. Langmuir (1916) defined this relationship as:

$$\tau = (1/v_0)\exp\left(E_a/k_B T\right), \tag{2.1}$$

where v_0 is the lattice vibrational frequency of the molecule (on the order of 10^{12} s^{-1}) and k_B is the Boltzmann constant.

Laboratory measurements using lunar regolith analogs have yielded a wide distribution of H_2O activation energies between 0.5 eV and 1.2 eV (Poston et al., 2013), although the majority (>90%) have activation energies below 0.9 eV. Due to its exponential dependence, even relatively small changes in E_a result in large differences in τ. As a demonstration of this, Figure 2.4 plots the adsorption residence time as a function of temperature for $E_a = 0.5$ eV, 0.7 eV and 0.9 eV. As seen here, with $E_a = 0.5$ eV and $T = 200$ K, the residence time of a water molecule is 2 seconds. At the same temperature, using $E_a = 0.7$ eV and $E_a = 0.9$ eV, the residence time is 1 hour and ~700 years, respectively.

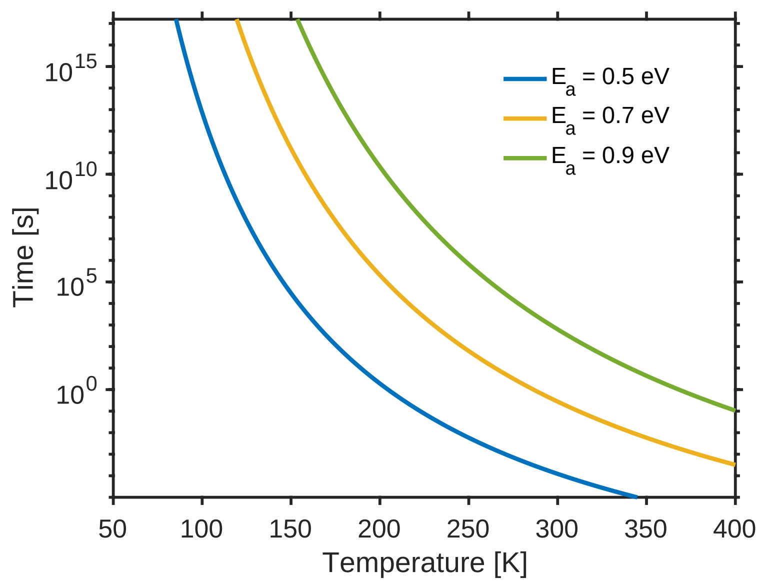

Figure 2.4: H_2O adsorption residence time (τ) as a function of surface temperature and activation energy. The activation energies displayed were selected on the basis of laboratory measurements from Poston et al. (2013).

Figure 2.4 also illustrates the exponential temperature dependence of τ, which has important implications for the mobility of water (and other volatiles) on bodies such as the Moon, where large thermal gradients exist due to its tenuous atmosphere and slow rotation. This is demonstrated in Figure 2.5, which displays longitudinal bolometric temperature profiles at various latitudes using data from the Diviner Lunar Radiometer instrument onboard LRO. Near the equator where sunlight is most direct, daytime temperatures can reach up to ∼400 K, and fall rapidly to ∼100 K during the night as surfaces radiate their heat directly to space. At higher latitudes where the Sun persistently illuminates the surface at high incidence angles, noontime temperatures are reduced to 200–250 K. Topographic and shadowing effects and surface thermo-physical properties may also contribute to thermal gradients at large and small scales (Bandfield et al., 2015), and these thermal gradients will have consequences for molecular residence times.

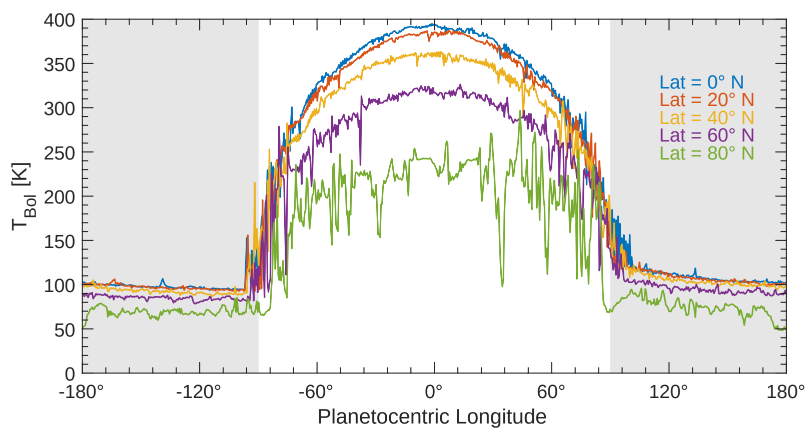

Figure 2.5: Diviner bolometric temperature profiles for selected latitudes at a 0° subsolar longitude. Data represent annual averages and derive from publicly available maps created by Williams et al. (2017). Gray shaded areas denote the nighttime surface regions.

At temperatures characteristic of the lunar dayside, molecules residing on the surface have short residence times ($\tau \sim$ ms) and are quickly thermalized and liberated from the surface. Due to roughness effects, molecules emitted at large zenith angles or entering pore spaces between grains are likely to make several short hops or grain-to-gain transfers before entering the exosphere on a ballistic flight path. Ballistic flights end in adsorption onto a regolith grain at the impact site, where molecules quickly reach thermal equilibrium with the grain and take on the local surface temperature. As a result of the extreme temperatures, molecules hopping on the dayside spend most of their time in the vapor phase (where ballistic flight times may be up to an hour) and little time on the surface. The opposite is true for condensible gasses encountering the nightside hemisphere, where, because of the extreme low temperatures, molecular residence times are long and molecules remain inert throughout the lunar night. They are eventually released into the exosphere at the morning terminator due to rapid heating of the surface. It is also worth noting that release into the exosphere may be caused non-thermal events such photodesorption (Mitchell et al., 2013) and sputtering (Killen & Ip, 1999), and, in these cases, the velocity distribution may differ from a thermally desorbed population.

If thermal accommodation is assumed, molecules are emitted with a speed drawn from a velocity probability distribution that is determined by the local surface temperature. Numerical simulations of exospheric transport have modeled the velocity distribution using both a Maxwell-Boltzmann (Crider & Vondrak, 2000; Moores, 2016; Schorghofer, 2014) and an Armand (Hodges Jr & Mahaffy, 2016; Schorghofer et al., 2017) distribution. In this work, both of these distributions will be considered. A Maxwell-Boltzmann distribution can be written as:

$$P_M(v) = \frac{4s^{3/2}}{\sqrt{\pi}} v^2 e^{-sv^2} \tag{2.2}$$

where v is the velocity and s is given by:

$$s = \frac{\mu}{2RT} \tag{2.3}$$

Here, μ is the molar mass, R = 8.314 J K^{-1} mol^{-1} is the universal gas constant and v is the velocity distribution. Hodges Jr and Mahaffy (2016), however, found a better fit to the vertical Argon distribution using an Armand velocity distribution (Armand, 1977), and argue that this distribution is appropriate for adsorption chemistry when base of the exosphere is a solid body. An Armand distribution is given as:

$$P_A(v) = 2s_A^2 v^3 e^{-s_A v^2} dv \tag{2.4}$$

where s_A is:

$$s_A = \frac{2\mu}{3RT} \tag{2.5}$$

Figure 2.6 juxtaposes these distributions for H_2O at $T = 200$ K. The direction at which the molecule is launched can be treated as a random probability over 2π steradians, weighted by a cosine factor to account for the diminishing spherical grid area approaching the zenith.

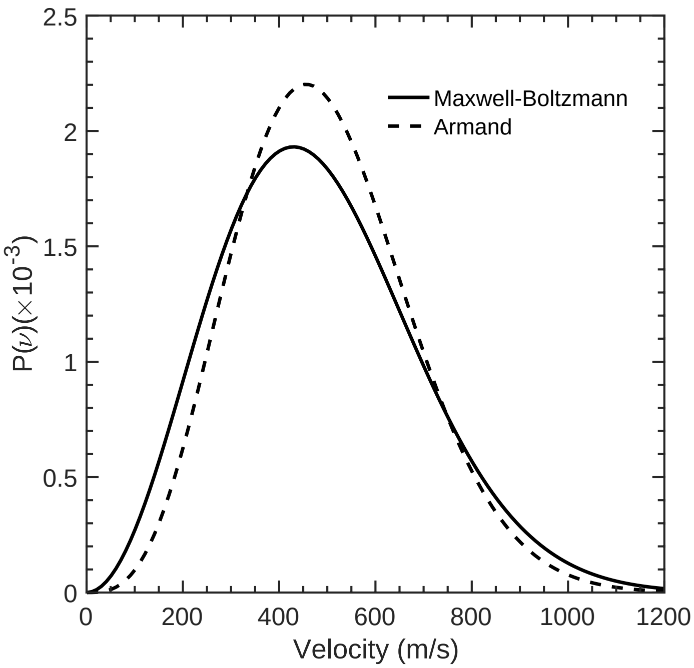

Figure 2.6: Comparison of Maxwell-Boltzmann and Armand velocity probability distributions.

During flight, molecules can be lost or destroyed through one of two mechanisms: (1) through thermal Jeans escape when the launch velocity reaches or exceeds the lunar escape velocity (2,375 m s^{-1}), or (2) through in-flight photodestruction/photoionization through exposure to solar UV photons. Due to its relatively strong gravity, escape is a low probability event on the Moon (Watson, Murray, & Brown, 1961), and only occurs for the very small number of molecules launched at the tail end of the velocity distribution (approximately 1 in 10^6 escape at $T = 400$ K). A significantly higher probability event is destruction through in-flight photodissociation or ionization. During periods of normal Sun activity, H_2O photodissociation occurs at a rate of 1.26×10^{-5} molecules s^{-1} at 1 AU, (Crovisier, 1989). It is worth noting that dissociated products may or may not escape the Moon and be removed from the lunar inventory. If molecules are ionized during flight, charged remnants may be carried along solar electric field lines, and, due to the large solid angle that the Moon subtends for low-altitude molecules, some (50% by some estimates [e.g. Crider and Vondrak (2002), Stern (1999)]) ionized products are likely returned to the Moon and are implanted into the surface at high velocities, releasing sputtering products in turn (Manka & Michel, 1970). Recombination may occur for molecules returned to the surface, and thus not all dissociated/ionized products may be removed from the lunar system (although exospheric models often make this assumption).

Due to their persistently low surface temperatures, molecular residence times within PSRs can be substantial. If temperatures are sufficiently and persistently low, they may effectively act as a permanent sink for exospheric water, and potentially other volatiles too (neglecting non-thermal loss mechanisms). Water vapor delivered to a PSR with $T_{max} < 100$ K would have a minimum residence time of 10^5-10^9 years, and thus these areas are referred to as "cold-traps" for water. Due to differences in their vapor pressures, individual volatile compounds remain stable at different temperatures. Most chemical species of interest on the Moon are *more* volatile than H_2O, and thus require colder temperatures for long-term preservation. This will be discussed in further detail in Chapter 6. Figure 2.7 summarizes the exospheric transport scheme discussed above.

Over the past several decades, a large number of numerical simulations containing

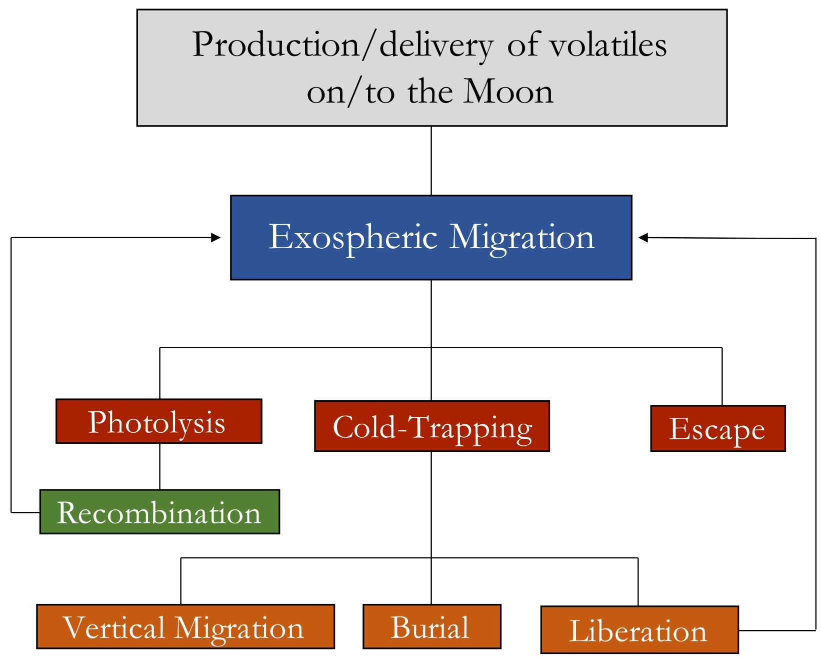

Figure 2.7: Flow diagram showing a simplified transport scheme.

water and other species have been performed using Monte Carlo methods. While differences can be found between existing models, the general approach is the same: source molecules on the surface and track their movement through space and time while monitoring rates of thermal escape, photolysis and cold trap capture. Butler (1997) carried out simulations of H_2O and CO_2 on the Moon and Mercury, concluding that significant fractions (20–50% for H_2O and 13% for CO_2) of both compounds survive transport to the polar cold traps.

Considering the solar wind as a source for the polar hydrogen deposits, Crider and Vondrak (2000) modeled the lateral flow of hydrogen, deuterium (D) and water on the Moon and made estimates of the trapping and loss rates, as well as the D/H fractionation that occurs during transport. Relative to Butler (1997), these authors found a significantly reduced trapping efficiency for water, with only $\sim$4.2% of simulated H_2O cold trapped. Differences in capture rates between these two models may be a result of differences in the source locations, temperature implementation, cold-trap area, or photolysis lifetimes, among other factors.

Schorghofer (2014) examined the diurnal variability of H_2O using a point source of water at the equator. Modeling production as continuous, Schorghofer observed an enhancement in the surface concentration of H_2O at the morning terminator due to the phenomenon of extricated molecules migrating back to the night-hemisphere (only to reemerge again at the morning terminator). Contrary to spacecraft data showing an OH enhancement at *both* terminators (Pieters et al., 2009; Sunshine et al., 2009), no such enhancement occurs at the dawn terminator in numerical simulations (Prem et al., 2018; Schorghofer, 2014; Schorghofer, Lucey, & Williams, 2017). Using a similar exospheric model, Moores (2016) examined the infall of H_2O within a number of large, south polar craters. Moores' results showed that heterogeneous trends in delivery occur as a result of the location (predominantly latitude) of the crater, and that differences in the size-frequency distributions of the PSRs lead to heterogeneous capture rates. Furthermore, both Moores (2016) and Schorghofer (2014) examine the differences in hemispheric capture by displacing the source location of H_2O away from the equator. As the source of water is shifted toward higher latitudes, capture within the hemisphere where the water is sourced becomes increasingly more efficient – and proportionally less efficient in the opposite hemisphere. For example, Schorghofer

(2014) showed that an impact occurring at 45° N would deposit up to three times more water into the northern traps relative to the south.

Other simulations, such as Hurley et al. (2015) and Prem et al. (2018), have examined the influence of surface roughness on volatile transport. Surface roughness is expected to play a significant role in the transport of volatiles through the resulting thermal gradients created at small scales by topographic shadowing effects. Comparing exospheric calculations with and without a surface roughness thermal model, Prem et al. (2018) observed a 4-7% enhancement in PSR capture and an associated reduction in photolysis when roughness effects were accounted for.

Spacecraft observations have reported evidence for the migration of water and/or water-group molecules such as hydroxyl (OH). In 2009, three spacecraft – Deep Impact (Sunshine et al., 2009), Cassini (Clark, 2009), and Chandrayaan-1 (Pieters et al., 2009) – independently observed a global, diurnally variable IR adsorption feature that was attributed to mobile H_2O/OH, although it is important to note that these observations were unable to distinguish between water and hydroxyl. Observations from these three data sets suggest a global surface hydration at a level of 10-1,000 ppm, and, importantly, that the formation and migration of water to the polar cold traps is ongoing. Other orbital data sets have since observed temporally varying hydration features on the lunar surface. FUV spectra from the LRO-LAMP instrument, for example, are consistent with a partial monolayer of water that is thermally adsorbing/desorbing over time (Hendrix et al., 2019). Similar interpretations have been made from LRO-LEND (Livengood et al., 2015) and M^3 (Li & Milliken, 2017; McCord et al., 2011) reflectance spectra.

It is important to note, though, that consensus has not been reached regarding the mobility of water on the lunar surface. Hodges (2002) has argued that lateral transport of H_2O is inefficient due to the high adsorption potentials of soil grains, and that even the largest temperatures on the Moon would not provide enough energy to liberate molecules from their bonds. Instead, water implanted in the regolith could become buried through meteoritic gardening, and/or released through non-thermal events such sputtering or meteoritic bombardment. In this scenario, lateral flow of material to the polar regions may still occur, although molecules would be ejected from the surface with suprathermal kinetic energies, which would significantly increase the probability of escape. This in turn would greatly reduce the transport efficiency relative to the case of thermal ballistic migration where probability of escape is exceedingly low (Watson, Murray, & Brown, 1961). With such inefficient transport, Hodges (2002) proposes that only 3–6% of water accumulated in the regolith may be moved to the polar cold traps, and significant reservoirs of ice are not likely to be found at the lunar polar regions as a result.

2.4.3 Storage

Once arriving within cold traps, molecules exposed to the space environment must survive against a myriad of thermal and non-thermal processes that act to bury, destroy or redistribute volatiles. Beginning with the thermal processes, molecules may vertically migrate to the subsurface through a diffusive process if thermal conditions are favorable (Schorghofer & Taylor, 2007). Schorghofer and Aharonson (2014) showed that water beneath an ice cover, such as that formed through deposition after a comet, may be pumped down into the regolith through diurnal or seasonal temperature cycles. Water buried at depth is expected to have a higher probability of long-term preservation as it is largely protected from space weathering erosional and desorptive processes. Burial through impact gardening, estimated to occur at a rate of 1 m Ga^{-1} (Hurley et al., 2012), provides an additional means for water to reach the subsurface, although if thermal conditions allow for ice mobility, water may migrate to a stable depth and thereby counteract burial (Siegler et al., 2015).

Non-thermal loss mechanisms include plasma sputtering from charged, solar wind particles, and impact vaporization due to micrometeoroid bombardment. Plasma sputtering occurs as energetic solar wind plasma gets deflected into polar craters and ejects surficial materials. Farrell et al. (2019) estimate that the proton flux diverted into a 40-km-diameter polar crater is on the order of $\sim 2\times10^{10}$ protons m^{-2} s^{-1} and for a 1% water ice mixture the resulting sputtering rate is 2.4×10^{-18} kg m^{-2} s^{-1}. A large fraction of the sputtering products will not be sufficiently energized to escape the Moon (Farrell et al., 2019), and will thus land elsewhere on the surface and ballistically migrate through the exosphere. Impact vaporization is a more complex mixture of volatile delivery and removal. Small micrometeoroids and interplanetary dust particles entering PSR craters and impacting ices will vaporize the material and erode the top surface; Cintala (1992) calculated an erosional rate of 7×10^{-16} kg m^{-2} s^{-1} due to micrometeoroid bombardment. Of course, micrometeorites also contain volatile material which is delivered to the lunar surface upon impact, and thus micrometeoroid bombardment is a more complex mixture of source and loss.

Photodesorption via exposure to energetic UV photons may also erode surficial ices and alter their lifetime. Morgan and Shemansky (1991) speculated that incoming Ly-α photons could liberate surface water frost quicker than it could accumulate, assuming only IPM/Starlight as the Ly-α photon source and the continual supply (non-episodic source) of water from micrometeoroids. Based on a constant IPM irradiance of 500 R (1.25×10^{8} photons cm^{-2} s^{-1}), these authors arrived at a monolayer desorption rate of 7×10^{6} molecules cm^{-2} s^{-1}, indicating that an adsorbed H_2O molecule could only survive for $\sim$4 years. Based on a continual supply rate of 0.25×10^{6} molecules cm^{-2} s^{-1} from micrometeoroids, they concluded that a net accumulation of water was not feasible between intervals of large delivery from comets. Using the laboratory-derived photodesorption yield from Westley et al. (1995) and Öberg et al. (2009), along with an assumption of a uniform PSR temperature of 35 K, Gladstone et al. (2012) reported a new desorption rate of 4.4×10^{5} molecules cm^{-2} s^{-1}, concluding that FUV photodesorption is not a severe loss mechanism as was previously thought.

3 The Illumination Conditions within Lunar PSRs

3.1 Chapter Overview

As discussed in Chapter 1 and 2, PSRs are exposed to an array of different illumination sources, including UV and visible starlight, Lyman alpha photons from the interplanetary medium, Earthshine and scattered sunlight; here, these sources are mapped within permanently shadowed regions at the north and south poles of the Moon. The primary goal is to understand how the intensity of these sources vary in space and time, and, furthermore, how they can be used to image PSR surface frost. With the latter goal in mind, we separate the illumination into four spectral bands: three regions of water ice absorption centered at λ_{eff} = 130, 1500 and 2000 nm along with one non-absorption region in the visible at 550 nm. The theoretical work explored here is complementary to the laboratory experiments described in Godin et al. (2020), where a proof of concept frost detection imager is presented which utilizes vis/FUV image ratios to identify the water ice photometric signature.

The text from this chapter is adapted from two publications: Kloos et al. (2020) and Kloos and Moores (2019). J.L.K., the author of this dissertation, developed the illumination models, performed the analysis and drafted the manuscripts. The collaborators on these works – J.E.M., P.J.G., and E.C. – assisted in developing the concepts and ideas for these projects and editing the manuscripts.

3.2 Methods and Data Sets

3.2.1 LOLA Topography and Illumination Modeling of Sunlit Surfaces

To perform the illumination modelling detailed in this work, polar topographic data from the Lunar Orbiter Laser Altimeter (LOLA) instrument are used. LOLA operates using a Q-switched Nd:YAG laser at 1064-nm and is designed to make high-resolution measurements of topography, surface reflectance and surface roughness (Smith et al., 2010). The orbit of LRO has enabled global, geodetically-precise maps of the aforementioned measurements to be acquired, with improved polar coverage relative to previous laser altimeters that have flown to the Moon. Shown in Figure 3.1 are the publicly available gridded polar digital elevation models (DEMs) used in this work. These maps contain binned, interpolated altimetric data where the surface elevation given is relative to the Moon's radius of 1737.4 km. Each uses a polar stereographic

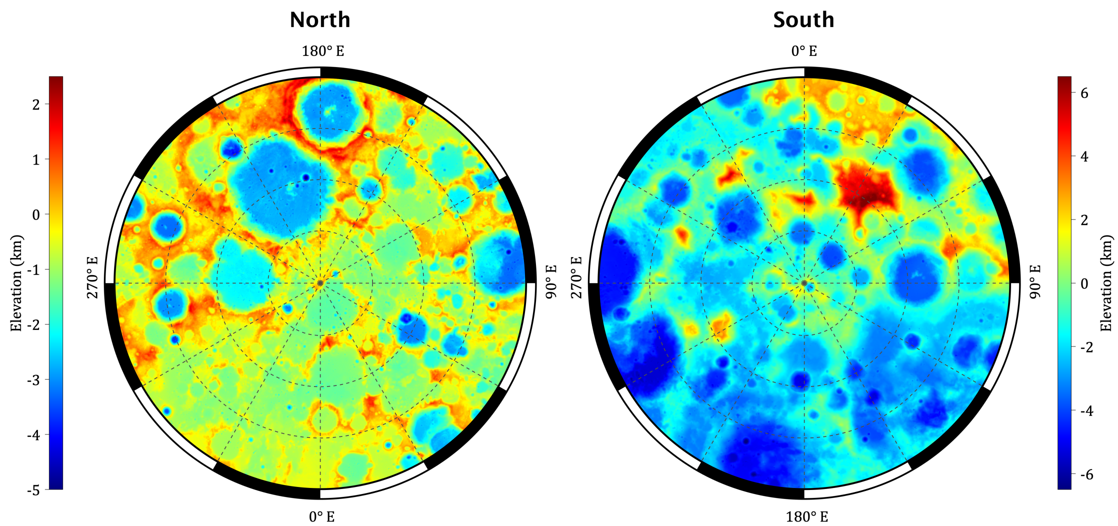

Figure 3.1: LOLA digital elevation models using polar stereographic projection for the north (left) and south (right) pole of the Moon. The color axis corresponds to the elevation (in km) of the surface relative to a sphere of 1737.4 km in radius. Each map is centered at the pole and has a 240-m-per-pixel resolution (true at the pole). Lines of latitude are shown every 2.5° with the outermost line representing 80°. Note that the scale of the color axis differs for the north and south pole.

projection (true at the pole) at 240-m-per-pixel resolution and extends to a latitude of ±75°, thereby encompassing the large polar craters containing PSRs (Mazarico et al., 2011; McGovern et al., 2013). A resolution of 240-m was selected as a compromise between accuracy and computational speed.

From LOLA altimetry, the bi-directional slope and slope orientation (also referred to as slope azimuthal angle or slope aspect) of individual topographic facets can be derived using simple geometric relationships. Displayed in Figures 3.2 and 3.3 are 240-m baseline polar stereographic maps of the surface slope and slope azimuthal angle,

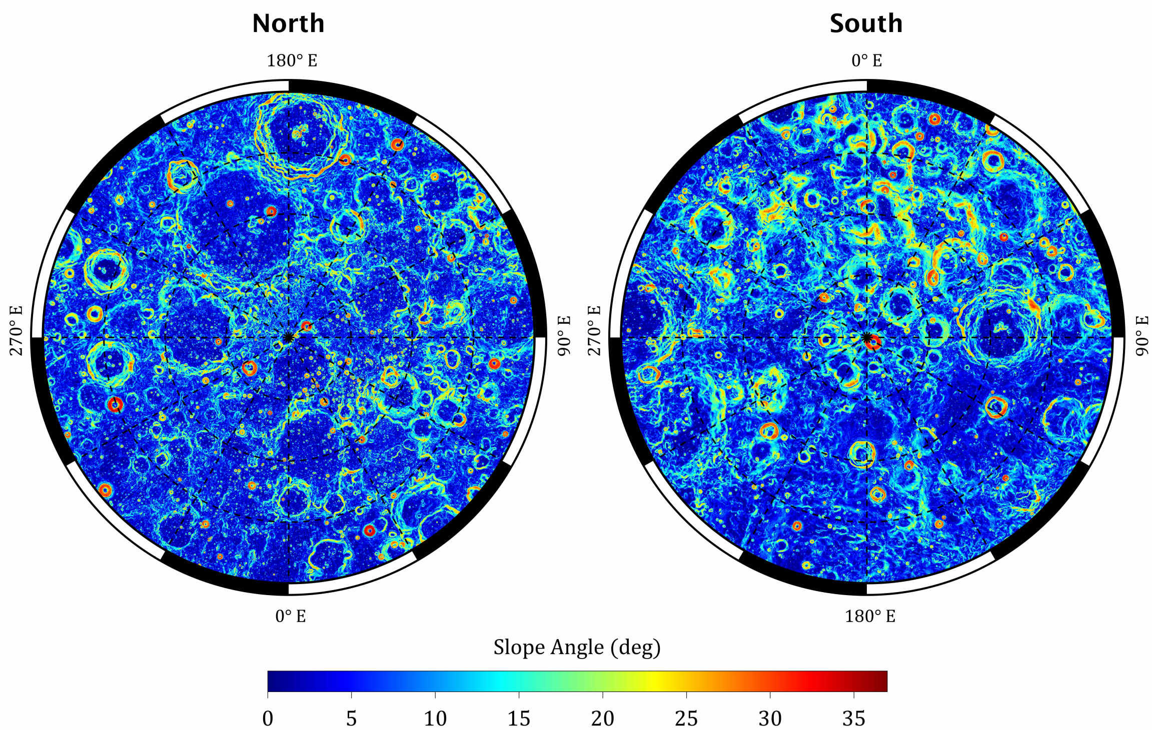

Figure 3.2: 240-m baseline bi-directional slope maps derived from LOLA topography.

respectively, which are referenced throughout this work. Bi-directional slope angles may be as large as 37°, or the angle of repose for dry, granular materials on the Moon; slope azimuth angle, defined to be the slope's angular deviation in degrees from the pole-facing direction, varies between 0° and 360°, where 0° indicates a pole-oriented slope and 180° indicates an equator-oriented slope.

To determine the region of sky visible for an individual facet (defined here as one pixel of the DEM or a 240 × 240m region of the lunar surface), the horizon method is employed. This technique has been used by other researchers (e.g. Gläser et al. (2014), Mazarico et al. (2011)), and is more computationally efficient than ray-tracing when examining long timescales given that repeated calculations are not

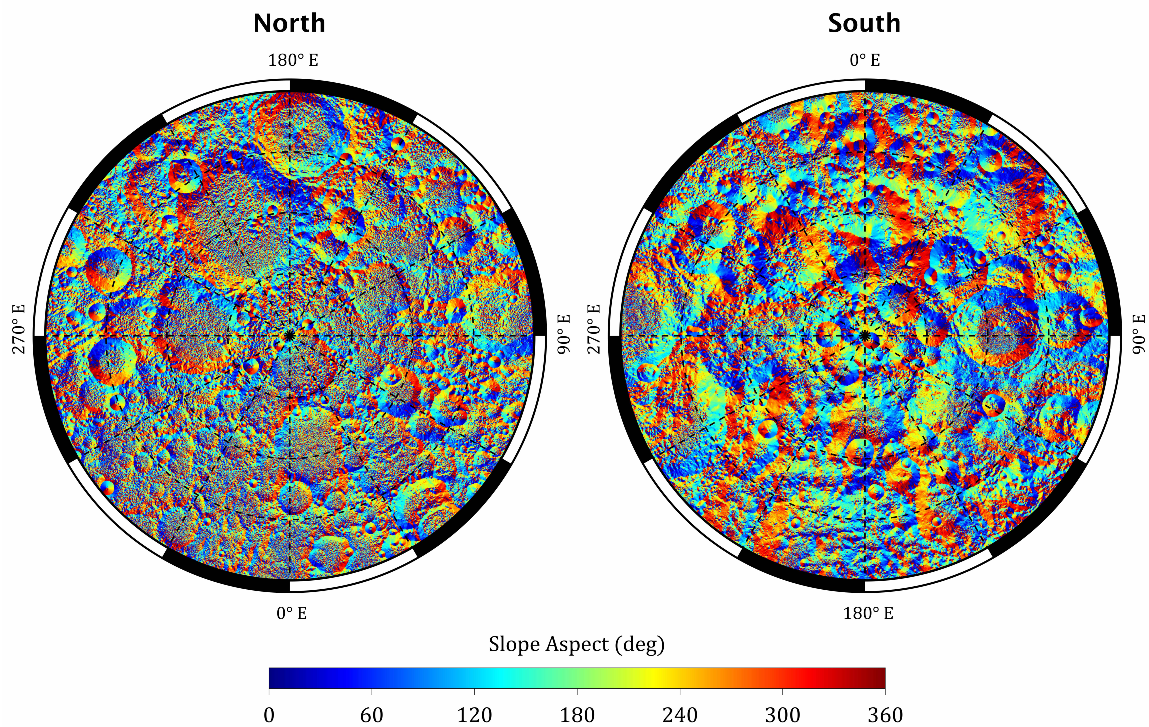

Figure 3.3: 240-m baseline slope azimuthal angle maps derived from LOLA topography. 0° indicates a pole-oriented slope and 180° indicates an equator-oriented slope.

needed at each time step. For each surface element, the elevation of the local horizon is determined for 360° of azimuth using a 1° step size, and the resulting profiles are stored in a database. Horizon angles are derived using vector geometry and account for the curvature of the Moon.

Using these horizon profiles, modeling the illumination received at the lunar surface becomes purely a geometric exercise. At a desired time, the subsolar point is computed with respect to a lunar-fixed frame using the DE421 lunar ephemeris (Williams, Boggs, & Folkner, 2008), and the angular size of the Sun's disk is scaled to account for the Sun-Moon deviation from 1 AU. Next, the visible fraction of the solar disk is determined for each facet of the surface by cross-referencing the subsolar latitude with the horizon angle in the azimuthal direction of the Sun, and spatially integrating the portion of the solar disk that lies above the horizon. The received irradiance E [W m^{-2}] can then be determined by considering the slope angle and orientation of the surface, and using the simple relationship:

$$E_\lambda = \frac{\tau F_{0,\lambda}(-\hat{\mathbf{s}} \cdot \hat{\mathbf{n}})}{d^2} = \frac{\tau F_{0,\lambda} \cos{(i)}}{d^2}, \tag{3.1}$$

where τ is the visible fraction of the solar disk, $F_{0,\lambda}$ is the in-band solar flux at 1 AU, $\hat{\mathbf{s}}$ is the solar vector, $\hat{\mathbf{n}}$ is the surface normal vector, d is the Moon-Sun distance in AU, and i is the angle at which the light is incident on the surface, measured from the normal. To illustrate this process, Figure 3.4 shows the model output for the disk fraction and irradiance computations at the south pole for an arbitrarily selected time.

As in previous works (i.e. Gläser et al., 2014; Mazarico et al., 2011), the illumination model was validated using polar imagery from the Narrow Angle and Wide Angle Cameras on LRO. Validation tests were performed by downloading a sampling of images from the Planetary Data System (PDS) and, using the image boundary coordinates and the observation start time provided in the imager header, creating photo-realistic portrayals using the illumination model described above. Visually, these tests showed excellent agreement in terms of the locations of shadowed surfaces and brightness variations due to the illumination geometry. As expected from previ-

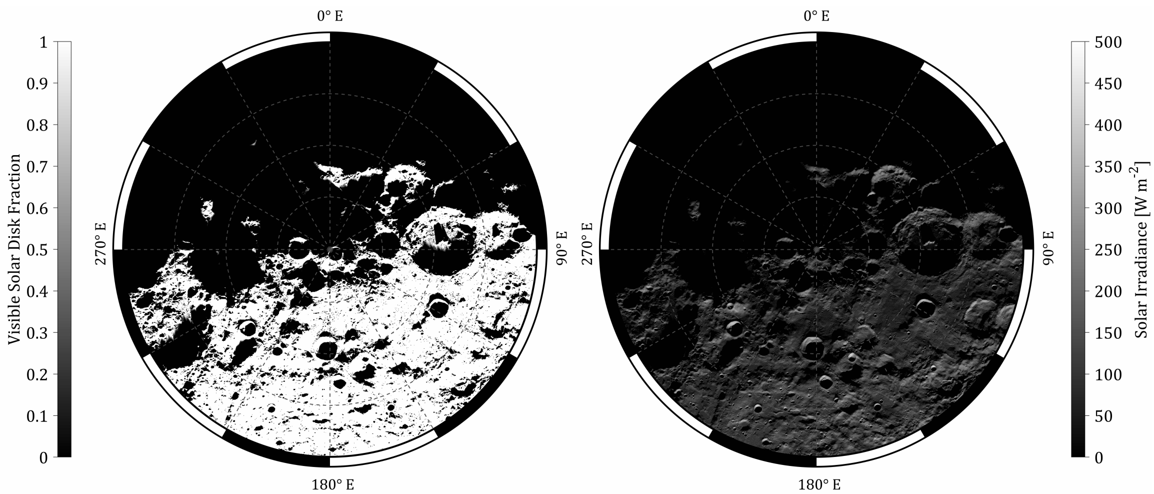

Figure 3.4: Left: map of lunar south pole showing the visible fraction of the solar disk on 29 September 2009 at 08:50:54 UTC. As shown here, the majority of the map appears binary although some regions near shadow-light boundaries are fractional. Right: map of lunar south pole showing the irradiance at the same date and time.

ous analyses (Mazarico et al., 2011), the DEM pixelation results in more pronounced discrepancies at the shadow/illumination boundaries.

3.2.2 Scattered Solar Illumination Model

Increasing the complexity of the model, we now turn to modeling the irradiance received by shadowed surfaces from sunlight that is scattered by nearby topography. Unlike directly illuminated surfaces which predominantly receive light from a single source (the Sun) and from a single direction (assuming the Sun is point source), shadowed surfaces may receive light from multiple directions at once, which significantly complicates the assessment of the energy delivered to these locations. In this section, a model is introduced that is used to quantify the scattered solar flux reaching the permanently shadowed regions of the Moon. Our aim with this work is to understand the relative significance of scattered sunlight relative to other PSR illumination sources (i.e. starlight, IPM Ly-α, Earthshine), and, furthermore, to understand the degree to which crater location, size and shape affect the amount of scattered solar energy delivered to the regions of permanent shadow. Scattered flux is modeled for a variety of craters at the north and south pole ($\pm 10°$ from the rotational pole) containing large, contiguous regions of permanent shadow; Figure 3.5 shows the locations of the PSRs studied while basic information regarding these craters is tabulated in Appendix Table A.1. Although not all of the craters selected display evidence for exposed surface frost in current data (Fisher et al., 2017; Hayne et al., 2015; Li et al., 2018), it is possible that ice may reside in micro cold traps, at scales below the spatial resolution of available remote sensing data. While not detectable from orbit, such ice could be observable with high-resolution *in-situ* studies.

For each crater analyzed, the region of permanent shadow is first isolated within the crater using publicly available PSR polar maps (240 meters-per-pixel resolution) from Mazarico et al. (2011). A line-of-sight calculation is performed between each PSR element and the non-permanently shadowed terrain encircling that element within a 150 km radius. This step is performed in order to determine which areas are capable of contributing singly-scattered sunlight into the PSR, and, furthermore, enhances the computational efficiency of the radiative transfer model by substantially reducing the number of calculations needed at each iteration. A distance of 150 km was selected on the basis of horizon mapping from Mazarico, Barker, and Nicholas

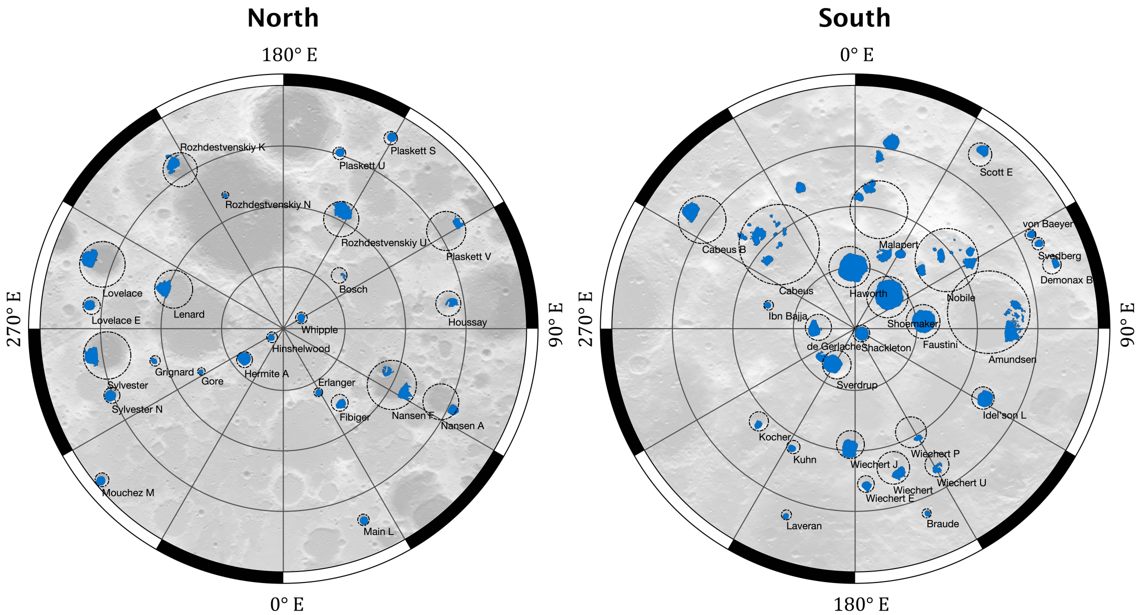

Figure 3.5: Maps of the lunar north and south pole showing the PSR locations analyzed in this study. Blue shaded areas show the locations of permanent shadow as mapped from LOLA topography by Mazarico et al. (2011); black dash-dotted lines outline the craters. Crater latitudes, longitudes and diameters were obtained from the USGS. Note that not all PSRs selected belong to named craters in the Lunar Impact Crater Database. Lines of latitude are shown every 2.5°.

(2018) showing that the maximum horizon distance is typically much closer than 150 km for PSRs (see their Figure 3). The terrain elements within the line-of-sight of at least one PSR element are stored in a database and are referred to in this manuscript as "light scattering terrain." An example of the output of this procedure is shown in Figure 3.6a for Haworth crater (87.4° S, 355.4° E) at the south pole. As it does here, the light scattering terrain can extend beyond the rim of the crater, and may include regional topographic peaks or elevated massifs (Figure 3.6b).

Next, the subsolar point is located with respect to the Moon's principal axis using the DE421 lunar ephemeris. The study period begins at the northern vernal equinox

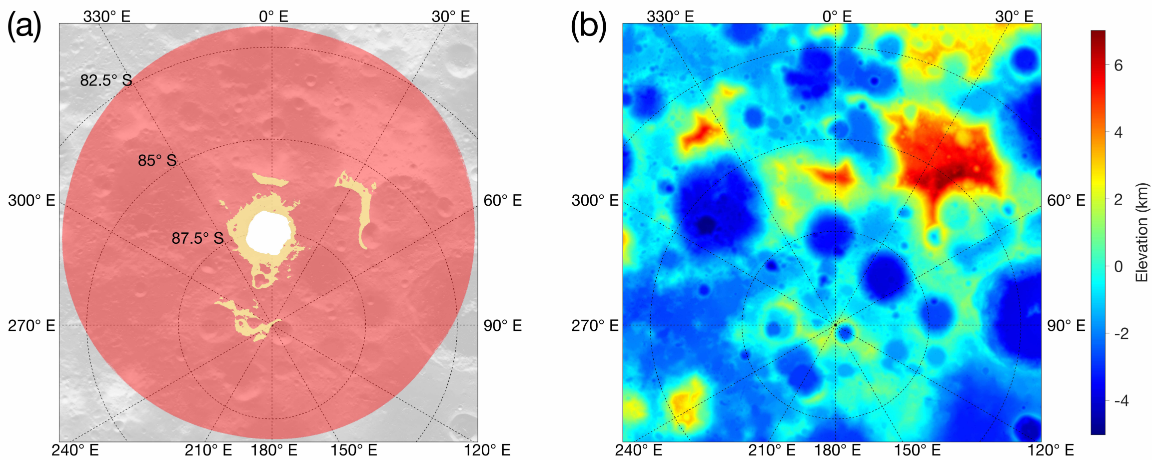

Figure 3.6: (a) Map showing the line-of-sight calculation for Haworth crater. The white region represents the PSR interior to Haworth, red regions represent examined terrain pixels that do not lie within the line of sight of the Haworth PSR while yellow regions represent terrain that lies within the PSR's line-of-sight and may therefore contribute singly-scattered sunlight. (b) Digital elevation model centered on Haworth crater.

on 28 July 2018 and is carried through one draconic year (346.6 Earth days), stepping through time in 48-hr increments. At each temporal iteration, the visible fraction of the solar disk is computed for light scattering elements using the horizon profiles detailed in section 3.2.1. For light scattering elements partially or fully illuminated by the Sun, the line-of-sight is evaluated between the illuminated element and all permanently shadowed terrain pixels comprising the crater. Where a direct line of sight is found, the radiance emitted from the sunlit surface in the direction of the PSR is computed using a Hapke bi-directional reflectance model described below.

The incidence, emission and phase angles, which define the scattering geometry and are needed as inputs to the Hapke model, are computed for each scattering event using slope maps derived from LOLA topography that record the slope angle and

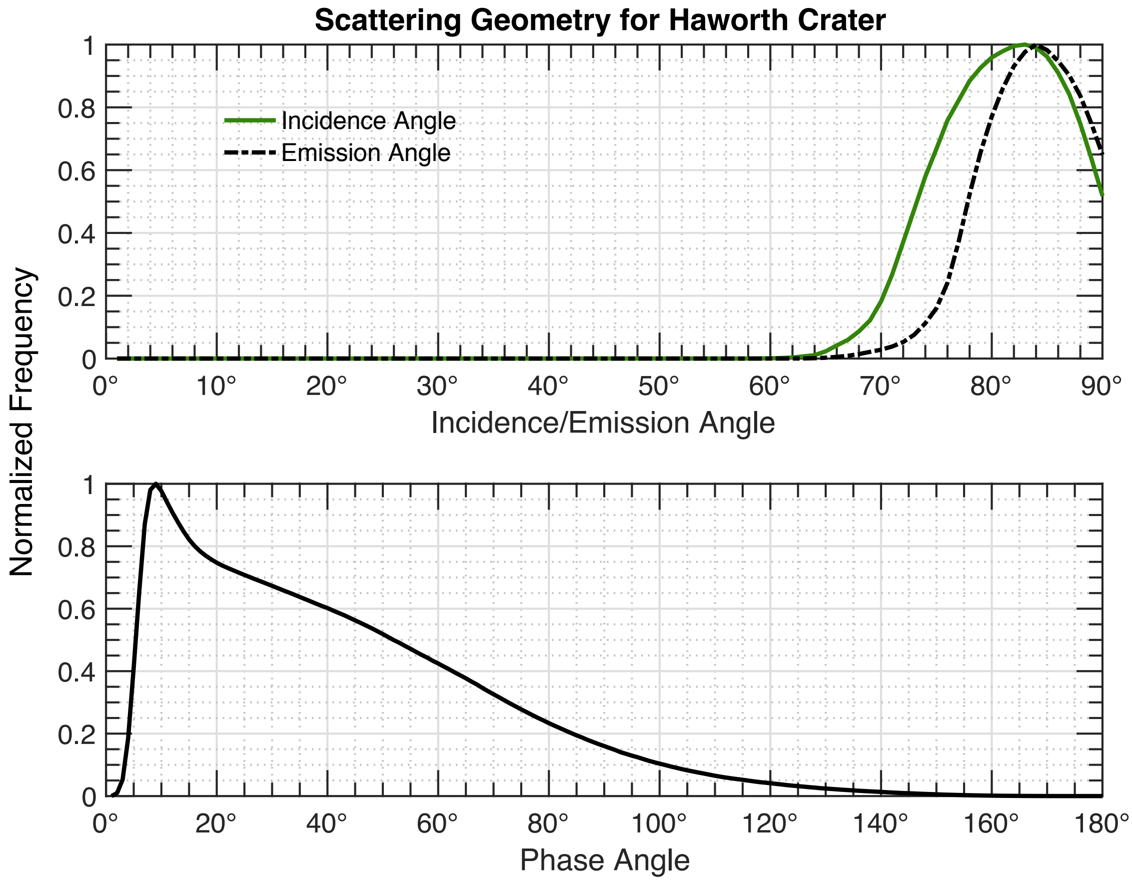

Figure 3.7: Light scattering photometric angles for the PSR area within Haworth crater. Top: histogram of the incidence and emission angles, normalized by the maximum. Emission angles represent the angles at which light is being scattered from the sunlit terrain in the direction of the PSR. Peak incident and emission angles for Haworth are 83° and 84°. Bottom: phase angles normalized by the maximum. Peak phase angle for Haworth is 9°.

aspect of each topographic facet. Incidence and emission angles are measured with respect to the surface normal, while phase angles are defined as the angle between the incidence and emission vectors. These angles are binned in 1° increments and saved as an output at each temporal iteration to provide a contextual background to the illumination results. An example of this output, totalled across the study period, is shown in Figure 3.7 for the Haworth crater PSR, which is found to be characteristic of all craters considered in this study. As seen here, the angles of sunlight incident and emergent on/from light scattering elements are typically large ($> 70°$). Individual craters exhibit a distribution similar to that of Haworth, with peak incidence and emission angles ranging between 74°–88° and 72°–89°, respectively, and an average peak of 82.8° and 83.0°. A wide range of phase angles are encountered in the light scattering geometry, although low phase angles appear dominant, with peak phase angles occurring between 7°–29° and a mean of 14.6°.

The radiance emitted/scattered from the surface is calculated using a Hapke bi-directional reflectance model – a model which is widely used in planetary remote sensing. A brief overview of its relevant aspects is provided here; however, for a full derivation the reader is referred to Hapke (2012) and references therein. The full theoretical Hapke bi-directional reflectance model can be written as

$$r(i, e, \alpha) = K\frac{\omega}{4\pi}\frac{\mu_{0e}}{\mu_{0e} + \mu_e}\{p(\alpha)[1 + B_{S0}B_S(g)] + M(i_e, e_e)\}[1 + B_{C0}B_C(g)]S(i, e, \Psi, \bar{\theta}), \tag{3.2}$$

where $r(i, e, \alpha)$ is the bidirectional reflectance which is given as the ratio of the radiance scattered from the surface in a given direction to the collimated power per unit area incident on the surface; i and e are the angles of incidence and emission measured from the surface normal; α is the phase angle, defined as the angle between the incidence and emission vectors; K is the porosity factor which is in turn dependent on the filling factor ϕ; ω is the volumetric single-scattering albedo; the term $\mu_{0e}/(\mu_{0e} + \mu_e)$ is the Lommel-Seeliger scattering function, where μ_{0e} and μ_e represent the cosine of the effective angles of incidence and emission, respectively, which account for the sub-pixel surface roughness, $\bar{\theta}$; $p(\alpha)$ is the phase function of the scattering grain; B_{S0} is the amplitude of the shadow hiding opposition effect (SHOE); $B_S(g)$ is the angular shape function of the SHOE; $M(i_e, e_e)$ is the isotropic multiple scattering approximation function; B_{C0} is the amplitude of the coherent backscattering opposition effect (CBOE); $B_C(g)$ is the angular shape function of the CBOE; and $S(i, e, \Psi, \bar{\theta})$ is the shadow hiding function where Ψ is the azimuthal angle between the incidence and emission vectors.

The free parameters used in equation 3.2 are colloquially referred to as "Hapke parameters," and together they describe the photometric properties and structure of the lunar regolith. Generally, these parameters are wavelength dependent and are spatially heterogeneous due to regional changes in surface composition, mineralogy, maturity, grain size, compaction state, and surface roughness, among other factors. By combining orbital remote sensing data and mathematical modelling, Hapke photometric parameters have been derived for both lunar mare and highlands terrain in spectral channels ranging from the FUV to the IR (Barker et al., 2016; Kennelly et al., 2010; Liu et al., 2018; Sato et al., 2014). In the work presented here, we utilize these Hapke parameters derived in the FUV (100-160 nm), visible (500-600 nm) and IR (1450-1550 nm and 1950-2050 nm) for highlands material as radar data show that the north and south polar regions are typical of highlands terrain (Spudis et al., 2013); these parameters come from the works of Liu et al. (2018), Sato et al. (2014), and Kennelly et al. (2010), respectively, and are summarized in Table 3.1. Unfortunately, mathematical coupling disallows all of the requisite terms to be constrained, and thus simplifications to the model are made during the data inversion process. For example, the porosity factor K is mathematically coupled to the single scattering albedo ω via the multiple scattering function, and thus cannot be uniquely determined. To reduce the dimensionality, previous authors (e.g. Barker et al. (2016), Kennelly et al. (2010), Liu et al. (2018), Sato et al. (2014)) set $K = 1$, although spacecraft and laboratory reflectance measurements support a somewhat larger porosity of $K = 1.25$ (Hapke & Sato, 2016; Ohtake et al., 2010). To be consistent with these earlier works, a value of $K = 1$ is also used here.

An important aspect of the lunar scattering model is the opposition effect (OE), which is a non-linear increase in the brightness of an object at low phase angles and is attributed to both shadow hiding and coherent backscattering phenomena. Both SHOE and CBOE are wavelength dependent and dominate the OE within different spectral regions (Hapke et al., 2012): As CBOE relies on multiple scattering, it has a relatively small contribution to the OE at UV wavelengths where ω is low, however it plays an increasingly large role at longer wavelengths due to phase reddening; in contrast, SHOE contributes most significantly to the OE in the UV and has a diminishing role at longer wavelengths. Through model fitting, distinguishing between shadow hiding and coherent backscatter opposition effects is difficult as a unique parameter solution cannot be attained. To avoid competing backscatter effects, Sato et al. (2014), who derived Hapke photometric terms using LRO Wide Angle Camera imagery, set $B_{C0} = 0$ in order to constrain the SHOE parameters. In doing so, the evaluated shadow hiding quantities contain a mixture of both coherent and shadow hiding backscatter effects.

Deriving Hapke parameters for the FUV region using LAMP dayside measurements, Liu et al. (2018) set the opposition surge terms (B_{C0} and B_{S0}) equal to 0 due to the lack of low phase angles ($\alpha < 25°$) encountered in their data set. The unique scattering geometry for PSR scattered sunlight, however, does permit the occurrence of low phase angles (Figure 3.7), and therefore accounting for the OE is important. To include its effects in our study for the FUV spectral modeling, we include the SHOE terms B_{S0} and h_S from Sato et al. (2014) for their shortest wavelength measurement: 321 nm. Based on the inverse relationship between wavelength and the shadow hiding amplitude B_{S0} (Hapke et al., 2012), the value at 130 nm is expected to be larger, meaning that FUV irradiance quantities that we report would be conservative estimates. However, although shadow hiding is not expected to contribute significantly at phase angles greater than 20° for large particle size distributions as are found on the Moon (Hapke et al., 2012), it cannot be ruled out that a wide SHOE contributes to the Liu et al. (2018) FUV phase curve behavior. In this case, SHOE may be overcompensated for in our model for scattering events at phase angles $> 25°$ given the inclusion of the Sato et al. (2014) parameters, leading to overestimations in the FUV radiance scattered from sunlit surfaces. In addition, we note that the scattering behavior in the near ultraviolet (at 321 nm), where volume scattering dominates, differs from that in the FUV where surface scattering is dominant, and therefore the mixing of near ultraviolet and FUV photometric parameters may result in additional uncertainties in the modeled FUV quantities. As for CBOE, to be consistent with Sato et al. (2014), we set $B_{C0} = 0$ as B_{S0} contains both coherent backscatter and shadow hiding effects. This assumption is further justified given that CBOE makes a small contribution to the opposition effect in the ultraviolet where ω is small (Hapke et al., 2012).

In the IR, Kennelly et al. (2010) derived Hapke model parameters using observations from the Robotic Lunar Observatory (ROLO) at 1.062 μm and 1.543 μm, among other wavelengths. Best-fit parameter solutions were found by minimizing the χ^2 fit with the lunar scattering model, where conditions were set to exclude solutions with a wide coherent backscatter surge and a narrow shadow hiding surge. Using this method, Kennelly et al. (2010) derive the CBOE and SHOE terms, however they note that the amplitude parameters and the shadow hiding width are only weakly constrained with this approach. Still, these quantities enable the OE to be accounted for in the IR lunar scattering model, although we recognize that uncertainties remain in their true values.

The phase function describes the phase angle dependence of light scattered from

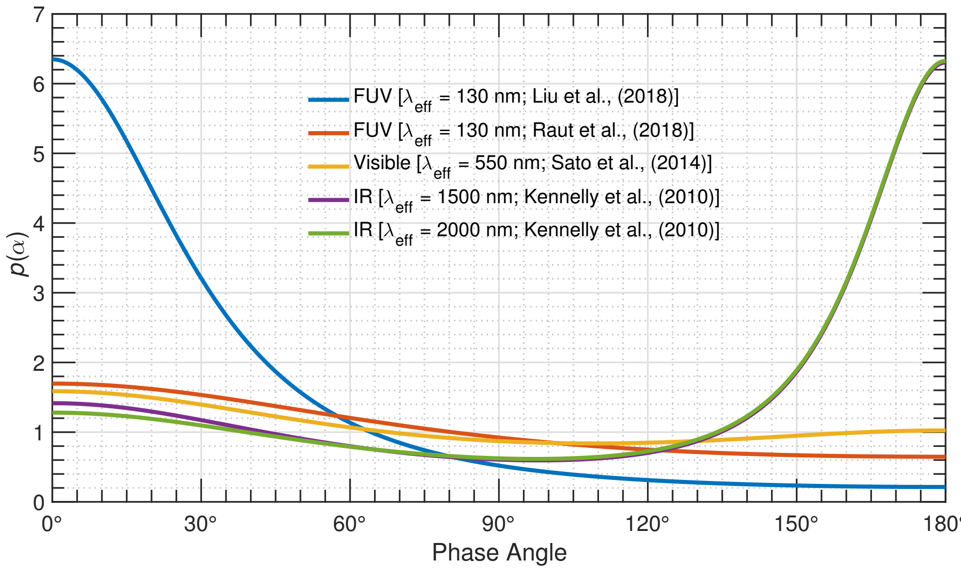

Figure 3.8: Phase function vs. phase angle for the wavelength regimes considered in this study.

regolith grains. A one-term or two-term Henyey-Greenstein (HG) phase function is commonly used to approximate this effect, although the specific type of HG phase function employed varies in the literature. Liu et al. (2018) used a one-term HG phase function given by:

$$p(\alpha) = \frac{1 - g^2}{(1 + 2g\cos(\alpha) + g^2)^{3/2}}, \tag{3.3}$$

where the asymmetry parameter, g ($-1 \leq g \leq 1$) describes the forward or backward scattering nature of the particle: negative values indicate a backward scattering behavior and positive values indicate a forward scattering behavior. Using this formulation, Liu et al. (2018) derive a value of $g = -0.51$ at 134 nm for the highlands terrain, indicating a large backscattering lobe at FUV wavelengths (Figure 3.8), although it should be noted that the phase angles encountered in their data set are generally larger than 25° and thus p for $\alpha < 25°$ was unable to be constrained. Laboratory studies of the FUV photometric properties of Apollo soil 10084 from Raut et al. (2018) utilized a two-term formulation of the HG phase function, which takes the form:

$$p(\alpha) = \frac{1+c}{2}\frac{1-b^2}{(1-2b\cos{(\alpha)}+b^2)^{3/2}} + \frac{1-c}{2}\frac{1-b^2}{(1+2b\cos{(\alpha)}+b^2)^{3/2}}. \tag{3.4}$$

Here, b ($0 \le b \le 1$) is the shape controlling parameter and c ($-1 \le c \le 1$) is the strength of the forward and backward lobes. Raut et al. (2018) derive values of b=0.158 and c=1.08 at 130 nm, suggestive of a subdued FUV backscattering response relative to that reported by Liu et al. (2018) as can be seen in Figure 3.8. The differing scattering behavior reported by these two works could be partly contributed by geographic differences in scattering behavior, as Liu et al. (2018) average data collected over a large range of the lunar surface to derive the photometric parameters while Raut et al. (2018) report on data sampled from a single location (Mare Tranquillitatis). It is also important to point out that laboratory and spacecraft measurements are made under disparate conditions, which may lead to differences in their derived quantities. Sato et al. (2014) also use the two-term formulation in equation 3.4, deriving values of b=0.24 and c=0.35 near 550 nm. A third formulation is employed by Helfenstein, Veverka, and Hillier (1997) and Kennelly et al. (2010), which is a linear

Table 3.1: Hapke photometric parameters used in this study. These values were derived from the works of Liu et al. (2018), Sato et al. (2014), and Kennelly et al. (2010) for the UV, visible, and IR regimes, respectively. These bands were selected for their ability to be used to distinguish frost from lunar regolith. Note that the porosity factor K=1 and the surface roughness $\bar{\theta} = 23.4°$ have been omitted from this table as they are assumed wavelength-independent.

Parameter	**UV (100-160 nm)**	**Visible (500-600 nm)**	**IR (1450–1550 nm)**	**IR (1950-2050 nm)**
ω	0.087	0.35	0.66	0.71
g	-0.51	N/A	N/A	N/A
b	N/A	0.24	N/A	N/A
c	N/A	0.35	N/A	N/A
g_1	N/A	N/A	-0.28	-0.25
B_{S0}	2.4	1.75	0.70	0.70
h_S	0.08	0.08	0.15	0.15
B_{C0}	0	0	0.50	0.40
h_C	0	0	0.04	0.05

combination of two 1-term HG phase functions, and is given by:

$$p(\alpha) = \frac{(1-f)(1-g_1^2)}{(1+2g_1\cos(\alpha)+g_1^2)^{3/2}} + \frac{f(1-g_2^2)}{(1+2g_2\cos(\alpha)+g_2^2)^{3/2}}. \tag{3.5}$$

Following Hillier, Buratti, and Hill (1999) and Helfenstein, Veverka, and Hillier (1997), Kennelly et al. (2010) used constant values of $f = 0.45$ and $g_2 = 0.65$, and derived g_1 which controls the backward scattering lobe. As shown in Figure 3.8, the values derived indicate a preferentially forward scattering surface at IR wavelengths. In this work, we use the formulation for $p(\alpha)$ employed by Liu et al. (2018), Sato et al. (2014) and Kennelly et al. (2010) for the FUV, visible and IR bands, respectively. For the FUV specifically, we also model scattered sunlight using the phase function terms of Raut et al. (2018) for selected craters in order to show the uncertainty in the FUV modeling due to this parameter.

The radiance, I_λ, scattered from the crater wall is given by

$$I_\lambda(i, e, \alpha) = \tau F_{0,\lambda} r(i, e, \alpha), \tag{3.6}$$

where τ is the fraction of the Sun's disk illuminated from the vantage point of the light scattering pixel and $F_{0,\lambda}$ is the incident in-band solar flux. For the visible and IR bands, $F_{0,\lambda}$ is obtained using the solar spectral distribution at 1 AU provided by the American Society for Testing Materials (ASTM), referred to as the ASTM G-173 spectra. For the FUV band, $F_{0,\lambda}$ is obtained by integrating the FUV spectrum acquired by SORCE SOLSTICE (Rottman, Woods, & Sparn, 1993) at the ephemeris time nearest to that of the model execution. SORCE FUV spectra are acquired daily in the 115–180 nm spectral range (1 nm resolution) at a mean solar distance of 1 AU, and have a reported accuracy between 2–6% (McClintock, Rottman, & Woods, 2000). An example of the SORCE FUV spectrum is provided in Figure 3.9a, and 3.9b shows the integrated SORCE SOLSTICE FUV flux over an 11-year solar cycle, where the gray shaded region denotes the one year study period considered in this work. While the FUV solar output does not vary significantly across this interval, it is evident that the study period selected represents a solar minimum; the implications of this will be further discussed in section 3.3.3. In all cases, $F_{0,\lambda}$ is scaled to account for the deviation of the Moon-Sun distance from 1 AU.

Finally, the irradiance, $E_{p,\lambda}$, received by a single PSR element can be written as

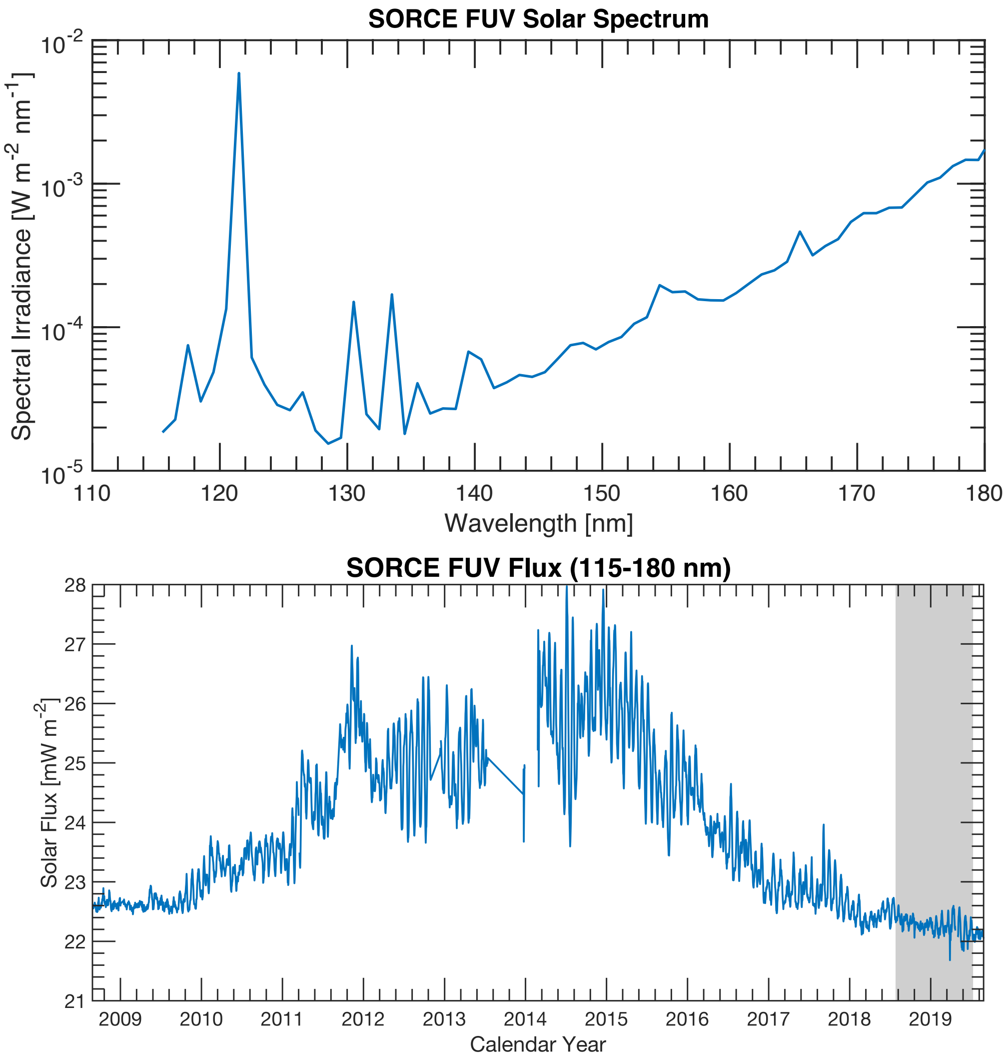

Figure 3.9: FUV solar flux measured by SORCE SOLSTICE over an 11-year solar cycle. The gray shaded region denotes the study period examined in this work.

$$E_{p,\lambda} = \sum_{n=1}^{N} I_{\lambda,n} \Omega_n \cos{(i_{p,n})}, \tag{3.7}$$

where N is the number of light scattering elements for the PSR, Ω_n is the projected solid angle of the light scattering element with respect to the PSR element (corrected for map distortion), and $i_{p,n}$ is the incidence angle of scattered sunlight measured from the PSR surface normal.

3.2.3 Earthshine

To model the Earthshine flux reaching lunar PSRs at visible and IR wavelengths, we rely on Earthshine solar reflectance spectra from Glenar et al. (2019), reproduced in Figure 3.10. Shown here are hemispherically averaged reflectance spectra for two near-fully illuminated ($> 99\%$) hemispheres: one comprised primarily of ocean and one with more significant land coverage[1]. Using an average of these two extremes, the broadband solar flux reflected from the fully-illuminated Earth toward the Moon is $\sim$62 mW m^{-2} at the average Earth-Moon distance (384,400 km); separating this into the visible and IR channels, we obtain upper limits of $F_{e,550} = 9.5$, $F_{e,1550} = 0.63$ and $F_{e,1950} = 0.11$ mW m^{-2}. With these quantities, modeling Earthshine within lunar PSRs is, in principal, similar to evaluating the irradiance of a surface *directly illuminated* by the Sun (Equation 3.1), with the added complexity of determining the phase of the Earth from a lunar vantage point.

The illumination received by the Earth is modeled using a pixelized sphere created with a HEALPix scheme, where each of the 12,288 grid faces is represented with an equal area. The day/night hemispheres of Earth are modelled at each time step using the terrestrial subsolar latitude and longitude, obtained using the DE421 ephemeris (Williams, Boggs, & Folkner, 2008); the Earth's disk as seen from an observer at one

[1] In both cases, cloud reflectance contributes to the spectra, although the fractional cloud coverage at the time the spectra were acquired is not known. Differences in Earthshine due to cloud coverage, however, will not significantly alter the conclusions in this work.

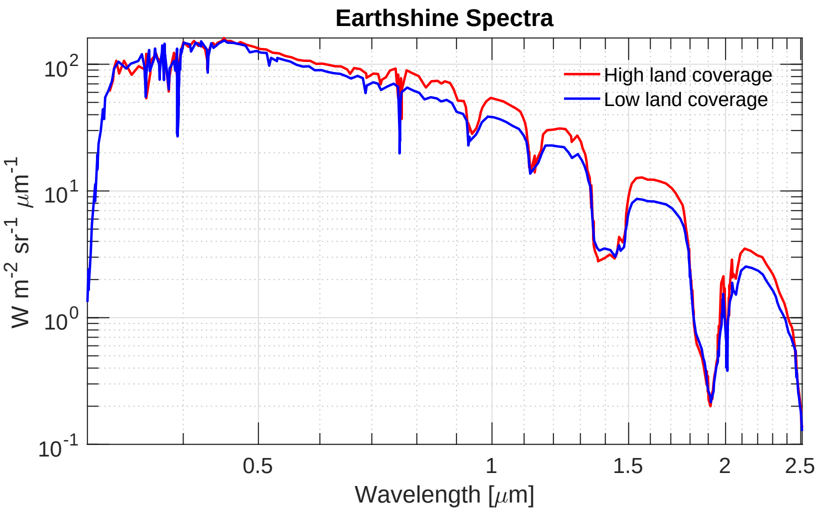

Figure 3.10: Earthshine solar reflectance spectra for a near-fully illuminated (> 99%) Earth disk. Two extremes in the fractional land coverage of the illuminated hemisphere are shown: the hemisphere of the Earth containing mostly ocean (blue) and a hemisphere containing more significant land coverage (red). In both cases, clouds contributed to the spectra. Data are taken from Glenar et al. (2019).

of the lunar poles is then extracted using the sublunar point and the hemispheric coordinates are projected onto a 2D plane (Figure 3.11). Using the horizon profiles, visible and IR Earthshine is mapped within PSRs pole-ward of 80° for one complete lunar precessional cycle (18.6 years), beginning at the northern vernal equinox on 28 July 2018 and stepping through time in 24-hr increments.

3.2.4 SWAN Ly-α All-Sky Maps

The Solar Wind Anisotropies (SWAN) instrument on the Solar Heliospheric Observatory (SOHO) spacecraft acquires intensity background maps covering the entire sky in the FUV region (115–180 nm) (Bertaux et al., 1995). Each SOHO/SWAN map is a grid spanning 360° longitude and 180° latitude (1° resolution) using an ecliptic

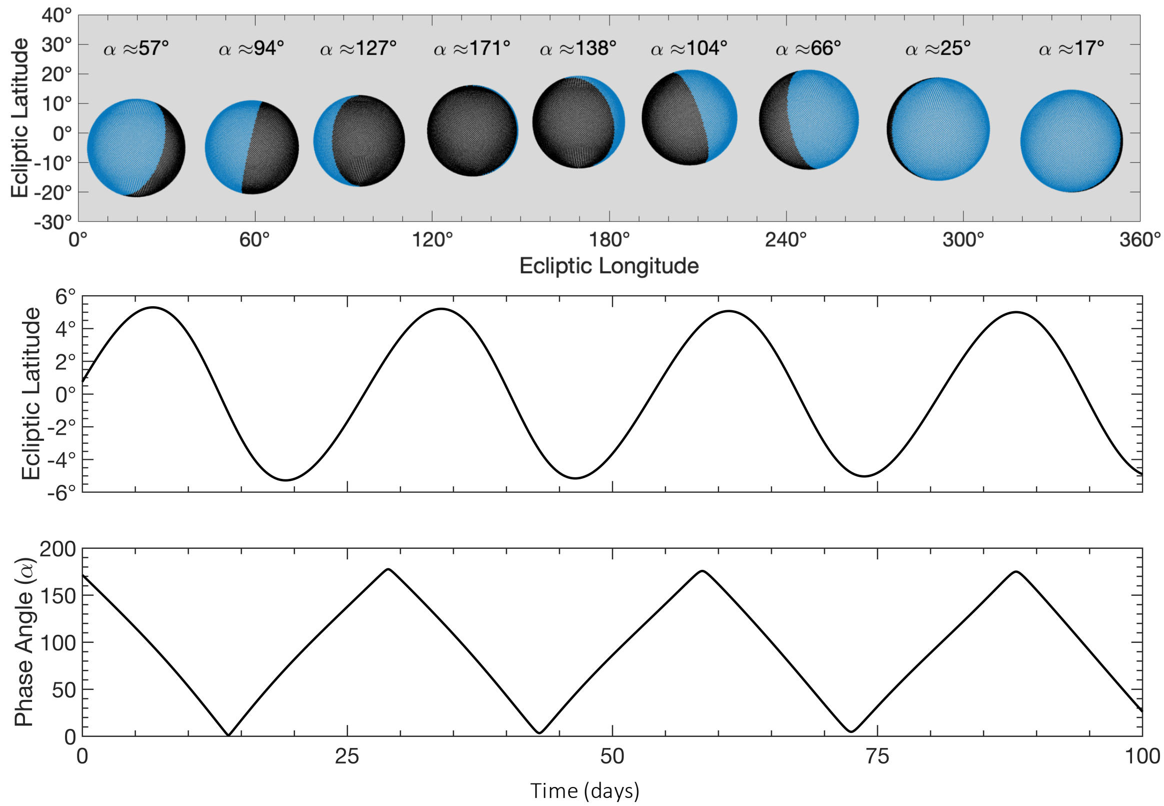

Figure 3.11: Top: Sequence showing the modeled illumination of a pixelated Earth, as seen from a lunar vantage point, over a 27.3 day period. Phase angles α (i.e. the Sun-Earth-Moon angle) are shown for each modeled disk. Blue regions of the disk are illuminated by the Sun while black points lie in darkness. Ecliptic latitude and longitude are with respect to a lunar-fixed reference frame. For clarity, the angular diameter of the Earth has been scaled by a factor of 17. Middle: Variation in the ecliptic latitude of the Earth from a lunar fixed reference frame over a 100-day period. Bottom: Phase angle variation over a 100-day period.

coordinate system. Two main causes contribute to the Ly-α intensity in each map: (1) the Ly-α interplanetary glow, which is caused by resonant scattering of solar Ly-α photons by interplanetary neutral H atoms and (2) nearby UV-bright stars in the Milky Way galaxy. While the stellar illumination is approximately constant, the interplanetary glow varies on seasonal timescales as the Earth's position changes in the interstellar wind and on shorter timescales due to variation in the solar Ly-α

flux. SWAN intensity maps are acquired near-daily, and thus are able to observe short-timescale variability of Ly-α flux.

The Ly-α intensity is highly non-uniform across the sky (Figure 3.12). As pointed out by Gladstone et al. (2012), the plane of the Milky Way galaxy dips below the ecliptic plane and contributes enhanced stellar brightness to the southern hemisphere. As such, the integrated brightness of the southern hemisphere is on average $\sim$14% brighter than that of the northern hemisphere. This difference is important given the low obliquity of the Moon's rotational axis to ecliptic plane, as the FUV photon flux at the north and south pole is approximately given by the integrated brightness of the northern and southern ecliptic hemispheres, respectively.

We analyze the Ly-α flux over one Earth year for the most recent year of SOHO/SWAN data at the time of writing (2018/2019). To avoid data contamination, we reject images with a median dark current level >20 counts as these images have excessive dark counts caused by solar events, rendering the data unreliable. Additionally, as can be seen in the top panel of Figure 3.12, regions exist where intensity data are missing (shown in white). These regions typically comprise about $\sim 9.5\%$ of the image, however the regions of missing data can be significantly larger, reaching in excess of 60% for some images. To minimize uncertainty, SWAN intensity maps containing more than 15% missing data are excluded from the analysis and regions of missing data are filled in with the annual average brightness. An example of this is shown in the lower panel of Figure 3.12.

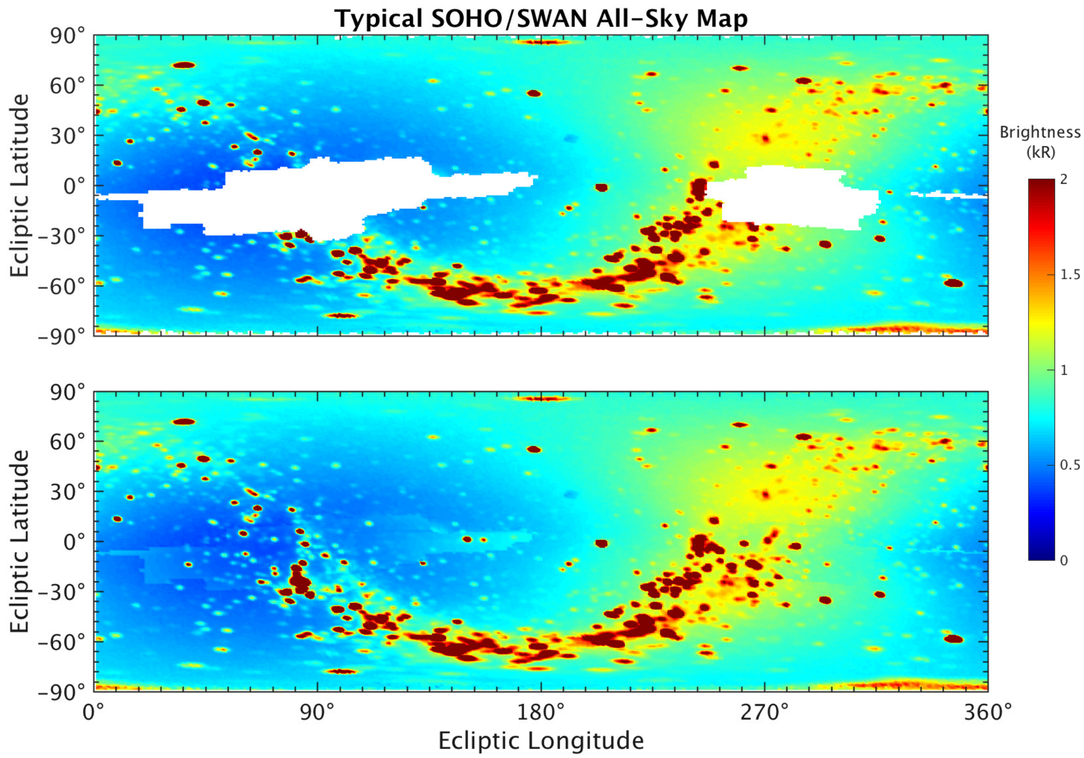

Figure 3.12: (top) Typical SOHO/SWAN all-sky Ly-α maps shown with missing data (white). Brightness in kR is represented as the color axis. (bottom) Same as above, but with missing data filled in using the average annual brightness.

To determine the Ly-α flux for a particular PSR element, the local horizon is oriented onto the celestial ecliptic sphere using the DE421 lunar ephemeris (Williams, Boggs, & Folkner, 2008); as each SOHO/SWAN map is acquired over a 24-hr span, the mid-point of the observation is used. The oriented horizon is then projected onto the SOHO/SWAN all-sky map and spatially integrated to obtain the incident FUV photon flux. Using the binary illumination maps produced by Mazarico et al. (2011), this process is repeated for all PSR surface elements pole-ward of $\pm 80°$ and for each SOHO/SWAN map within the study period. In total, 272 usable images were analyzed that span the 1-year study period.

3.2.5 Visible All-sky Map

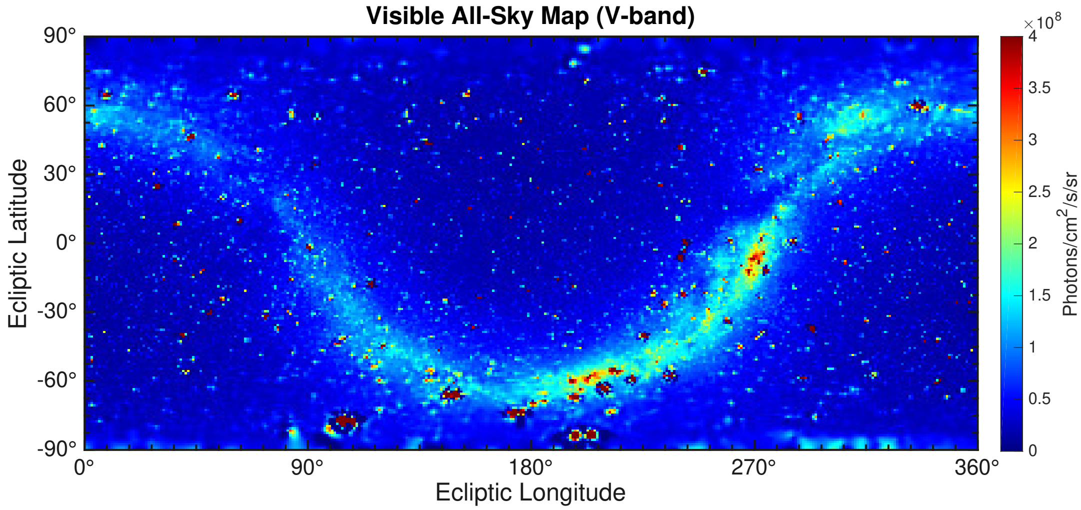

Figure 3.13: The Color All-Sky Panorama Image of the Milky Way from Mellinger (2009) plotted using an ecliptic coordinate system. The color axis corresponds to the photon flux density in the V-band spectral region (500-600 nm).

To model the visible photon flux within lunar PSRs due to starlight, we use the Color All-Sky Panorama Image of the Milky Way from Mellinger (2009). This image is a mosaic of over 3000 ground-based images acquired using a CCD camera and an RGB filter set. Individual images were astrometrically and photometrically calibrated; the latter was achieved via two steps. First, undesired signals from the background sky such as light pollution, airglow, zodiacal light and light from tropospheric scattering were removed. Secondly, to obtain absolute brightness measurements, stellar sources within each field were compared with flux measurements of reference stars given by the Yale Bright Star Catalog.

The units of brightness for each RGB band are given in $S_{10}(V)$, which corresponds to the number of tenth magnitude stars (in the V-band of the Johnson-Cousins filter set) of solar spectral type per square degree. It should be noted that a spectral correction parameter is applied to each image band in order to scale the RBG intensity to that of the V-band. As the bandpass of the G-band is closely aligned with that of the V-band, the spectral correction parameter for this channel is near-zero. For this reason, we use the G-band image for our analysis and convert the units of the image from $S_{10}(V)$ to radiance (W m^{-2} sr^{-1}). The original image was converted from galactic to ecliptic coordinates, and downsampled to a 1° pixel^{-1} resolution, thereby matching the SOHO/SWAN all-sky maps. The V-band of Color All-Sky Panorama Image of the Milky Way from Mellinger (2009) is shown in Figure 3.13.

3.3 Results

3.3.1 Illumination from the IPM and Starlight

The resulting FUV flux reaching the lunar PSRs originating from the IPM and UV-bright stars is mapped in Figure 3.14. Here, we show the average flux density in the spectral range 115–180 nm for PSR locations pole-ward of ±80° across the one year study period. In the northern hemisphere, we find an average FUV flux of 2.87± 0.08 (1σ) μW m^{-2} while in the southern hemisphere, the average is 3.39 ± 0.08 (1σ) μW m^{-2}. The illumination is spatially variegated within individual craters due to subtle topographic deviations, although individual regions are reasonably homogeneous (σ = 0.02 μW m^{-2}). As noted previously, the FUV radiation varies over seasonal timescales due to Earth's changing position in the interstellar wind as it orbits the Sun (Figure 3.14c).

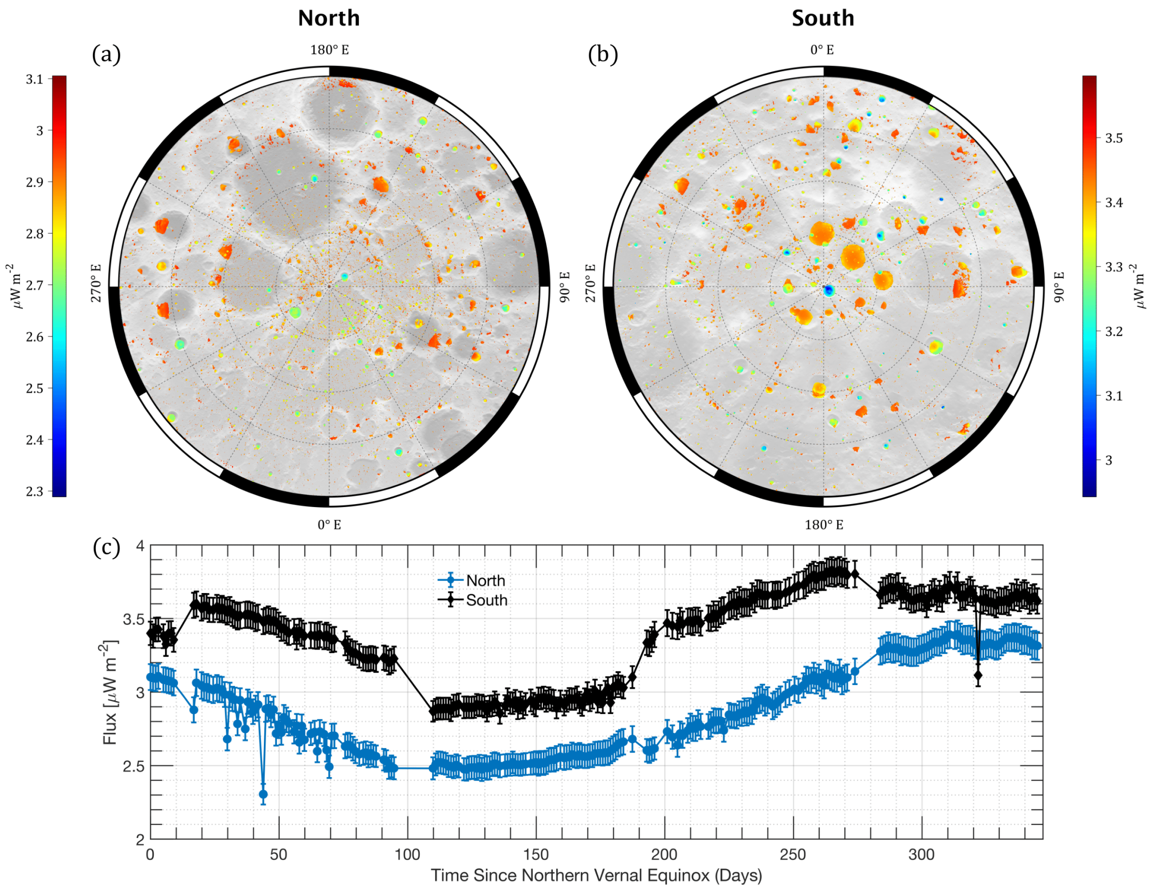

Figure 3.14: Average far ultraviolet (115–180 nm) flux from IPM and starlight reaching PSRs at the north (a) and south (b) pole of the Moon. Note that the scale of the colorbar differs for the north and south pole. (c) Temporal variability of FUV flux across one lunar year. Data represent the mean of all PSR elements and are shown with 1σ error bars. Seasonal variation is due to the changing position of the Earth with respect to the interstellar wind. Gaps in data represent SOHO/SWAN all-sky maps with excessive dark current and/or > 15% missing data.

Maps of the visible (500–600 nm) PSR flux from starlight are shown in Figure 3.15. Of course, the regional and broad-scale spatial trends in illumination are similar to the FUV maps shown in Figure 3.14. The average flux is 0.55 $\pm$ 0.016 (1σ) μW m^{-2} and 0.71 $\pm$ 0.023 (1σ) μW m^{-2} for the northern and southern hemisphere, respectively.

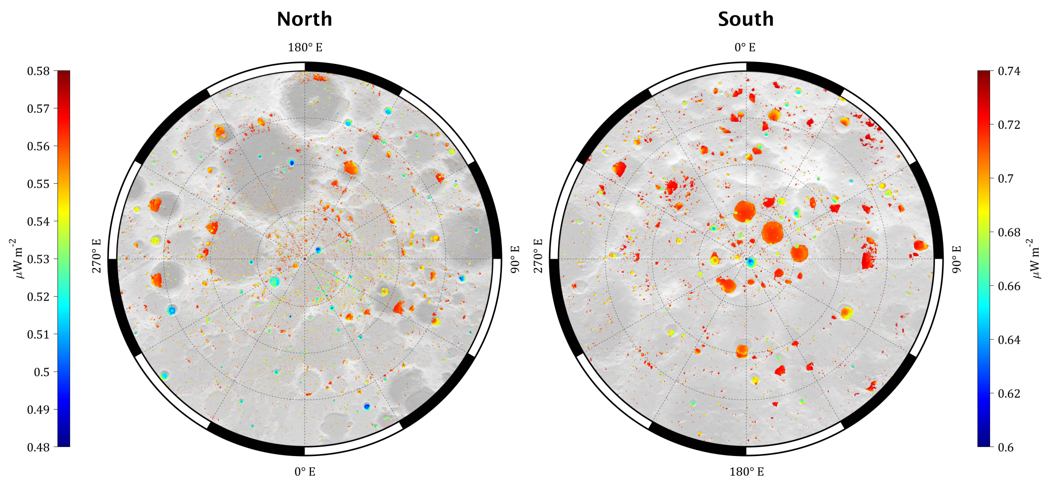

Figure 3.15: Average visible (500–600 nm) flux from starlight received by PSRs at the north and south pole of the moon.

3.3.2 Illumination from Earthshine

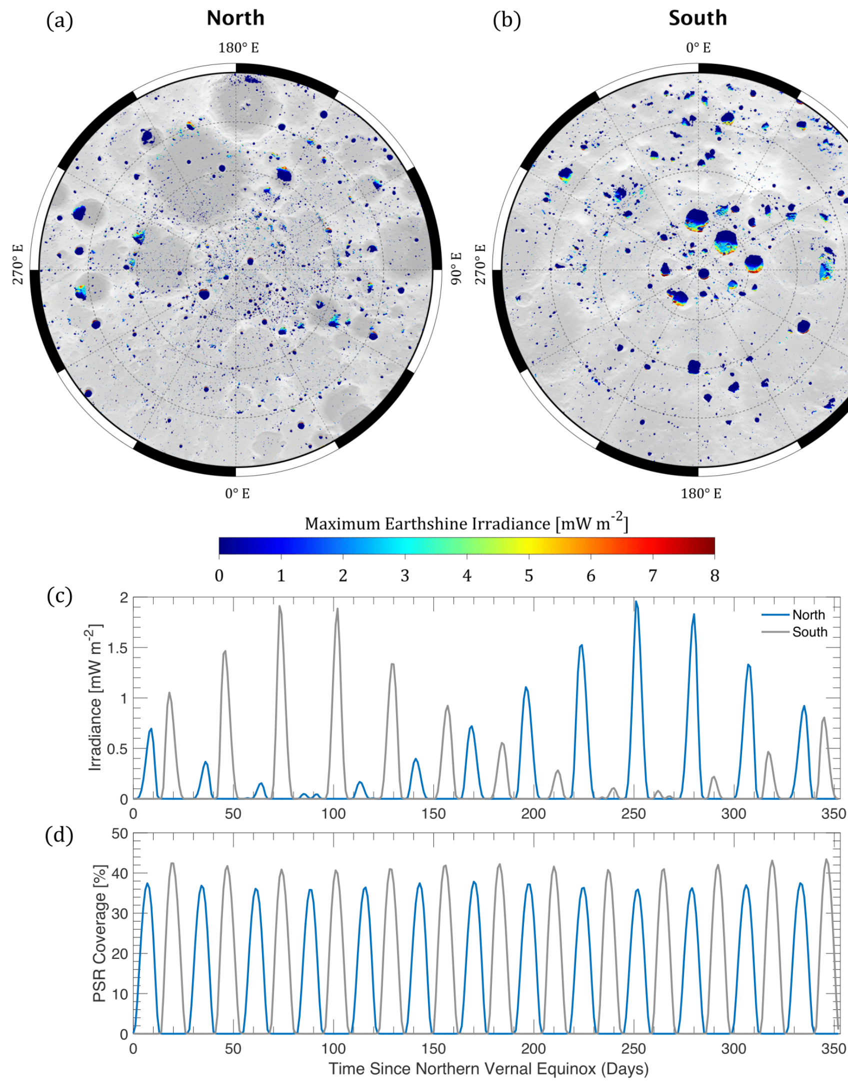

Figure 3.16: Maximum Earthshine irradiance within lunar PSRs at the north (a) and south (b) poles across one lunar precessional cycle (18.6 years). Data are shown for the visible band (500-600 nm). Maps from Mazarico et al. (2011) were used to identify PSR locations. (c) Temporal variation in Earthshine for a typical year; each data point within the line represents an average of all PSRs pole-ward of ±80°, with surface elements permanently shielded from Earthshine omitted from the average. (d) Variation in the PSR coverage of Earthshine for the same time period. Note that data exhibit slight interannual variation.

Shown in Figure 3.16a and b are maps that display the *maximum* Earthshine irradiance across the 18.6 year study period for the visible band; similar maps for the two IR bands are provided in Appendix Figures B.1 and B.2. As is evident from these maps, many permanently shadowed surfaces are also perpetually shielded from Earthshine: at maximal coverage, only 40.2% of northern hemisphere PSRs are exposed to this source, while coverage increases to 45.2% for southern hemisphere PSRs (Figure 3.16d). The three largest contiguous regions of permanent shadow on the Moon – the floors of Haworth, Shoemaker and Faustini – receive 52.8%, 60.2% and 55.7% coverage at their maximum extents, respectively. Other craters of interest receive significantly less flux, such as Shackleton crater at the south pole which has a maximum coverage of only $\sim$ 16.7% owing to its high depth-to-diameter ratio. Earthshine may have more significant coverage within lower-latitude PSRs on the nearside of the Moon, however, for reasons examined below in section 3.3.3, these areas tend to have higher maximum temperatures (Paige et al., 2010; Williams et al., 2019), and thus are less likely to be cold traps for volatiles.

As shown in Figure 3.16c, Earthshine illumination oscillates over diurnal and seasonal timescales. Diurnal variation occurs due to the $\sim 6^{\circ}$ undulation of the subearth latitude about the lunar equator, which varies with a period of one sidereal day ($\sim$13 cycles per Earth year) due to the inclination of the Moon's orbit. Seasonal variation occurs due to a confluence of the subearth latitude variation and the Sun-Earth-Moon angle (i.e. phase angle), with seasonal maxima occurring at times when the phase angle is low and the elevation of the Earth reaches a diurnal peak. Figure 3.16c presents the temporal variation in Earthshine across one year, where PSRs that do not receive Earthshine were omitted from the average. The fractional cloud coverage on Earth's illuminated disk may provide additional variation on shorter timescales.

3.3.3 Illumination from Scattered Sunlight

Geographic Variability

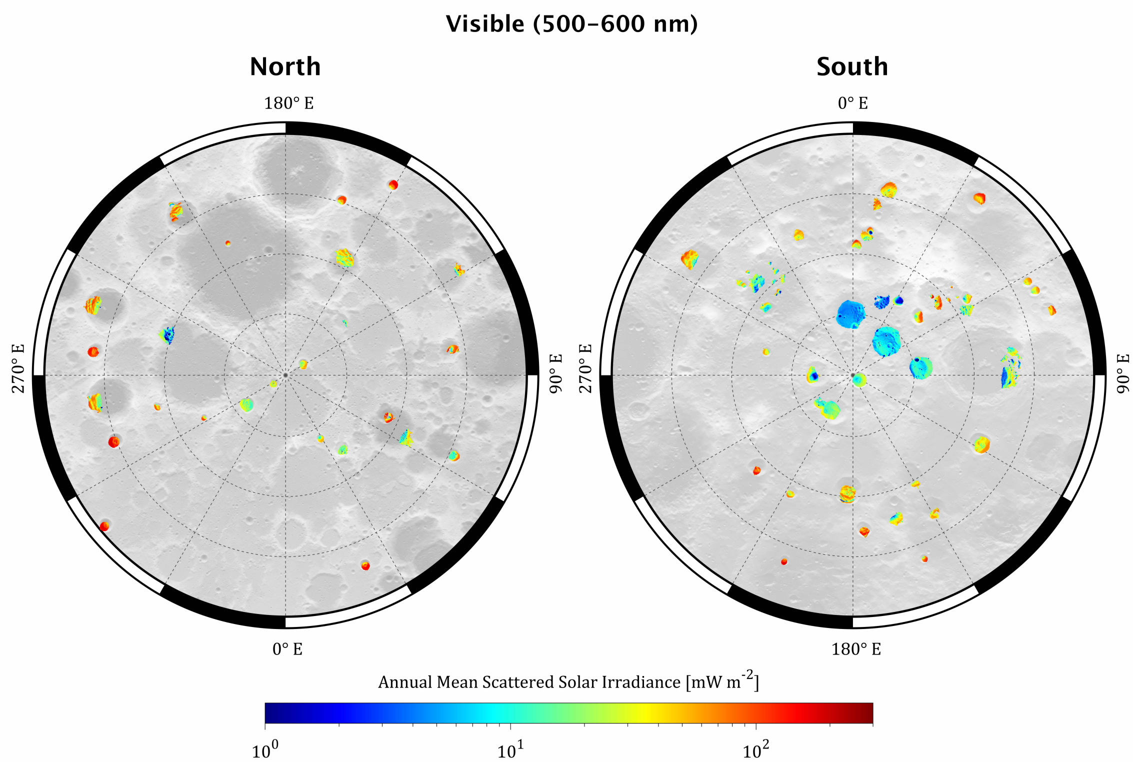

Figure 3.17: Annual mean Visible (500–600 nm) scattered solar irradiance (mW m^{-2}) received by areas of permanent shadow at the north and south pole of the Moon. Note that similar maps created for the FUV and IR bands have been included as Appendix Figures C.1, C.2 and C.3.

Figure 3.17 displays the annual average scattered solar illumination received by individual PSRs for the visible band; similar maps created for the FUV and IR bands have been included as Appendix Figures C.1, C.2 and C.3, respectively. As these maps demonstrate, the vast majority of permanently shadowed regions receive some amount of scattered flux, as only a small percentage (0.03%) of PSR elements were found to be doubly shaded from sunlight. Still, there is significant geographic differences in the quantity of energy delivered to these areas. In Haworth crater at the south pole, for example, the annual mean PSR irradiance in the visible band is 5.3 ± 1.6 (1σ) mW m^{-2} while the permanently shadowed interior of Lovelace E (82.0° N, 263.2° E) crater at the lunar north pole receives an average irradiance of 103 ± 26.2 mW m^{-2}, or more than twenty times that of Haworth. Among the factors that modulate the scattered flux received by a PSR is its proximity to the rotational pole. Figure 3.18 shows the annual maximum irradiance PSRs receive as a function of latitude, where data are separated by spectral band. As seen here, near-polar PSRs tend to receive less solar energy given the reduced solar incidence angles at high latitudes as well as less illuminated terrain from which scattered energy can be received. Poleward of ±80°, the change in irradiance as a function of latitude can be approximated as linear, with line-of-best-fit slopes m = -2.3e-3, -30.5, -9.8 and -4.2 mW m^{-2} for the FUV, visible and two IR bands, respectively. The enhanced scattered solar energy supplied to low-latitude PSRs yields warmer surface temperatures (Paige et al., 2010; Siegler et al., 2015), and in turn less favorable conditions for surface ice due to higher rates of sublimation and desorption. Molecules desorbed from low-latitude PSRs may continue to migrate poleward and accumulate in the higher latitude cold traps where temperatures are diminished, thereby amplifying the preferential delivery and accretion of water at high polar latitudes described by Kloos et al. (2019). Water buried beneath the surface, however, may have enhanced survivability as it is protected from loss processes and may remain stable across geologic periods even in low-latitude regions (Feldman et al., 2000; Mitrofanov et al., 2010).

Other factors, such as the depth-to-diameter (d/D) ratio of the crater, also influence the quantity of sunlight received, and may contribute to the scatter in the data from Figure 3.18. To understand the relationship between crater geometry and scattered flux, d/D ratios for the craters of interest were obtained using diameters from the USGS and the empirically-derived depth-diameter relationship for lunar craters provided by Pike (1977). In Figure 3.19, the annual maximum irradiance is plotted as function of d/D, where, to separate out the effects of latitude and crater geometry on the received flux, we restrict the data to only lower latitude craters (equatorward of $\pm 85°$). From the resulting figure, it is evident that PSRs within smaller craters (larger d/D) tend to receive more energy than those within larger craters (smaller d/D) owing to the fact that smaller craters have steep walls that reflect more direct, high energy sunlight into the PSR. Disparities in the received flux occur between craters of similar d/D, however, as the quantity of flux incident on a given PSR is also influenced by the regional topography, which determines the amount of sunlit area surrounding the PSR from which scattered light is received.

In addition to variation between craters, local heterogeneities in the received flux

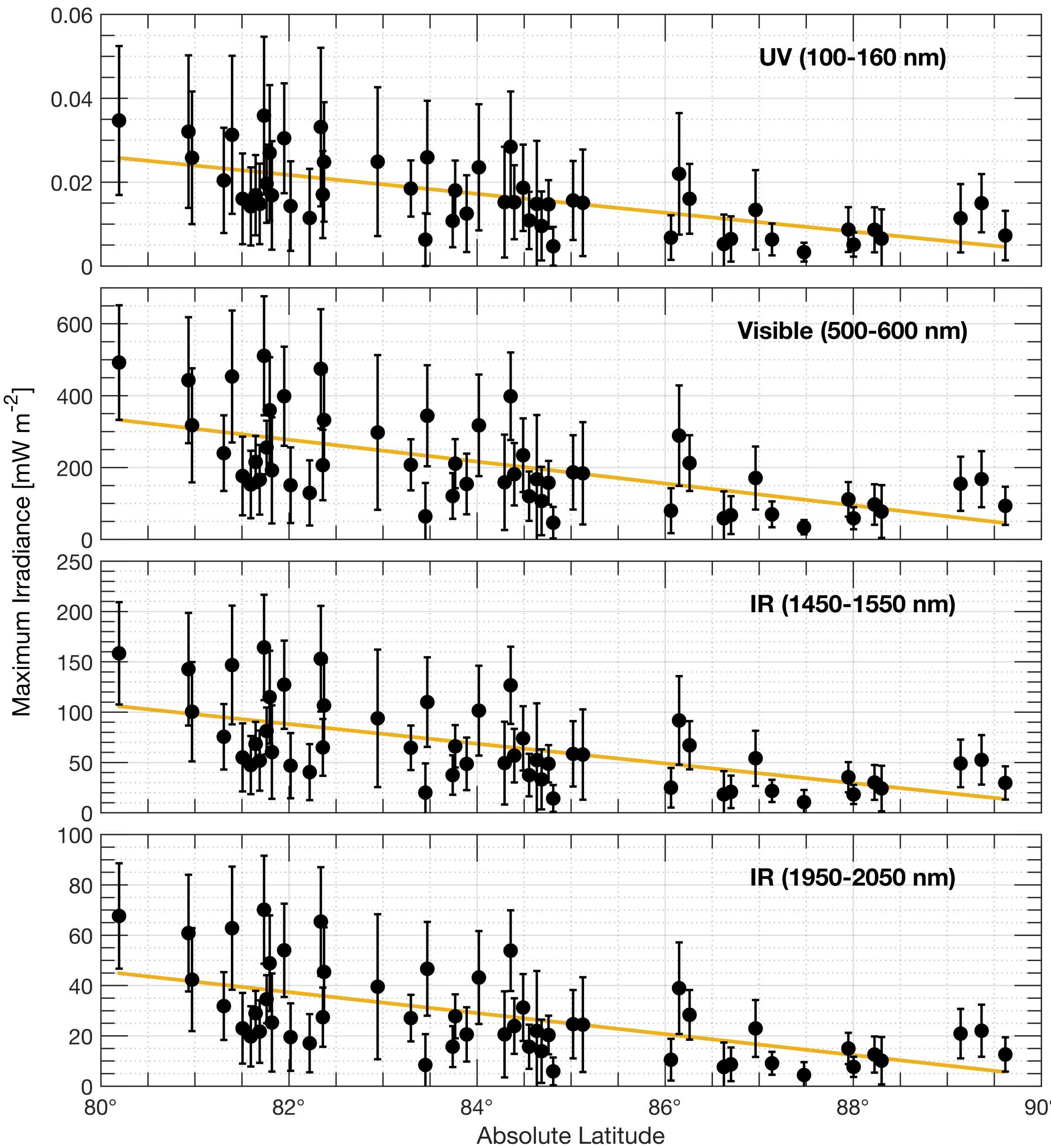

Figure 3.18: Annual maximum scattered solar irradiance received by PSRs as a function of absolute latitude. Each data point represents the mean irradiance of the PSR within a given crater at its summer diurnal peak; data are shown with 1σ variation.

are prominent within individual PSRs (see Figure 3.17). In contrast to starlight, which emanates from all directions of the sky and provides a relatively even dispersal

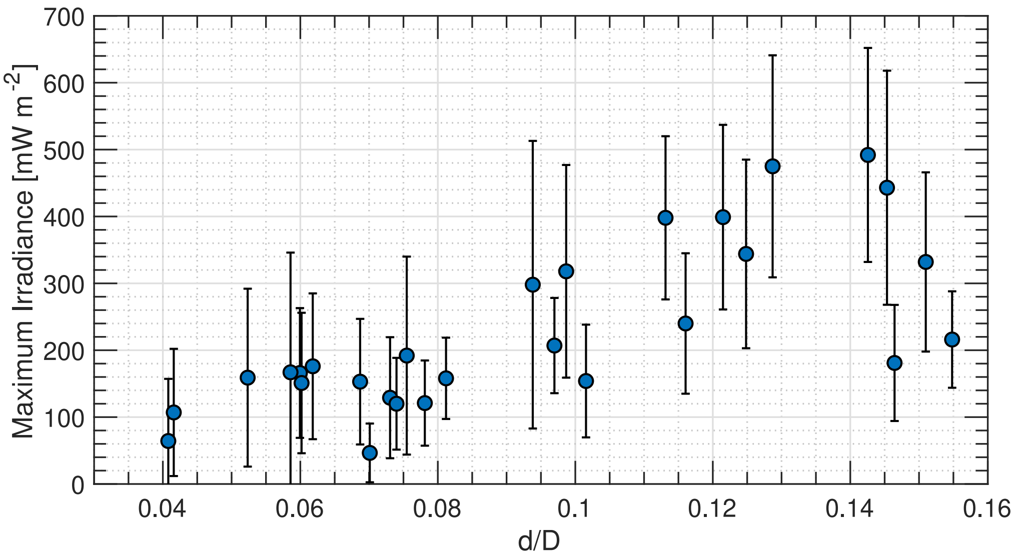

Figure 3.19: Maximum irradiance received by PSRs as a function of the crater's depth-to-diameter (d/D) ratio. Here, data are restricted to high-latitude craters (poleward of ±85°) in order to uncouple the effects of latitude and crater shape on the received scattered solar flux. Each data point represents the mean irradiance of the PSR within a given crater at its summer diurnal peak; data are shown with 1σ error bars.

of light across the surface, sunlight scattered into a PSR tends to emerge from a narrow section of the nearby sunlit terrain, meaning that topographic variance and scattering geometry have a large influence on the dispersion of scattered energy. An illustrative example of this is found when the maximum irradiance is plotted as a function of slope azimuthal angle, β, as is shown in Figure 3.20, where data for each spectral band contain an average of the northern and southern hemisphere PSR elements, are binned in 3° increments and normalized at an azimuthal angle of 0°, or a pole-facing slope. As seen here, PSR slopes at high azimuthal angles (β near 180°, or equator-facing) receive ~60% less energy than pole-facing slopes in the visible and IR bands. This inequality is a result of the location and azimuthal orientation of pole-

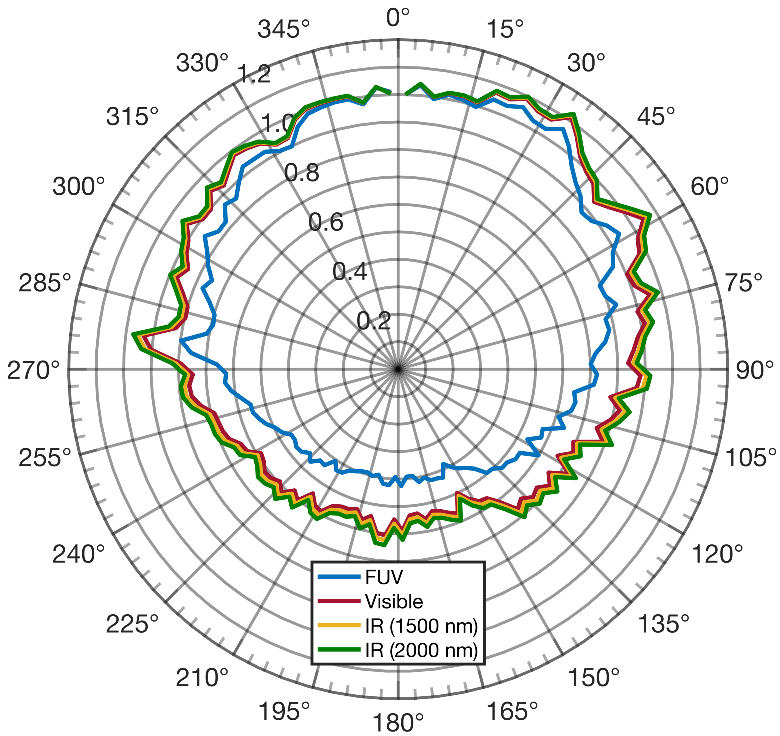

Figure 3.20: Maximum irradiance by PSRs as a function of slope azimuthal angle, β. Slope azimuth angle is defined as the slope aspect's angular deviation in degrees from the pole-facing direction. Data are normalized at $\beta = 0°$, which is designated as a pole-facing slope.

facing, PSR slopes relative to the equator-oriented, sunlit slopes that are scattering light into the PSR. In other words, PSR slopes that are oriented toward the sunlit terrain receive more direct scattered solar illumination (at lower incidence and phase angles) relative to other other slope orientations. In the FUV this effect is enhanced due to the highly backscattering nature of lunar regolith particles at UV wavelengths (Liu et al., 2018), and thus equator-facing PSR terrain elements receive only 40% as much energy as their pole-facing counterparts. We note, however, that this figure represents an upper limit for the FUV as laboratory measurements of Apollo samples report a reduced backscattering behavior in this regime (Raut et al., 2018). Still, large spatial gradients in energy delivery are produced through this effect, leading to geographic heterogeneities in surface temperature and photodesorption rates. Given that temperature is the primary factor controlling volatile residency times, volatile stability may be enhanced on high azimuthal angle PSR slopes where temperatures are decreased.

The solar irradiance quantities reported here are expected to be lower limits given that crater walls tend to have more reflective surfaces due to the effect of mass wasting exposing bright, fresh material which has been less exposed to space weathering (Pike, 1970). Kennelly et al. (2010) found improved model fits by defining a separate scattering regime consisting of craters when constraining the Hapke parameters; for the crater regime, the derived single scattering albedo was increased by 10–40% relative to highlands surfaces at visible and IR wavelengths. In addition, given the low albedo of the Moon we consider only singly-scattered light reflected into the PSRs, yet multiple scattering will enhance the downwelling photon flux into these areas. By our estimates, the contribution from multiple scattering is small, amounting to $\sim 1\%$ of the total flux attributable to single-scattering from directly illuminated surfaces.

Temporal Variability

The scattered solar flux supplied to PSRs varies over diurnal timescales as well as seasonal timescales due to the slight obliquity of the Moon. To express the temporal variation for a particular crater, we show the average irradiance received by the PSR floor as a function of time. Time series for Faustini, Haworth and Braude are shown in Figure 3.21 for the FUV band (left-hand column) and for the visible and IR bands (right-hand column). To provide a measure of uncertainty in the FUV scattered flux, these selected craters were also modeled using the laboratory-derived phase function terms ($b = 0.158$ and $c = 1.08$ using formula 3.4) of Raut et al. (2018), which vary significantly from the spacecraft-derived quantities reported by Liu et al. (2018) at low phase angles (see Figure 3.8). For comparison, the mean IPM/starlight flux of the PSR is also plotted in the FUV panels of Figure 3.21.

Some PSRs, such as those in Faustini crater (87.2° S, 84.3° E) and Braude crater (81.8° S, 158.9° E) in the southern hemisphere, receive flux in a relatively predictable way, with 11–12 diurnal peaks spread across the draconic year spaced at intervals of $\sim$1 synodic day. Other craters, however, such as Haworth, have a more complex time series (Figure 3.21 middle): During the winter, Haworth receives little to no sunlight when the region is blanketed by seasonal shadow (Kloos et al., 2019); during the summer, however, the incoming flux exhibits erratic shifts as the regional topography casts long shadows over the crater, which provides irregular coverage of sunlight on the scattering terrain. Despite being of comparable size and lying at a similar latitude, the average energy Haworth receives is reduced in magnitude by a factor of $\sim$2 relative to Faustini, consistent with it being one of the coldest PSRs in the region (Williams et al., 2019).

With respect to the FUV illumination, Figure 3.21 shows that the relative strength

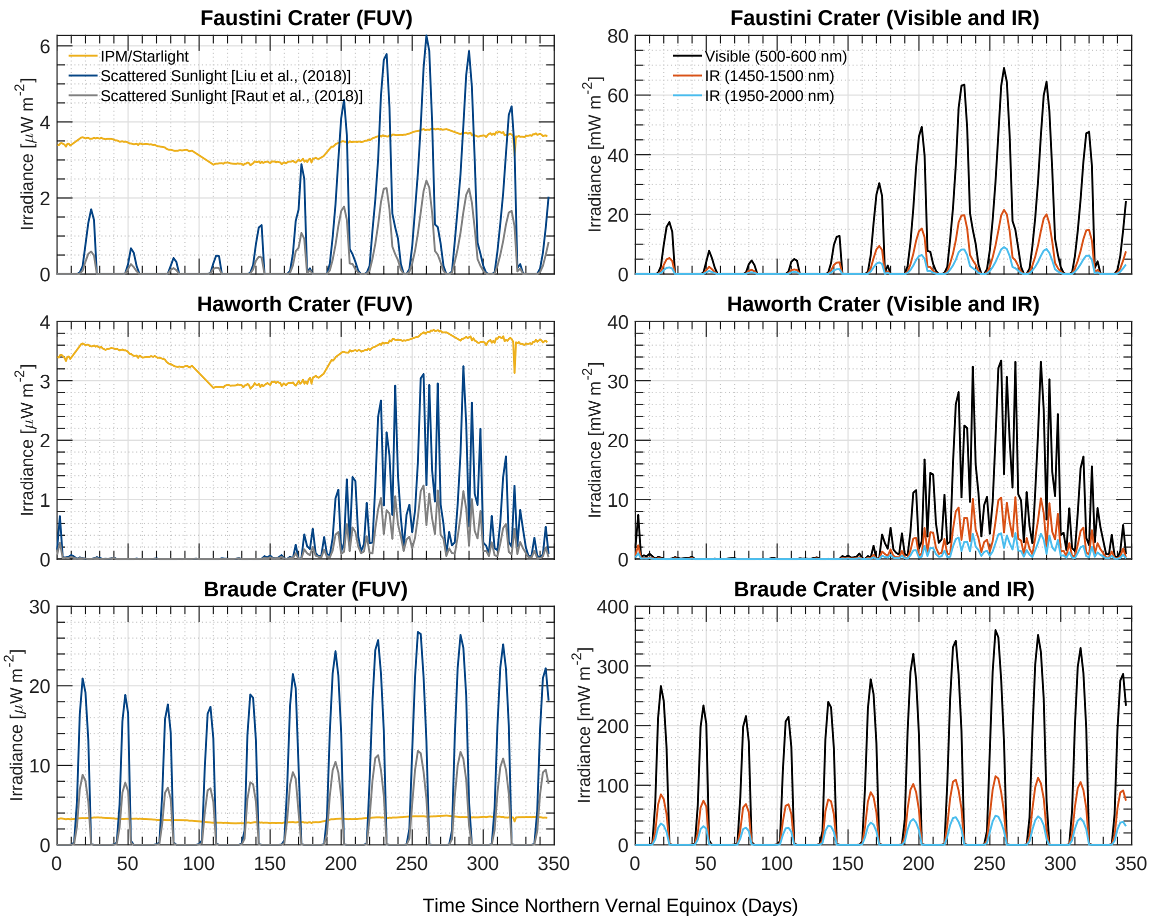

Figure 3.21: Temporal variability of scattered solar illumination received by the Faustini, Haworth and Braude PSRs at the lunar south pole. The left-hand panel of each row compares the FUV illumination sources (with units of μW m^{-2}) within a given crater, including IPM/starlight and scattered sunlight modeled with the phase function parameters of Liu et al. (2018) and Raut et al. (2018); the right-hand column shows the modeled visible and IR radiation (with units of mW m^{-2}).

of scattered sunlight and IPM/starlight varies depending on the crater, time of year and the backscattering behavior of the lunar surface, as the subdued backscattering response reported by Raut et al. (2018) reduces the received irradiance by more than a factor of 2 owing to the abundance of low phase angle geometries encountered for scattered sunlight (see Figure 3.7). For some PSRs such as Faustini, depending on the phase function applied the diurnal summer peak of FUV scattered sunlight may exceed the IPM/starlight flux, which hovers between 3.5–4 μW m^{-2} throughout the year. This does not mean that FUV scattered sunlight is in excess for all regions of the crater interior *per se*, as smaller impact craters on the crater floor may be shaded or partially shaded from singly-scattered sunlight; for these doubly shaded areas, light from the IPM/starlight will remain the dominant FUV source year-round. This also applies to certain craters with reduced scattered fluxes such as Haworth, independent of the phase function employed. The geographic trends described in section 3.3.3, however, suggest that the strength of the scattered sunlight relative to IPM/starlight is enhanced for lower-latitude PSRs and high d/D ratio craters. This is verified in the case of Braude crater, where scattered sunlight, when illuminating the PSR, exceeds the IPM/starlight flux year-round. This trend will be enhanced during periods of solar maximum when quantities of FUV sunlight are increased by ~20%, as well as for north polar PSRs which have reduced IPM/stellar fluxes due to the paucity of stars in the northern ecliptic hemisphere. In other words, our modeling indicates that scattered sunlight represents a considerable source of FUV photons to the permanently shadowed regions.

The flux of these highly energetic solar FUV photons to the PSRs, which has previously not been considered, has new implications for the photodesorption rate of water and thus for the lifetime of individual water molecules. Given the geographic and temporal trends of scattered sunlight reported in this work, the rate of photodesorption will exhibit significant diurnal, seasonal and geographic variations according to the incident FUV solar irradiation. This is also true given that the desorption yield (H_2O/photon) is positively correlated with the ice temperature (Öberg et al., 2009; Westley et al., 1995), indicating that low-latitude PSRs, where both surface temperature and FUV irradiation are increased, will experience exponentially higher rates of desorption relative to near-polar PSRs. The photodesorption rate of 4.4×10^5 cm^{-2} s^{-1} stated by Gladstone et al. (2012) is therefore a lower limit as it is made on the basis of IPM/starlight alone, and will only be valid in PSRs where IPM/starlight is the prevailing photon source year-round (such as Haworth). The comparative significance of FUV solar flux may also have implications for the LAMP data set, which is currently modeled using only IPM/starlight (Gladstone et al., 2012). Exactly how the inclusion of scattered sunlight may impact the LAMP results, however, is difficult to ascertain without further assessment of the spectral differences in the received scattered solar irradiance between the LAMP off-band (155–190 nm) and on-band (130–155 nm).

In the visible and IR regimes, even for PSRs that receive, on average, less scattered solar radiation such as Haworth, this source of illumination is still considerably larger than that of other sources. At the summer diurnal peak when scattered flux is maximized, visible indirect sunlight is 5-6 orders of magnitude greater than starlight. With respect to Earthshine, according to diurnally averaged Earthshine spectra from Glenar et al. (2019), the maximum flux in the 500–600 nm spectral range scattered from a fully illuminated Earth disk and received at the Moon is 11 mW m^{-2}. As the subearth latitude varies $\sim 7°$ about the lunar equator, Earthshine illuminates the lunar polar regions at relatively large incidence angles ($i > 50°$), which reduces the maximum possible visible Earthshine irradiance received by a PSR to ~7 mW m^{-2}. This is $\sim 5\times$ less than the maximum scattered solar flux received by Haworth's PSR, $\sim 10\times$ less than that received by Faustini and more than $\sim 50\times$ less than Braude (see Figure 3.21, right-hand panels). Similar calculations in the IR show even larger differences between scattered sunlight and Earthshine, with the former exceeding the latter by a factor of ~100 and ~250 for the 1500 nm and 2000 nm bands, respectively in Braude crater (Glenar et al., 2019). While scattered sunlight represents a more significant source of natural illumination to the lunar PSRs, it is notable that both scattered solar radiation and Earthshine are diurnally variable and may illuminate areas of permanent shadow asynchronously. It is also worth highlighting here that Earthshine only illuminates 40% and 45% of the permanently shadowed area poleward of ±80° in the north and south, respectively (Kloos & Moores, 2019), and thus has limited utility for water ice prospecting.

The seasonal change in energy delivered to the PSRs through scattered sunlight may vary significantly depending on the region. For the majority of craters in this study, particularly those that are located at lower latitudes (equatorward of ±85°), the ratio of the diurnal summer peak to the diurnal winter peak – referred to here as the seasonal amplitude – is small, with values between 1.5 and 2 (Figure 3.22). The

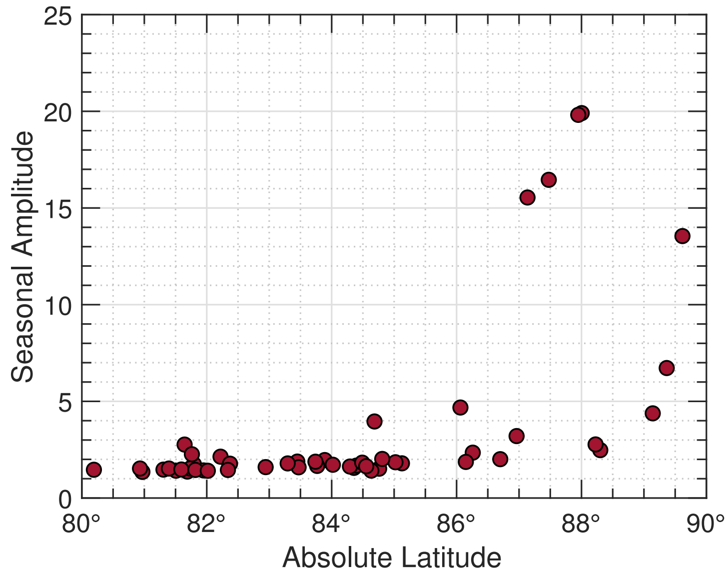

Figure 3.22: Seasonal amplitude – defined as the ratio of the summer diurnal peak to the diurnal winter peak – plotted as a function of latitude.

seasonal amplitude for near-polar craters, however, can be much larger owing to the moderating influence of seasonally shadowed regions, which are concentrated at high latitudes (Kloos et al., 2019). As seen in Figure 3.22, the amplitude of seasonal flux can be as high as ∼20 for craters located poleward of ±86°. The cycling of thermal energy to the PSRs – whether diurnally or seasonally – may have consequences for the diffusion of volatiles into the subsurface (Schorghofer & Aharonson, 2014), although modelling this effect is outside the purview of this work. The effect of seasonality as it relates to remote sensing, however, will be discussed in section 3.4.

3.4 Detection of Water Ice Within PSRs Using Passive Multispectral Imaging

3.4.1 Radiance modelling for Ice-Regolith Mixtures

As the brightest source of illumination to reach the PSRs, scattered sunlight should permit the use of passive remote imaging as a means of water ice detection. A camera equipped with vis/FUV or vis/IR filter pairing may be able to uniquely map the surface coverage of water frost from a distance and identify regions of interest for further study. Certain questions, however, remain regarding this technique. Namely, which filter pairing is optimal for the identification of water ice given the comparative scattering properties of lunar regolith and water ice and the available illumination in each of the spectral bands? What are the limitations associated with this approach? Furthermore, what are the optics and integration times needed to clearly differentiate ice from regolith?

To explore these questions, we simulated the research conditions expected for in-situ exploration of the PSRs: We imagined a camera, mounted on a rover positioned at the crater's edge, looking down into the crater interior and imaging the permanently shadowed surface. Synthetic images were generated by modelling the radiance received at the camera for signals consisting of dry regolith and pure water ice; for signals consisting of a mixture of both endmembers, an areal mixing model was used.

An areal mixing model is suitable for conditions where ice is present in the form of patches on the surface, and individual photons only interact with a single species. Given the high spatial resolution achievable through surface imaging, it will be possible to spatially resolve individual patches of ice on the surface should they be present, indicating that the signal received by the camera may come entirely from light scattered from pure water ice (or dry regolith). For the visible and IR bands, we assume only scattered sunlight as the illumination source; this assumption is justified given that sunlight is several orders of magnitude larger than starlight and more than an order of magnitude greater than Earthshine in most craters (see section 3.3.3). For the FUV band, however, we combine the illumination from IPM/starlight Ly-α and scattered sunlight.

The radiance emitted by the PSR regolith in the direction of the camera is obtained by applying the Hapke model to a second reflection of light from the crater floor to the camera using the method described in section 3.2.2, while the radiance contributed by water is modeled with an assumption of Lambertian scattering. The radiance emitted from a patch of water on the surface I_{λ,H_2O} is described by the equation:

$$I_{\lambda,H_2O}(i) = \frac{k_\lambda F_\lambda \mu_{0e}}{\pi}, \tag{3.8}$$

where k_λ is the fraction of light scattered, and F_λ is the in-band flux originating from the light scattering terrain and incident on the patch of water. Under the assumption of Lambertian scattering, k_λ is given by the directional hemispheric albedo, which is

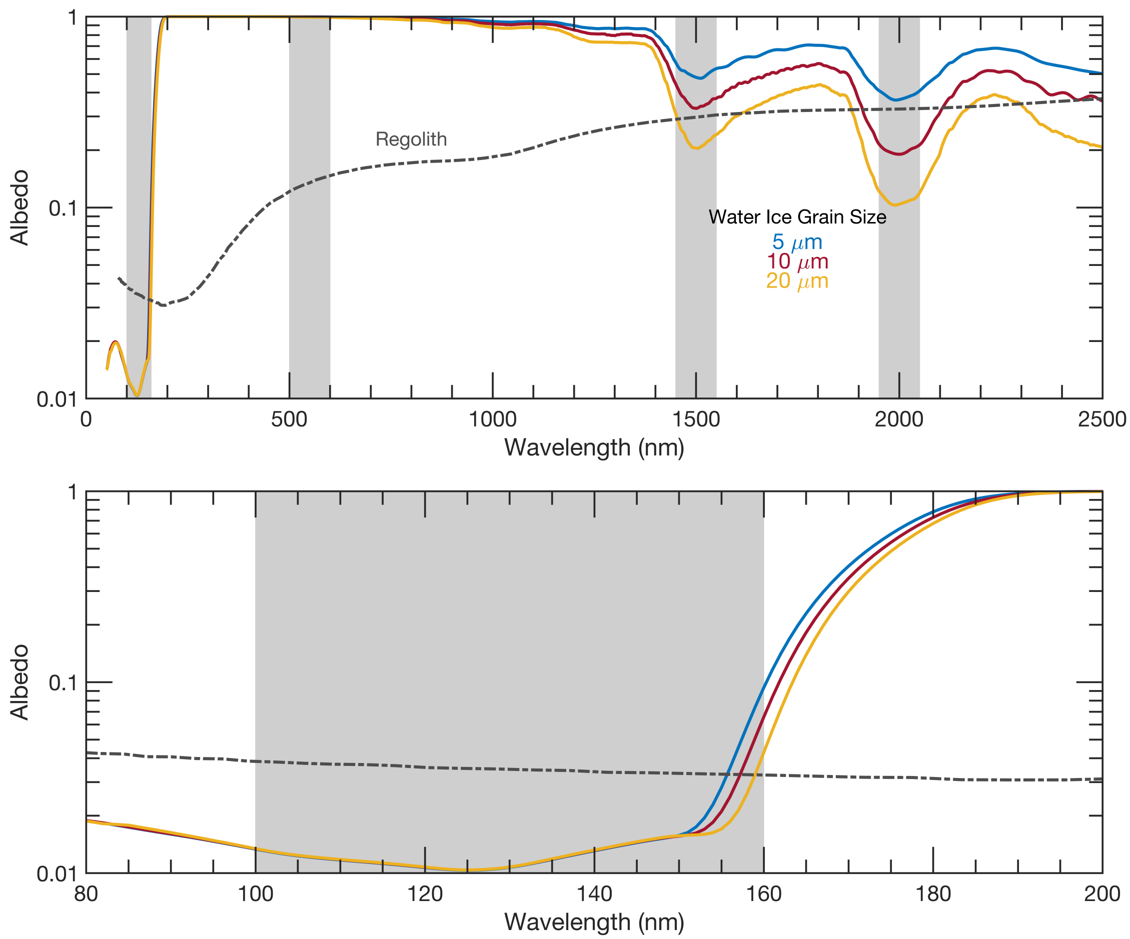

Figure 3.23: (Top) Spectra for water ice of varying grain sizes modeled using radiative transfer theory of Wiscombe and Warren (1980) and optical constants derived from Warren and Brandt (2008). The spectra shown represent directional hemispheric albedo, defined as the ratio of the power of the incident beam to the power reflected into an entire hemisphere. Gray shaded regions denote the image bands studied in this work, which include three regions of water ice absorption near 165 nm, 1500 nm and 2000 nm along with a region non-absorption at 550 nm. Juxtaposed with water is a composite albedo spectra for an "average moon" using observational data as well as laboratory measurements of lunar samples from Shkuratov et al. (1999). (Bottom) Same as above but highlighting the FUV spectral region and the grain size dependency in the water ice absorption edge near ∼165 nm.

defined as the ratio of the power within the collimated incident beam to the power reflected into an upper hemisphere. To model the directional hemispheric albedo, we use radiative transfer theory of Wiscombe and Warren (1980), optical constants from Warren and Brandt (2008) and a Mie scattering code based on the appendix material of Bohren and Huffman (2008), prepared by Christian Maetzler for Matlab. The output of this model is shown in Figure 3.23 for grain sizes of 5 μm, 10 μm and 20 μm in radius. The large water ice absorption (nearly two orders of magnitude) is evident in the FUV, whose absorption edge near ∼165 nm is shown to vary with grain size as is highlighted in the lower panel of Figure 3.23 (see also Hendrix and Hansen (2008)). In the IR at 1500 nm and 2000 nm, the depth of the absorption is grain size dependent, with larger grains possessing a deeper absorption. Also shown in Figure 3.23 is the albedo of lunar regolith which is taken using data from Shkuratov et al. (1999) which exhibits a sharp increase in reflectance between 300–500 nm, and a steady, more gradual increase with wavelength beyond 500 nm.

For a given fractional coverage of water ice ρ, the radiance received at the camera $I_{\lambda,Mix}$ using an areal mixing model is given by

$$I_{\lambda,Mix}(i,e,\alpha) = I_{\lambda,H_2O}\rho + I_{\lambda,reg}(1-\rho). \tag{3.9}$$

Due to the strong directional dependence of light scattering for lunar regolith particles, the illumination and viewing conditions of an observation will have significant influence on $I_{\lambda,Mix}$ for low ice concentrations. In the case of radiance emitted from pure water ice, which is assumed to scatter light in a Lambertian manner, the viewing geometry will be of less consequence. Still, being able to separate out the effects of the observational geometry on the photometric signal is necessary in order to accurately interpret compositional differences. To demonstrate the effects of illumination/viewing geometry on the surface brightness variability, the camera was placed at six separate locations along the crater rim, spaced in 60° azimuthal increments, and the radiance was modeled for ice concentrations varying from 0% (dry regolith) to 100% (pure water ice) at the summer diurnal peak when illumination is maximized. Figure 3.24 displays the product of this modelling for Faustini crater, where data are shown as ratios between the non-absorption band (visible), and the three water ice absorption regions in panels a, b and c. Histograms of the phase angle distribution for each pointing are given in panel d.

Beginning with the vis/UV, the obtained brightness ratios are large due to discrepancies between the FUV and visible solar flux as well as albedo differences in the two spectral channels. For the 0° and 300° azimuthal pointings, where low phase angles are dominant, the vis/UV ratio increases exponentially as water ice is added to the signal. At a 180° pointing, in contrast, where the viewing geometry favors larger phase angles in the range of 100°–120°, the ratio increase is approximately linear. What is observed here is a shift in the relative brightness of ice and regolith at FUV wavelengths due to observational effects. At low phase angle geometries, the dry lunar surface appears brighter than water due to the enhanced FUV backscattering of regolith particles (see Figure 3.8), and therefore the surface brightness decreases with increasing water under these circumstances. The opposite is true, however, at the 180°

azimuthal pointing and other observing geometries for which low phase angles are not encountered; in these situations, the FUV surface brightness may remain constant or even increase with ice fraction depending on the photometric alignment. The large separation between the observed brightness ratios at different observational geometries – particularly for intermediate ice-regolith mixtures – significantly complicates the retrieval of water ice abundance from remote sensing data, and demonstrates the need for accurate photometric correction techniques as well as detailed laboratory studies to validate modeling results.

Unlike the FUV ratios, the expected vis/IR ratios for ice-bearing mixtures will depend on the size of the scattering ice particle given that larger ice grains appear darker at 1500 nm and 2000 nm. For 5 μm to 20 μm grain sizes, the vis/IR$_{1500\ \mathrm{nm}}$ ratios increase with ice content, although the rate of increase declines as the signal approaches pure water ice. This is also true for the vis/IR$_{2000\ \mathrm{nm}}$ ratios modeled for the 5 μm grain size, however moving toward larger particle sizes, the relationship shifts to an exponential as the relative ice-regolith brightness changes due to ice darkening. Relative to the vis/FUV, only subtle differences in the observed ratios are found owing to measurement geometric effects, however larger separations are still present at intermediate ice-regolith mixtures.

3.4.2 Signal-to-Noise Ratios

The primary challenge with imaging in low-light environments is elevating the desired signal above the background noise. The signal-to-noise ratio (SNR) of a particular observation will depend on the lighting conditions in addition to a number of factors pertaining to the camera's detector and optical assembly. With respect to the camera's detector, the quantum efficiency (QE), thermal response and the size and full well capacity of each pixel are among the most important factors that dictate the SNR of an image. As for the optics, the pupil diameter and focal length of the lens will govern the amount of light reaching the sensor, and will therefore contribute to the SNR.

The signal for a single pixel, S, measured in electron counts can be written as:

$$S = \frac{I_{\lambda,Mix}(i,e,\alpha)\sigma_{lens}\Omega_{pixel}QE_{\lambda}\Delta t}{\nu_{\lambda}}, \tag{3.10}$$

where σ_{lens} is the area of the entrance pupil, Ω_{pixel} is the solid angle of a pixel, QE_{λ} is the quantum efficiency of the sensor, Δt is the integration time and ν_{λ} is the energy of a single photon at the central wavelength of the band pass. The SNR of a pixel is then given by:

$$SNR = \frac{S}{\sqrt{S + N_D\Delta t + N_R^2}}. \tag{3.11}$$

In the denominator are the noise sources, where $\sqrt{S}$ is the photon noise, N_D is the dark current and N_R is the read noise.

While the SNR achievable will vary significantly depending on the choice of sensor and optics, it is nonetheless instructive to model the performance of a camera imaging the PSR floor given the available upwelling photon flux. We begin with the performance of the FUV camera described in the companion work of Godin et al. (2020), which utilizes a Ly-α filter (20 nm FWHM) along with a Sony IMX249 CMOS chip with a large full well capacity (FW = 33,000 e$^-$) and a QE of $\sim$35% at Ly-α wavelengths. In front of the camera is a $f/2.4$ MgF_2 lens with a 44 mm focal length at 121 nm and a 12.5° $\times$ 16° field of view. The same optical parameters are assumed for the visible and IR image bands, but the QE is adjusted to reflect the differing photosensitivity of image sensors in these regimes: To be conservative, we use a QE = 80% for the visible and QE = 60% for the IR bands. The expected SNR for this camera system, imaging the floor of Faustini crater at the summer diurnal peak when scattered solar illumination is maximized, is plotted as a function of integration time in Figure 3.25 for signals consisting of 0%–100% ice. Here, we assume N_D is negligible (justified if the sensor is sufficiently cooled or if the rover is operating in shadow) and a read noise of $N_R = 10$ e$^-$.

In the FUV where a camera is photon-limited, the SNR approaches 10–20 at integration times of $\sim$17 minutes depending on the fractional ice concentration. In theory, the exposure duration could be increased beyond 17 minutes owing to the static location of the rover and the slow rotation of the Moon. The SNR could also be improved by increasing the light gathering power of the lens or through use of processing techniques such as image stacking or deconvolution. Still, the SNR attainable with an FUV camera is diminished with respect to the visible and IR, where the number of available photons is significantly enhanced. As shown in Figure 3.25, even for short integration times (0.1 – 1s), the maximum SNR of the sensor, given approximately as $\mathrm{SNR}_{\mathrm{max}} \approx FW/\sqrt{FW} \approx 181$, is reached. It is important to recall that these SNRs are modeled at the summer diurnal peak when conditions are optimized, and thus represent best-case scenarios. For the visible and IR bands, however, the modeled quantities are not highly sensitive to seasonal variations. To take the extreme case at the winter diurnal peak, integration times of 0.4–3 seconds are needed to reach $\mathrm{SNR}_{\mathrm{max}}$. In contrast the FUV band is more sensitive to temporal changes, with an SNR of $\sim$2 being reached at the winter diurnal peak for a 17 minute exposure and a 100% ice signal.

The choice of wavelength regions for detecting water ice and other volatiles in permanently-shadowed regions can take advantage of the fact that different materials have absorption bands in specific regions. For the Moon, the major minerals and their associated absorption bands are in the 900-1100 and 1900-2200 nm regions (pyroxene), the 800-1300 nm region (olivine), and the 1300 nm region (plagioclase feldspar) (e.g., Pieters and Mustard (1988)). The use of these wavelength regions must therefore account for their possible spectrum-altering effects. Of the wavelengths selected for Lunar Flashlight and VMMO, the 1500 nm region lies outside of mineral absorption bands; thus, an absorption band in this region (e.g., 1495 nm: Lunar Flashlight; 1560 nm: VMMO) is most likely associated with water ice.

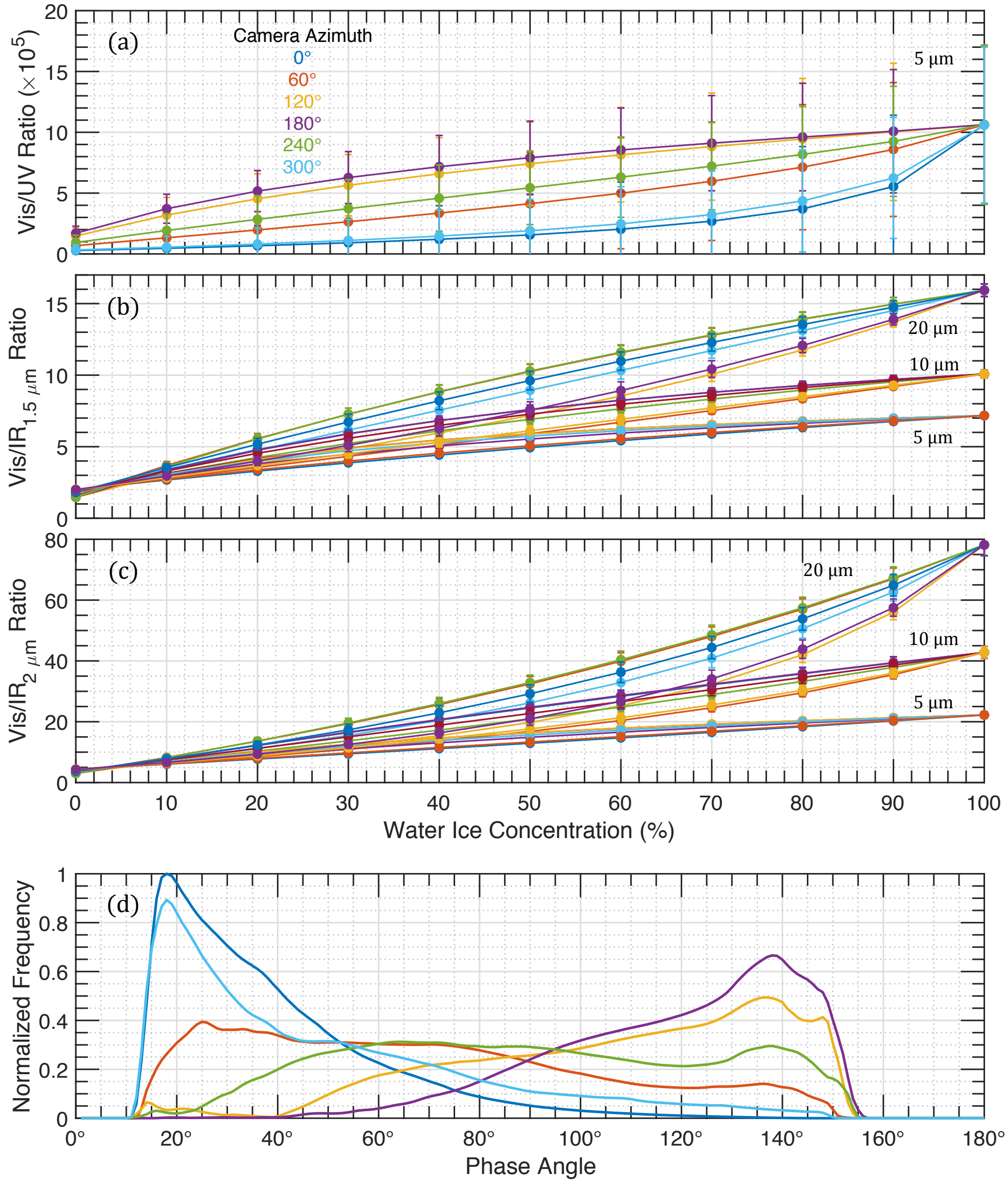

Figure 3.24: Panels (a), (b) and (c): modeled ratios of the visible radiance to the FUV and IR radiance for varying concentrations of water ice within Faustini crater. Each colored curve corresponds to the radiance received at a separate azimuthal placement of a camera along the crater rim, color coded in panel a; each set of curves in panels (b) and (c) represents a modeled water ice grain size. The model was performed at the summer diurnal peak when scattered sunlight is maximized. Data points represent a mean of the PSR area with 1σ error bars. Panel (d) shows the phase angle distribution associated with each pointing, where angles are binned in 1° increments.

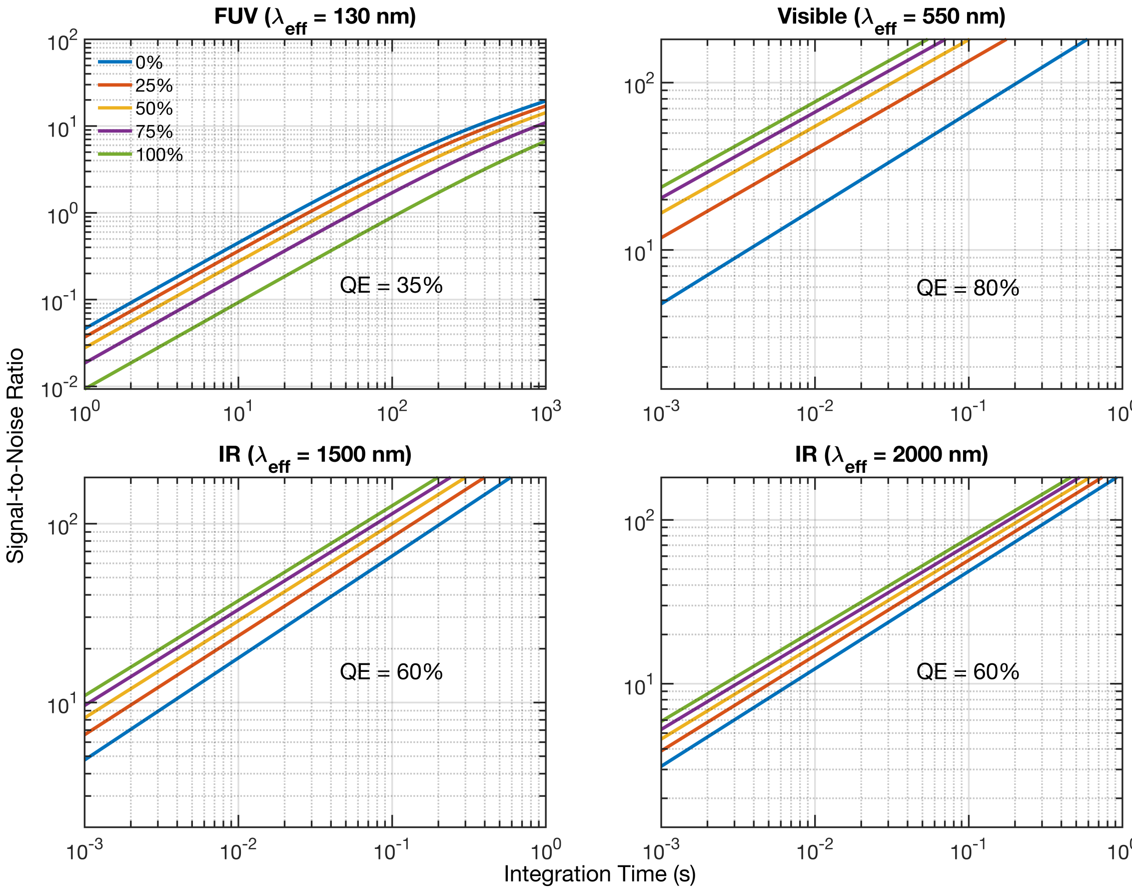

Figure 3.25: Modeled signal-to-noise ratios for various ice-regolith mixtures as a function of camera integration time. Data are modeled for a camera imaging the floor of Faustini crater at the summer diurnal peak and a 0° azimuthal pointing. For all image bands shown, a $f/2.4$, 44 mm focal length optical lens is assumed as is used in the frost detection laboratory experiments of Godin et al. (2020). The QE of the FUV, Visible and IR image bands, however, vary, with assumed values of 35%, 80% and 60%, respectively. Note that the x-axis and y-axis limits differ for each panel. In the vis and IR bands, the upper limit of y-axis is clipped at the maximum SNR of the sensor $SNR_{max} \approx 181$.

4 Examining the PSR Surface Reflectivity Using Long-Exposure NAC Imagery

4.1 Chapter Overview

As shown in the previous chapter, detailed radiometric models can provide valuable information about the illumination conditions of a planetary surface; these tools, however, are also useful in that they facilitate analysis from planetary image data sets (Mazarico, Barker, & Nicholas, 2018). For example, using radiometrically calibrated images of a planetary surface, the relative brightness (i.e. reflectance) of the surface can be derived using a photometric normalization technique. Common in planetary science (Hapke, 2012), this technique entails correcting an image for illumination effects such that, upon correction, each pixel appears to be illuminated and viewed at the same geometry. Sato et al. (2014) describes a large-scale effort to characterize the photometric response of the lunar surface using this technique.

An intriguing yet challenging data set with which to apply this photometric method are images of permanently shadowed regions captured by the Narrow Angle Cameras (NACs) (Robinson et al., 2010) on LRO. Although not designed to image shadowed areas, NAC is capable of observing PSRs illuminated at low luminosities by sunlight scattered from the nearby, sun-facing topography. As a result of a dedicated campaign to observe PSRs, as of 1 July 2018 a total of 6,108 NAC observations have been acquired, with good spatial coverage of north and south polar craters (Cisneros & the LROC Team). As the primary source of natural illumination (scattered sunlight) for PSRs is diffuse and emanates from an extended solid angle, photometrically correcting a NAC image of a PSR entails independently accounting for each scattering event that is delivering flux to the imaged target. This is significantly more complex than for directly illuminated surfaces which are principally illuminated by a single source (the Sun) and from a single direction (assuming a point source).

Here, we describe an attempt to photometrically correct NAC PSR images through employing the previously described radiative transfer model in an adapted form. The goal of this work is to examine the PSR surface brightness, which many previous data sets have indicated is, on average, brighter than the adjacent sunlit regions as a result of exposed frost (Fisher et al., 2017; Lucey et al., 2014; Qiao et al., 2019). This chapter will begin with an overview of the relevant NAC data set, and will then move to discuss the modifications made to the radiative transfer model that were necessary to perform this work, and then the incipient results.

4.2 Data and Model

4.2.1 Long-Exposure Narrow Angle Camera Images

Among the science instruments carried by LRO are the Lunar Reconnaissance Orbiter Cameras (LROC), which consists of three imaging subsystems: two NACs (NAC-L and NAC-R) and one multispectral Wide Angle Camera (WAC) (Robinson et al., 2010). The NACs, which are used in this work, are monochrome push-broom scanners with typical resolution capabilities of 0.5 m pixel^{-1} for directly illuminated surfaces at the nominal 50 km orbital altitude. While not designed to image shadowed surfaces, NAC is able to observe PSRs at reduced SNRs and image scales; however, in order to accomplish this, observations must be taken at or near periods of maximum secondary illumination, and, furthermore, must utilize extended integration times: while nominal exposures range between 0.7 and 2.0 ms, long-exposure observations require up to 24.2 ms exposures (Mitchell et al., 2018). This increased exposure results in a number of undesired side effects. One significant example is an image smear in the downtrack direction, which produces elongated pixels and decreases the overall image resolution to ∼10–20 m pixel^{-1}. To correct for this effect, prior to uplink to the Planetary Data System, the images are subject to binning in the crosstrack direction using ISIS routines to create a square aspect ratio for each pixel. This binning has the added benefit of increasing the SNR of each pixel. An additional, unwanted consequence of the extended integration is blooming of saturated, sunlit terrain pixels onto the neighboring, indirectly-lit PSR pixels in the cross-track direction. For quantitative analyses, such as that attempted here, these pixels are especially problematic as they contain no usable information. Thus, in the analysis described below, saturated pixels are identified using a brightness threshold of $I/F > 0.005$ as prescribed in the LROC PSR Atlas (Cisneros & the LROC Team), and are excluded from the analysis.

In this study, we consider 44 craters (21 in the north, 23 in the south) containing large (>10 km^2), contiguous regions of permanent shadow for which long-exposure observations have been acquired (Table 4.1). NAC images for each crater are downloaded from the Planetary Data System, resampled from their original resolution to match that of the digital elevation model used in this work (240 m/pix) and subsequently projected onto a polar stereographic map. Based on pre-flight calibration (Robinson et al., 2010), images contain radiometric units of I/F, defined as the radiance received at a particular illumination/viewing geometry divided by the radiance of an ideal Lambertian surface illuminated at $i = 0°$. The term I/F is also referred to as the radiance factor by Hapke (2012), and can be interpreted as the reflectivity of the surface relative to an ideal standard.

Table 4.1: Summary of the NAC long-exposure data set.

Crater	[a]Latitude (deg)	[a]Longitude (deg)	# of NAC Images	PSR Coverage (%)
		Northern Hemisphere		
Bosch	86.8 N	133.5 E	3	100
Erlanger	87.0 N	28.6 E	11	100
Fibiger	86.1 N	37.1 E	11	100
Gore	86.2 N	62.3 W	2	100
Grignard	84.5 N	75.8 W	8	100
Hermite A	87.9 N	51.0 W	14	100
Lenard	85.2 N	109.7 W	6	88.7
Lovelace	82.1 N	109.5 W	28	100
Lovelace E	82.0 N	96.8 W	8	100
Main L	81.4 N	22.7 E	6	100
Nansen A	82.8 N	65.0 E	12	100
Nansen F	85.0 N	62.4 E	22	100
Plaskett S	81.0 N	150.6 E	10	100
Plaskett U	82.4 N	162.3 E	14	100
Plaskett V	82.2 N	120.9 E	14	100
Rozhdestvenskiy K	82.2 N	147.0 W	17	100
Rozhdestvenskiy N	84.0 N	156.5 W	2	54.4
Rozhdestvenskiy U	84.9 N	152.1 E	19	100
Sylvester	82.7 N	81.2 W	14	100
Sylvester N	82.4 N	68.7 W	9	100
Whipple	89.1 N	120.0 E	4	100
		Southern Hemisphere		
Amundsen	84.4 S	83.1 E	40	37.2
Cabeus	85.3 S	42.1 W	71	78.3
Cabeus B	82.3 S	54.6 W	35	100
de Gerlache	88.5 S	88.3 W	56	100
Faustini	87.2 S	84.3 E	44	100
Haworth	87.5 S	5.2 W	42	63.0
Haworth Lowlands	86.6 S	25.2 E	30	94.5
Ibn Bajja	86.3 S	75.0 W	32	100
Idel'son L	84.0 S	118.6 E	55	100
Kocher	84.5 S	134.0 W	19	100
Kuhn	84.5 S	152.5 W	9	100
Malapert	85.0 S	11.4 E	47	99.4
Nobile	85.3 S	53.3 E	63	97.2
Shackleton	89.7 S	129.8 E	8	86.8
Shoemaker	88.1 S	45.9 E	53	94.0
Svedberg	81.7 S	65.2 E	14	91.9
Sverdrup	88.3 S	153.4 W	58	99.5
von Baeyer	81.8 S	61.9 E	14	100
Wiechert	84.0 S	164.7 E	117	100
Wiechert E	83.6 S	176.0 E	23	100
Wiechert J	85.2 S	177.6 W	54	100
Wiechert P	85.1 S	151.8 E	29	100
Wiechert U	83.4 S	149.0 E	45	100

[a]According to the United States Geological Survey.

4.2.2 Illumination Model of Scattered Sunlight

To generate synthetic NAC PSR images, the radiative transfer model described in Chapter 3 is modified to incorporate a second bounce of reflected sunlight and a non-stationary observer. For each of the examined images, the procedure begins by extracting from the image header the exposure time, camera (NAC-L or NAC-R), observation start and stop time (converted from UTC to a Julian date) and image dimensions (specified by line and sample numbers, referring to the height and width of the image, respectively). The observation start time and exposure time are used to construct an array which specifies the Julian date at which each line of the image was acquired, and, with this information, the surface intercept point of the boresight and FOV boundary vectors are computed for a smooth surface, corrected for one-way light time using the SPICE toolkit by NASA's Navigation and Ancillary Information Facility (NAIF; Acton Jr, 1996). A map-projected footprint for each image is constructed by casting great circle arcs between right and left FOV boundary points for each line sample to acquire the intermediate image coordinates.

Using the mid-point of the observation, the direct solar irradiance received by the light scattering terrain is computed as before; however, here, for improved accuracy the solar disk fraction is ascertained using a ray-tracing technique in place of the horizon method. Using equations 3.2 and 3.6, the radiance scattered toward the imaged surface is evaluated, where non-PSR regions of the image were excluded from the calculation using the PSR boundaries charted by Mazarico et al. (2011). The process is then duplicated: the radiance is computed for a second bounce of light from the PSR to the NAC using the position of the LRO spacecraft and the boresight of the camera vector at each line epoch. In this way, synthetic images are assembled line-by-line to replicate the exact scattering geometry of the observation. The modeled radiance emitted from a given PSR element and received at the camera, $I_{\lambda,Model}$, can be can be written as:

$$I_{\lambda,Model} = \sum_{n=1}^{N} I_{\lambda,n}(i,e,\alpha)\Omega_n r(i_p,e_p,\alpha_p), \tag{4.1}$$

where N is the number of light scattering elements for the PSR, $I_{\lambda,n}(i,e,\alpha)$ is radiance scattered toward the PSR, Ω_n is the projected solid angle of the light scattering terrain element with respect to the PSR (corrected for map distortion), and the angles i_p, e_p and α_p are, respectively, the incidence, emission and phase angles measured from the PSR surface normal. Hapke parameters were obtained from Sato et al. (2014) for the central wavelength of the NAC bandpass (600 nm). Here we use an increased K value of 1.25 as recommended by Ohtake et al. (2010) and Hapke and Sato (2016). The modeled I/F is then simply computed as

$${}^{I}\!/_{F}{}_{Model} = \frac{\pi I_{\lambda,Model}}{F_0}, \tag{4.2}$$

and the photometrically normalized NAC image, corrected for illumination effects, is

$$n{}^{I}\!/\!{}_{F} = \frac{{}^{I}\!/\!{}_{F}{}_{NAC}}{{}^{I}\!/\!{}_{F}{}_{Model}} {}^{I}\!/\!{}_{F}{}_{Std}, \tag{4.3}$$

where ${}^{I}\!/\!{}_{F}{}_{Std}$ is the I/F modeled at a standard viewing geometry ($i = \alpha = 30°$, $e = 0°$).

For the sake of completeness, Earthshine was also included in the model, although for the majority of observations it does not contribute significant radiation to the targeted areas – both because its PSR coverage is low and because NAC observations were coordinated to occur at periods of maximum secondary illumination from the Sun.

4.3 Initial Results

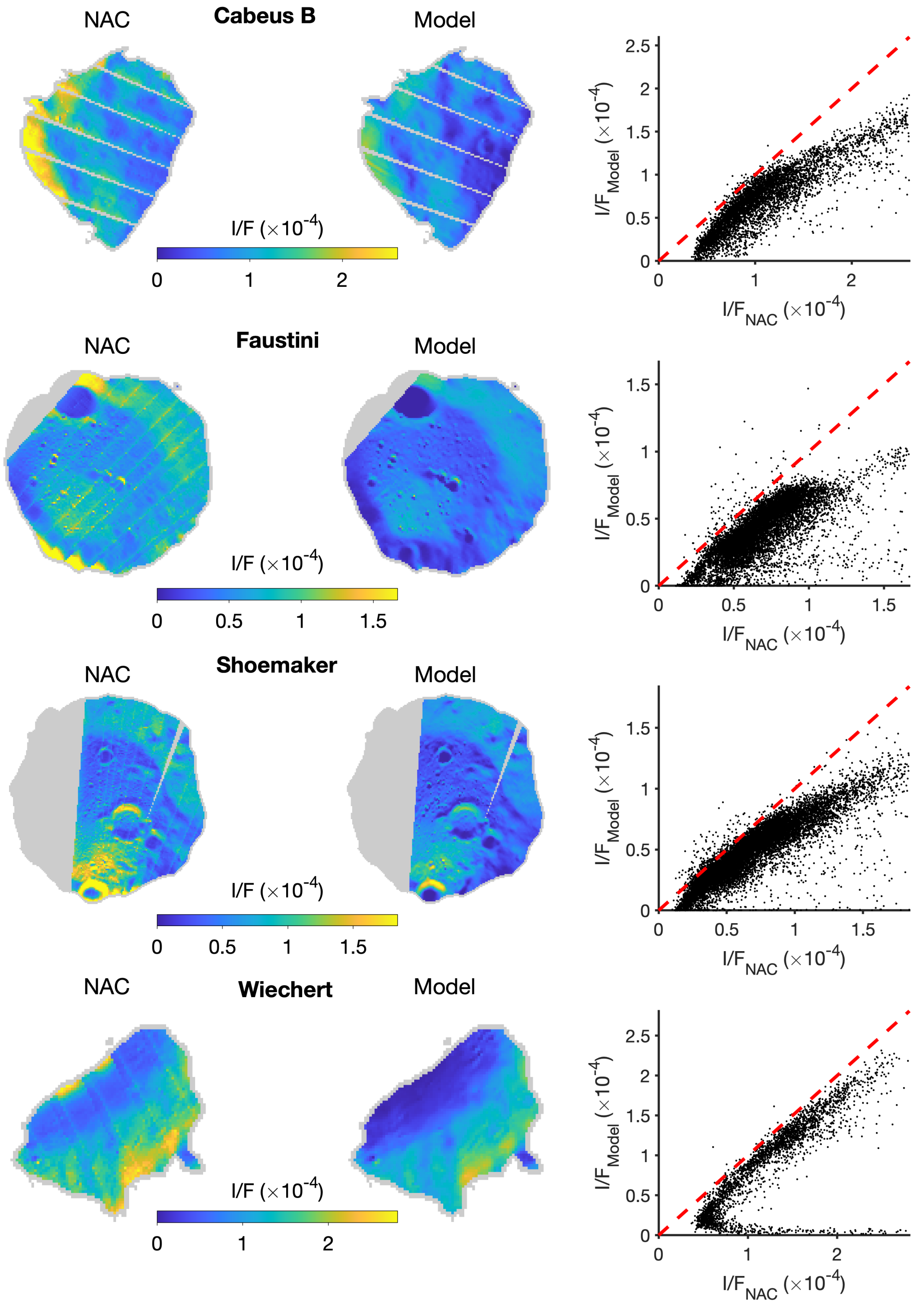

Figure 4.1: Left column: PSR mosaics created using a series of long-exposure NAC images acquired within 24 hour period. Images were resampled from their original resolution of ∼10 m/pixel to 240 m/pix (the DEM resolution). The gray shaded region represents the PSR within the crater. Center column: PSR mosaics created using an illumination model. Individual images were modeled independently and subsequently assembled into a mosaic. Right column: Direct comparison of I/F_{NAC} and I/F_{Model} showing good linearity, however I/F_{NAC} is consistently larger than I/F_{Model}. The red dashed line shows a one-to-one relationship.

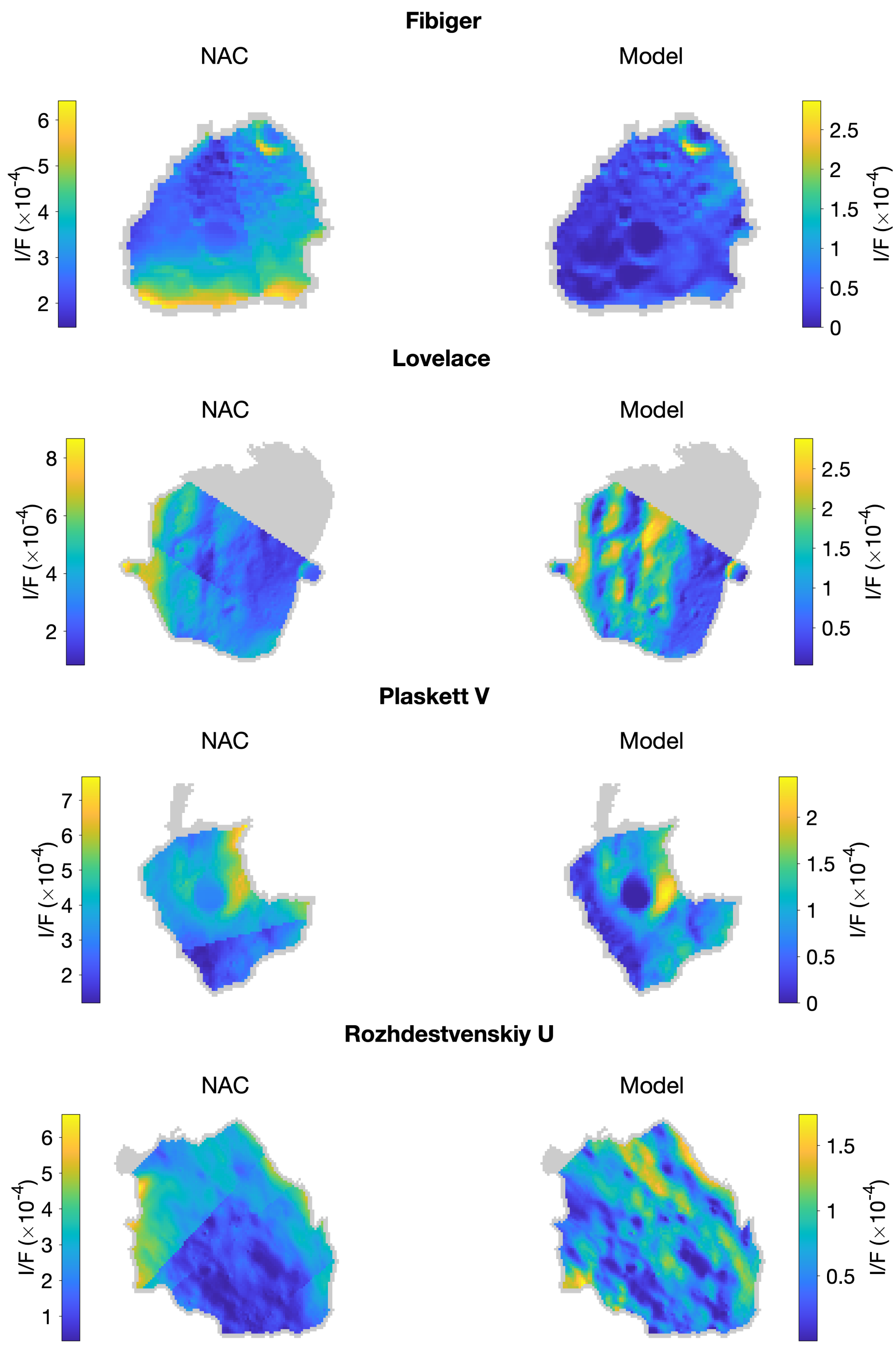

Figure 4.2: Left column: PSR mosaics created using a series of NAC long exposure images showing stray light contamination. The gray shaded region represents the PSR within the crater. Right column: PSR mosaics created using an illumination model. Individual images were modeled independently and subsequently assembled into a mosaic.

Figure 4.1 shows selected NAC long-exposure mosaics for four south polar craters. Each mosaic was assembled using a series of observations acquired within a 24-hr period on consecutive orbits, where, due to the slow rotation of the Moon, the illumination is effectively constant. Saturation is evident within some boundary locations due to pixel bleeding from the adjacent sunlit areas, such as in the lower left region of Faustini. To minimize this effect, concentric rings containing the outermost 10 PSR pixels for each crater were removed and discarded from the subsequent analysis. The center column of Figure 4.1 provides the corresponding modeled data for the same craters. With respect to the spatial intensity, the modeled intensity shows good agreement with the NAC observations; however, it is clear that the modeled brightness is consistently decreased relative to that of the NAC. This effect can be more visibly observed by directly comparing the NAC and model pixel values, as is shown in the rightmost column. Although reasonably good linearity is observed, $\mathrm{I/F_{NAC}}$ consistently exceeds $\mathrm{I/F_{Model}}$, suggesting that illumination model is systematically under-predicting the radiance scattered toward the camera. This may be explained by a combination of several factors: (1) the brightness of the NAC images are augmented with out-of-field stray light, (2) sunlit areas scattering light into the crater are more highly reflective than modeled, perhaps due to regional differences in surface composition and (3) the PSR surface is more highly reflective than the surrounding sunlit areas, from which the Hapke model parameters (notably the single scattering albedo) are derived. The latter has been demonstrated by LOLA zero-phase albedo measurements at 1,064 nm which show systematically higher reflectivity within PSRs, interpreted to be the result of the presence of highly reflective water ice (Fisher et al., 2017; Lucey et al., 2014; Qiao et al., 2019). As for the former, however, signatures of stray light contamination are evident in a number of images; Figure 4.2 displays several craters for which this is the case.

Generally, out-of-field stray light manifests in two ways. The first is as a decrease in the overall image contrast, where the images appear washed out. This manifestation is apparent in craters Fibiger, Plaskett V and Rozhdestvenskiy U shown in Figure 4.2. The second is as a discontinuity between image boundaries in the crosstrack dimension, which is evident in all craters shown. While it may be feasible that images collected at two different times of day differ in brightness, the slow rotation of the Moon, coupled with the fact that these images were acquired on consecutive orbits (where image spacing is only a couple of hours), should ensure a smooth brightness transition moving across image boundaries (as is modeled). Through manual examination of the image mosaics, it was found that data within all north polar craters and eight south polar craters exhibited clear signs of stray light contamination, and, as such, were excluded from the analysis. In total there are 16 craters with image sets that were deemed valid; these craters are emboldened in Table 4.1. Although these data did not manifestly show signs of contamination, we recognize that stray light may still exist in small quantities or uniformly within the images. The uncertainty due to stray light contamination will be discussed further in sections 4.4 and 4.5.

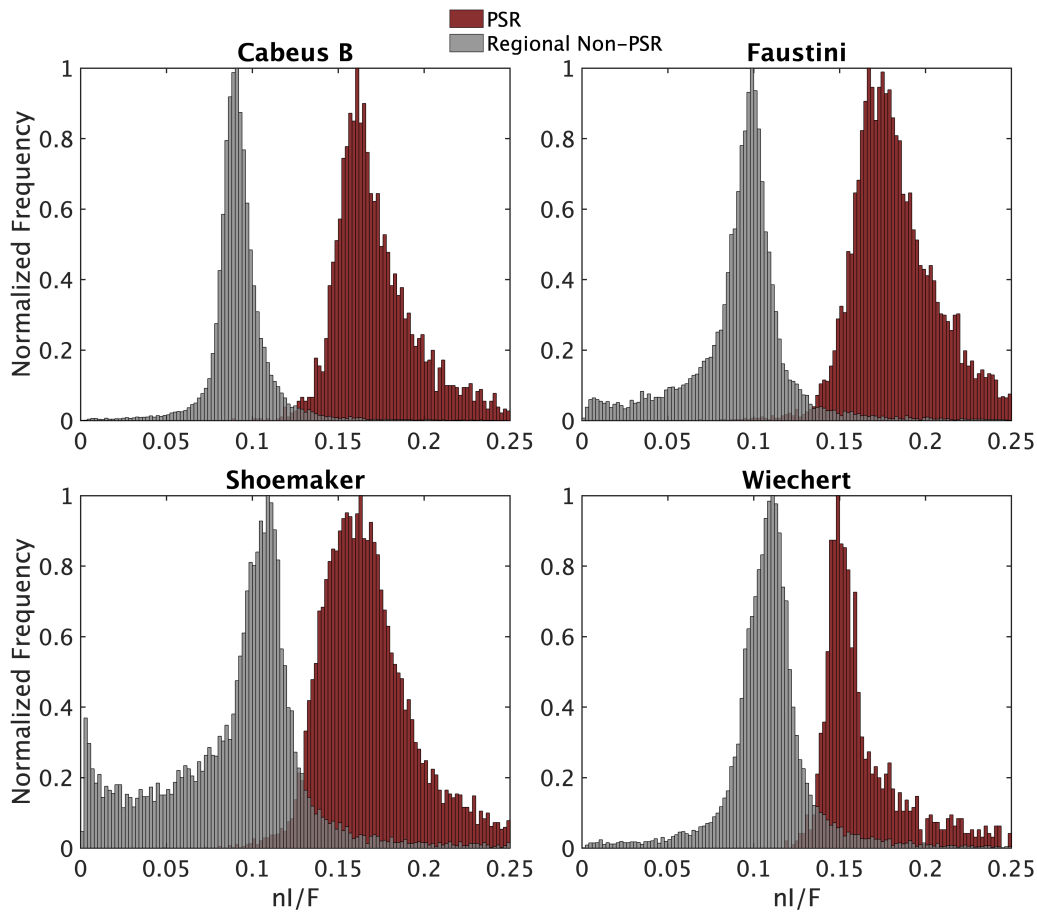

Figure 4.3: Histogram comparing the normalized I/F of the PSR with the regional non-PSR (area encircling the crater with an extended radius of 5 km) for selected craters. Data were filtered by excluding slopes larger than 20° and pixels illuminated at high incidence angles ($i > 85°$). Boundary PSR pixels were also excluded as they are subject to pixel bleeding from the adjacent sunlit pixels.

Valid image sets were subjected to further analysis to study variations in the surface reflectance. To account for the existing regional changes in surface composition and albedo at the polar regions, we compare the nI/F of the PSR with the nI/F of the nearby sunlit areas (Figure 4.3) – a technique used in similar assessments (i.e. Fisher et al. (2017), Qiao et al. (2019)). The regional, non-PSR nI/F data were obtained using polar NAC images acquired within an area encircling the crater using an extended radius of 5 km from the rim. To reduce uncertainty, images were filtered to exclude pixels that are illuminated at high incidence angles (>85°) as well as pixels with steep slopes (>10°), which may be enhanced in brightness due to the effect of mass wasting. NAC images were photometrically corrected using modeled illumination images generated using the procedure described above. As is shown here, PSRs are, on average, brighter than their surroundings, although overlap is observed in the tail-ends of the histograms. For example, using the median nI/F values, the Faustini permanently shadowed region is 1.8× brighter than the surrounding sunlit area. Figure 4.4 plots the PSR/non-PSR nI/F ratio for other craters, which show similar brightness offsets, ranging from 1.4 to 2.2.

One factor that could contribute to this discrepancy is PSR/non-PSR compositional differences, which will be examined further in section 4.4. Such a large reflectance differential, however, is unexpected based on LOLA data, where only a 15% PSR albedo enhancement is observed (Qiao et al., 2019). Part of the disagreement between our measurements and LOLA data could be the result of stray light contamination of the NAC images, although other parameters in the bi-directional reflectance model, such the single scattering albedo or the regolith porosity may also contribute to the disagreement. As a result of these uncertainties, we felt it necessary to compare our results to established data sets. In the lower panel of Figure 4.4, the nI/F brightness variations are compared with LOLA albedo PSR/non-PSR ratios using data from Lemelin et al. (2016); here the nI/F ratios and LOLA ratios are normalized to their respective means in order to compare their relative amplitudes. With some exceptions (i.e. Haworth, Idel'Son L, Nobile and Wiechert), the data show moderately good qualitative agreement. Craters with larger LOLA–nI/F discrepancies, such as Haworth, Nobile and Idel'Son L, tend to have larger nI/F ratios (>2), possibly indicating larger amounts of stray light in these craters. This trend, however, does not hold for Wiechert crater.

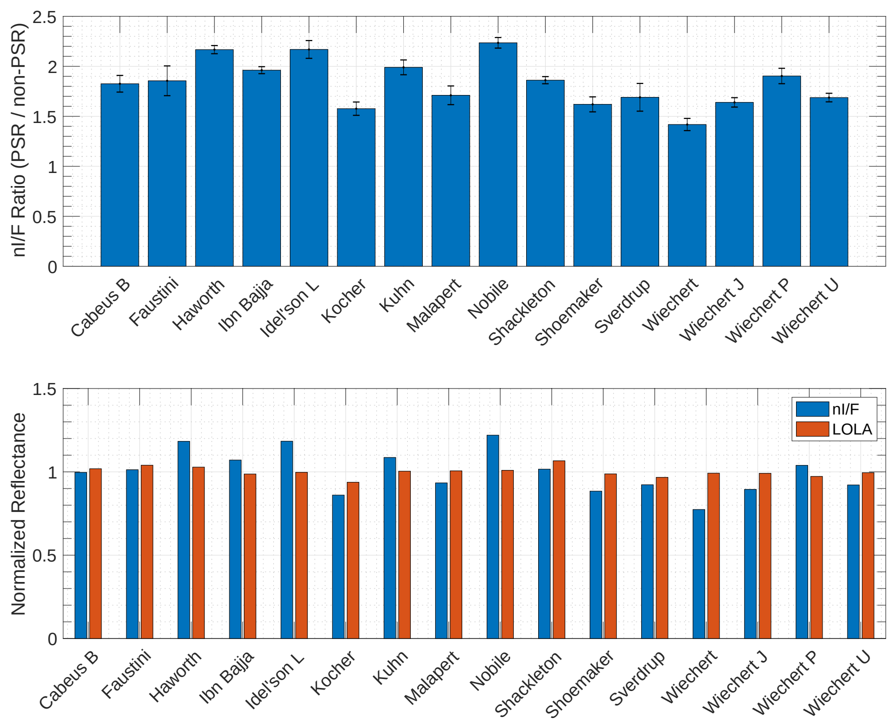

Figure 4.4: (Top) Ratio of PSR-derived nI/F and non-PSR-derived nI/F for craters containing valid image sets. Error bars represent 95% confidence intervals. (Bottom) Comparison of nI/F ratio with LOLA PSR/non-PSR albedo ratios using data from Lemelin et al. (2016). Each data set is normalized by the respective mean.

4.4 Modeling Ice-Regolith Mixtures

The enhanced brightness of PSRs has been explained by the presence of water ice, although decreased space weathering has also been proposed as a contributing factor (Lucey et al., 2014; Qiao et al., 2019). Here we explore the possibility that the enhanced brightness of the NAC images (as in Figures 4.1 and 4.3) is due to the presence of water ice. To estimate the concentration of ice that would explain the NAC/model discrepancy, we compute the radiance scattered by a patch of pure water ice, I_{λ,H_2O}, using an assumption of Lambertian scattering (equation 3.8) and a directional hemispheric ice albedo of 0.9. Assuming a linear mixing model (equation 3.9), the fraction of ice needed to explain the NAC/Model disparity, σ_i, can be written as:

$$\sigma_i = \frac{I_{\lambda,Model} - I_{\lambda,NAC}}{I_{\lambda,Model} - I_{\lambda,H_2O}}. \tag{4.4}$$

Calculations of ice abundance are made on a pixel-by-pixel basis, and pixels with repeated observations are reported using a median value.

Due to the exponential relationship between surface temperature and the sublimation loss rate, ice has been reported to exist in higher abundances on surfaces with lower maximum surface temperatures (Fisher et al., 2017; Hayne et al., 2015). To search for this volatile signature, we utilize publicly available, 240 m pixel^{-1} resolution bolometric brightness temperature maps of the north and south polar regions from the Diviner Lunar Radiometer instrument on LRO (Figure 4.5) (Williams et al., 2019). The maps employed in this work record the maximum surface temperature during the summer season, defined by Williams et al. (2019) to be the temporal period when the subsolar latitude is above or below the equator for each pole. These temperatures are interpreted to be annual maximum temperatures.

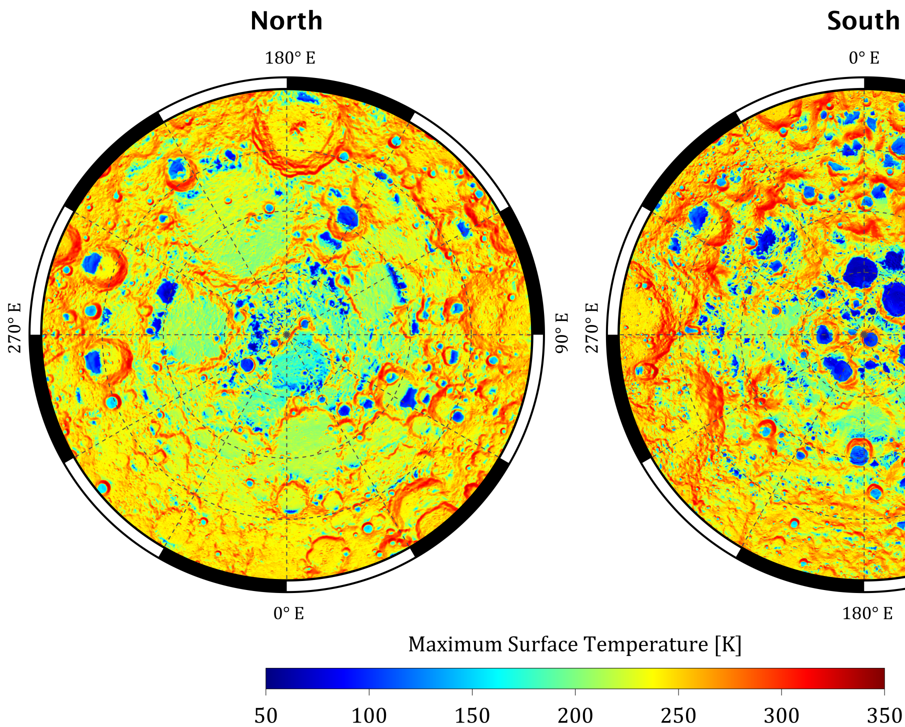

Figure 4.5: Diviner maximum temperatures at the north and south pole. Data are derived from Williams et al. (2019) and are shown for locations poleward of ±80°.

Figure 4.6 plots the modeled ice concentration as a function of maximum temperature for three selected craters at the south pole: Cabeus B, Faustini and Wiechert. These results, consistent with the other craters examined, show that ice concentrations in the range of 0 to 30% may explain the NAC-model brightness differential. This concentration level is in agreement with previous estimates, which range from 1-10% in far ultraviolet spectroscopic measurements (Gladstone et al., 2012; Hayne

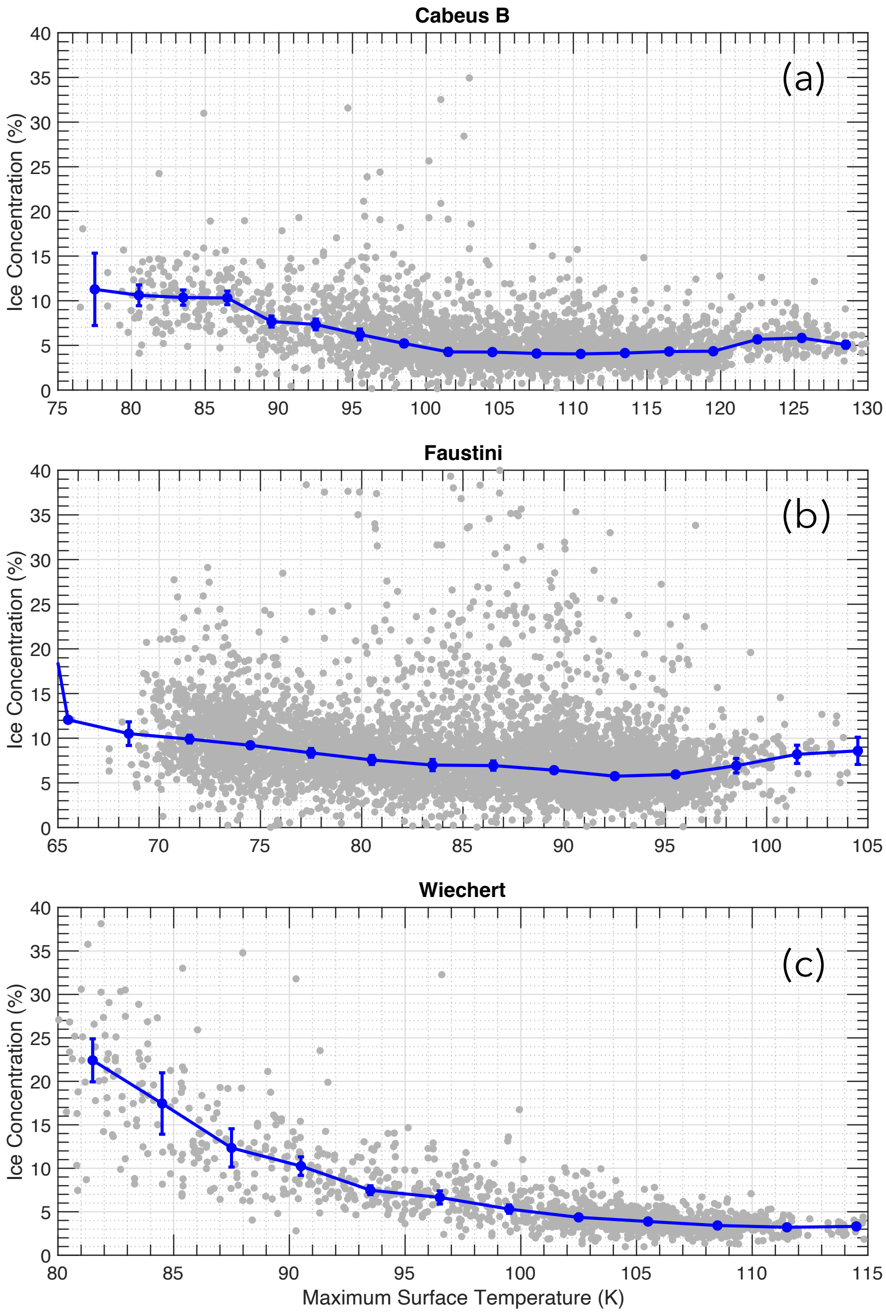

Figure 4.6: Modeled ice concentration vs. annual maximum surface temperature for Cabeus B, Faustini and Wiechert craters at the south pole. Gray dots show individual measurements and the blue line shows the binned data using a 3 K bin width and 95% confidence intervals.

et al., 2015), to up to 30% in IR data sets (Li et al., 2018). Interestingly, within Cabeus B and Wiechert, colder temperatures are correlated with increased ice concentration at $T < 100$ K. This behavior, consistent with the presence of water ice, has been observed in the aggregate for lunar south polar PSRs (Fisher et al., 2017), although it has yet to be observed within individual craters containing permanent shadow. We note, however, that while all PSRs examined are enhanced in brightness relative to their surroundings, this temperature-reflectance behavior is only observed in these two cases. The remaining craters, such as Faustini (Figure 4.6b), do not exhibit a clear temperature-reflectance correlation.

4.5 Uncertainties

There are a number of uncertainties associated with this work, and it is important to address them. To start, and perhaps most significantly, the identification of out-of-field stray light, without a means of accounting for its presence, disallows a large percentage of the data set to be quantitatively examined. Moreover, even in observations which do not appear to be contaminated with stray light, it cannot be definitively concluded that stray light does not manifest homogeneously or in small quantities. As such, the values of ice abundance reported in this work should be interpreted as upper limits, as any amount of stray light would decrease the modeled ice concentration. This is not unreasonable, as our estimates are already approaching or at the upper limits of ice abundance reported in the literature (Li et al., 2018).

The photometric response of lunar regolith and ice-regolith mixtures described above are predicated on comparable scattering properties of PSR and non-PSR regolith, however the PSR regolith may look different from the non-permanently shadowed terrain as it is affected by different processes. For example, PSRs experience less space weathering, which will affect composition and abundance of nano-phase iron oxide; this may, at least in part, explain why PSRs are anomalously bright in relation to sunlit areas (Lucey et al., 2014; Qiao et al., 2019). In addition, more extensive sublimation/condensation (Andreas, 2007) as well as reduced thermal diurnal cycling (Metzger, Anderson, & Colaprete, 2014) will affect particle packing/porosity of the upper regolith, leading to a more porous regolith as has been observed by LAMP (Gladstone et al., 2012). These factors together could indicate unique scattering properties of the PSR regolith.

Finally, the resolution of the polar digital elevation models used in this work are relatively coarse. While future work will examine the influence of the DEM resolution of the results reported here, it is worth briefly speculating on the expected outcomes. First, higher resolution DEMs will enable the illumination to more accurately mapped, which will predominantly affect the surface regions near shadow/light boundaries. As well, improved spatial resolution will facilitate image/model comparisons – particularly differentiation of albedo variations which result from geologic processes (i.e. mass wasting and impact ejecta) versus those that are due to volatile enrichment.

5 The Temporal and Geographic Extent of Seasonal Cold Trapping on the Moon

5.1 Chapter Overview

The small obliquity of the Moon gives rise to a seasonal variation in solar insolation that oscillates with a period of 346.6 days, or one draconic year[1] (Figure 5.1) (Paige et al., 2010). As a result of topography, shadowed area near the rotational poles may vary significantly across this time interval. Seasonally shadowed regions (SSRs), defined here to be a region of the surface that remains continuously in shadow for at least one lunation, are significant due to their expected low temperatures, and may

[1]A draconic year, also referred to as an eclipse year, is defined as the length of time for the Sun, as viewed from the Earth, to complete one revolution with respect to the same lunar node (i.e. either the longitude of the ascending node or the longitude of the descending node), and is related to the lunar nodal precession. On average, it takes 18.6 years for the longitude of the ascending node to complete one revolution, and, as such, the time taken for the Sun to return to the same lunar node is ∼346.6 days, or about 18.6 days shorter than a sidereal year.

offer temporary shelter for water and other exospheric constituents such as Argon (Hodges Jr, 2018). The extent and distribution of SSRs will depend on the local topography and time of year: polar regions of topographic high such as the rim of Shackleton crater (89.6° S, 122.0° E) remain near-continuously exposed to sunlight (Gläser et al., 2018; Gläser et al., 2014; Speyerer & Robinson, 2013), however the regional expanse of SSRs should reach a maximum near the winter solstice when the solar elevation is reduced.

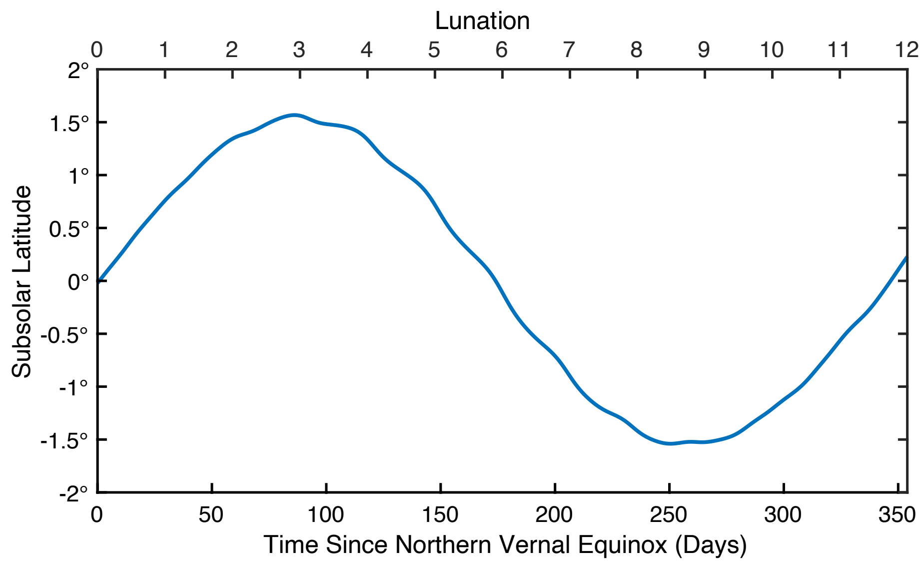

Figure 5.1: Subsolar latitude as a function of time for 12 lunations, or 1.02 draconic years.

In this chapter, an illumination model is developed using polar topographic data to assess the temporal variation and geographic extent of shadowed surfaces at the north and south pole of the Moon (pole-ward of ±80°). These data are used in conjunction with Monte Carlo simulations of water transport in order to explore the influence of seasonal shadow on surface migration as well as patterns in deposition within known PSRs in the modern era.

The text from this chapter is adapted from the publication Kloos et al. (2019). J.L.K. developed the illumination model, adapted the Monte Carlo model originally written by J.E.M. to examine seasonal trends, performed the analysis and drafted the manuscript. Collaborators on this work – J.E.M., J.S., T.G.N. and N.S. – assisted in developing the concepts and ideas for the project, and contributed to the analysis and editing of the manuscript.

5.2 Data and Models

5.2.1 Illumination Model

To identify the location of SSRs, as well as their variation in extent and distribution throughout the lunar year, an illumination model is developed that is similar to those previously described by Mazarico et al. (2011) and Gläser et al. (2014). Publicly available gridded digital elevation models (DEMs) from the LOLA instrument are used to model the sky visibility for individual surface elements (defined here as one pixel or a 240×240m surface region) pole-ward of 80°N and 80°S. The horizon method (Mazarico et al., 2011) is employed to ascertain the elevation of the local horizon for 360° of azimuth using a 1° step size. Horizon profiles are derived using vector geometry and account for the curvature of the Moon. Although computationally demanding, this step is only performed once and the horizon profiles are stored in a database.

Following the horizon mapping, the Sun is located from a lunar-fixed reference frame using the DE421 lunar ephemeris (Williams, Boggs, & Folkner, 2008). We begin our illumination survey at the northern vernal equinox on 29 July 2018 and carry it through 12 lunations[2] using a 1-hr time step, thereby encompassing 1.02 draconic years. At each time step and for each surface element, the subsolar point is cross-referenced with the local horizon profile to determine the visible fraction of the solar disk. In total, 12 maps are output for each hemisphere that record the geographic locations of PSRs and SSRs pole-ward of 80°N and 80° S during the lunation modeled; each map therefore typifies the dispersion of potential cold trapping area at a specific period of the lunar year. All SSRs have an associated "release time," which represents the lunation at which that point of the surface is no longer in shadow – so named because a water molecule trapped at that location would thereby be released.

5.2.2 Monte Carlo Model

Each Monte Carlo simulation begins with the production of individual H_2O molecules, hereby referred to as particles, onto the lunar surface. The generation of a particle initiates the simulation wherein the particle is tracked in space and time until becoming trapped within a PSR or lost to the system through photolysis or escape. Particles are given random initial positions based on a uniform probability distribution as has been implemented in other lunar exospheric models (e.g. Prem et al. (2018)). The

[2]One lunation is defined as the period of one lunar phase cycle (i.e. the time between one new Moon and the next). On average, it measures about 29.53 Earth days, although it may vary from month to month due to gravitational perturbations from the Sun.

randomized production scheme was not intended to model a particular source of water, however it was intended to remove any bias in north/south trapping as a result of the particle's origin latitude, as was shown to occur in previous works (Butler, 1997; Crider & Vondrak, 2000; Schorghofer, 2014). Furthermore, implementing a randomized production scheme enables study of the behavior of discrete populations of particles according to their provenance.

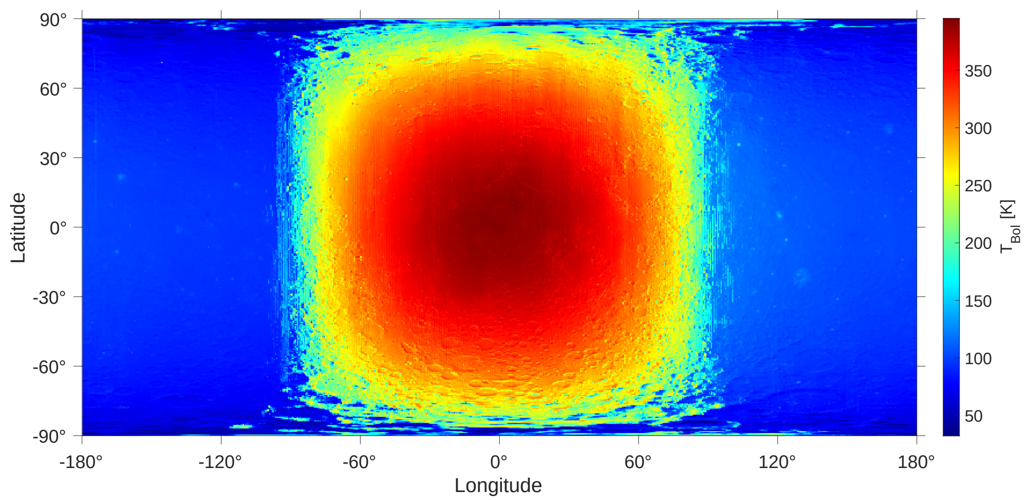

Figure 5.2: Diviner global temperature map, resolved at a spatial resolution of 0.5°/pixel. Data are taken from Williams et al. (2017).

Once a particle appears on the surface, it is assumed to instantaneously reach thermal equilibrium with the regolith below and take on the local surface temperature. Here, surface temperatures are determined using topographically-resolved bolometric temperature maps derived from the Diviner Lunar Radiometer instrument onboard LRO (Williams et al., 2017). Diviner temperature maps were created using nadir observations (emission angles $< 10°$) and are globally resolved at a spatial resolution of 0.5°/pixel. In total, Williams et al. (2017) produced 24 global temperature maps, each of which displays the bolometric brightness temperatures for a particular subsolar longitude using the binned values of all 7 of the Diviner IR spectral channels. These maps combine data across a nearly 6-year period between 5 July 2009 and 1 April 2015 and thus each temperature map represents an annual average of the 24 time steps through a lunation. An example of a Diviner global temperature map (at a subsolar point of 0°N and 0°E) is displayed in Figure 5.2.

The surface temperature controls the surface residence time τ, calculated using equation 2.1. The residence time is updated using a one hour time step (Δt = 1 hr) which is achieved by interpolating the Diviner temperature map. For particles where $\tau > \Delta$t, the model is advanced in time to the first point at which $\tau < \Delta$t and the particle is released. For a small fraction of Diviner temperature profiles (0.7%, all of which occur at the polar regions), the temperature remains low enough to effectively permanently trap water despite not being a PSR or SSR; particles that land in these regions are released at the morning terminator.

Particles emitted from the surface inherit a velocity vector in 3 dimensional cartesian coordinates where the particle's speed is drawn from the Maxwell-Boltzmann distribution and the vector direction is randomized over 2π steradians. Particle trajectories are simulated in three dimensions using a fourth-order Runge-Kutta scheme, where the lunar atmospheric density is assumed low enough so as to be non-collisional, and therefore particle flight paths are described by ballistic trajectories (Figure 5.3). Even the highest temperatures at the lunar surface do not permit a significant number of particles to achieve escape velocity; as such, the dominant way in which water can be lost to the system is through photodissociation from solar UV photons. Following Moores (2016), the probability of photodissociation is estimated using a rate of 1.26×10^{-5} molecules s^{-1}, appropriate for normal sun activity (Crovisier, 1989). This method ensures that particles with longer flight times are more likely to dissociate while still retaining the random nature of this process.

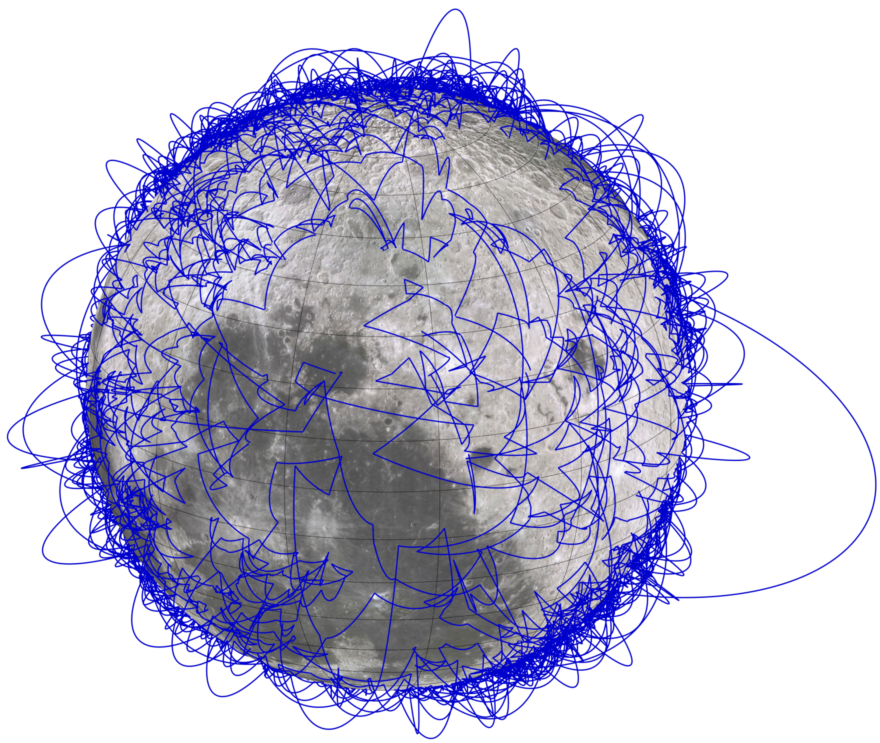

Figure 5.3: Sample Monte Carlo run showing the ballistic trajectories of an H_2O molecule with 5,000 jumps. Trajectories are shown to scale relative to the Moon. Lines of latitude are shown every 10°, lines of longitude every 30°.

In total, 12 Monte Carlo simulations were performed, where each simulation was conducted using 2 million particles and was intended to model spatial trends in the polar deposition of water at a particular period of the lunar year. Each Monte Carlo run was executed with PSR and SSR maps (described in section 5.2.1) emplaced at the north and south pole that record the trapping area out to ±80° latitude at the temporal period being analyzed. To model the delivery of water to low-latitude PSRs and to understand their influence on the pole-ward migration of water, we additionally place the altimetrically-derived PSR maps produced by Mazarico et al. (2011) at the poles, which chart the location of PSRs out to ±65° latitude at 240 meters-per-pixel resolution. When a particle lands within a PSR, the simulation is ended and particle's location and flight time are recorded. For particles landing in an SSR, the model is advanced to the first lunation at which the surface is directly illuminated by the Sun (i.e. the release time); new SSR maps are uploaded and the particle is liberated and continues its journey until either photodissociating, escaping or becoming PSR-trapped.

5.3 Results

5.3.1 Spatial and Temporal Extent of Polar Shadow

Figure 5.4 displays the locations of SSRs pole-ward of 80° N and S, where the color denotes the length of time, in Earth days and over a time span of 12 lunations, that the surface spends in shadow. Surface elements that lie in shadow across all 12 lunations (PSRs) are shown in white. As shown here, SSRs tend to emanate from permanently shadowed regions and expand toward the pole. Regions near the perimeter of PSRs are the longest seasonally shadowed surfaces; with increasing distance from PSR boundaries, SSRs become progressively diminished in temporal extent.

Cumulatively, the north and south permanently shadowed area determined from this work is 15,772 km^2 and 18,909 km^2, respectively, which is 23% and 18% larger than previous estimates from Mazarico et al. (2011) whose modeling technique was similar to ours. At least 2 explanations can be invoked to explain the disparity in PSR size. First, the temporal domain of our survey was shorter than that of Mazarico et al. (2011), whose analysis was performed across multiple lunar precessional cycles (18.6 years). Second, our estimate includes PSRs down to a single pixel, while Mazarico et al. (2011) removes PSRs fewer than 9 contiguous pixels due to uncertainties in the modeling. When the same treatment is performed on our data, our PSR estimates are larger by 13% and 14% for the north and south, respectively, with good geographic alignment. Using a ray tracing method and including single-pixel PSRs, McGovern et al. (2013) obtained PSR estimates of 12,090 km^2 and 16,800 km^2 pole-ward of 80° for the north and south; these authors, however, argued that their smoothing operation of the DEM may have resulted in underestimations of PSRs. In the Monte Carlo simulations described below we include all PSRs down to a single pixel while acknowledging the same uncertainties considered by Mazarico et al. (2011). This decision was made in order to provide an upper limit on PSR accretion as well as to account for the influence of smaller-scale PSRs on volatile transport.

Throughout the lunar year, the shadowed area varies significantly (Figure 5.4c).

At its largest expanse near the solstices (green vertical bars), the total SSR area (solid lines) more than doubles the PSR area (dashed lines) in both hemispheres, totalling 43,160 km^2 and 41,640 km^2 for the north and south, respectively. As expected, the majority of this area is concentrated at high latitudes (Figure 5.4d). Pole-ward of 87° lie the densest trapping regions, reaching a peak density near 89° in the north and 88.5° in the south at which point 85% and 72% of the area lie in shadow, respectively. Based on Diviner surface temperature measurements, Williams et al. (2019) have determined a variation in cold trap area of more than a factor of two between summer and winter. These authors define cold traps by T_{max}<110 K, and the sizes depend on the choice of this threshold.

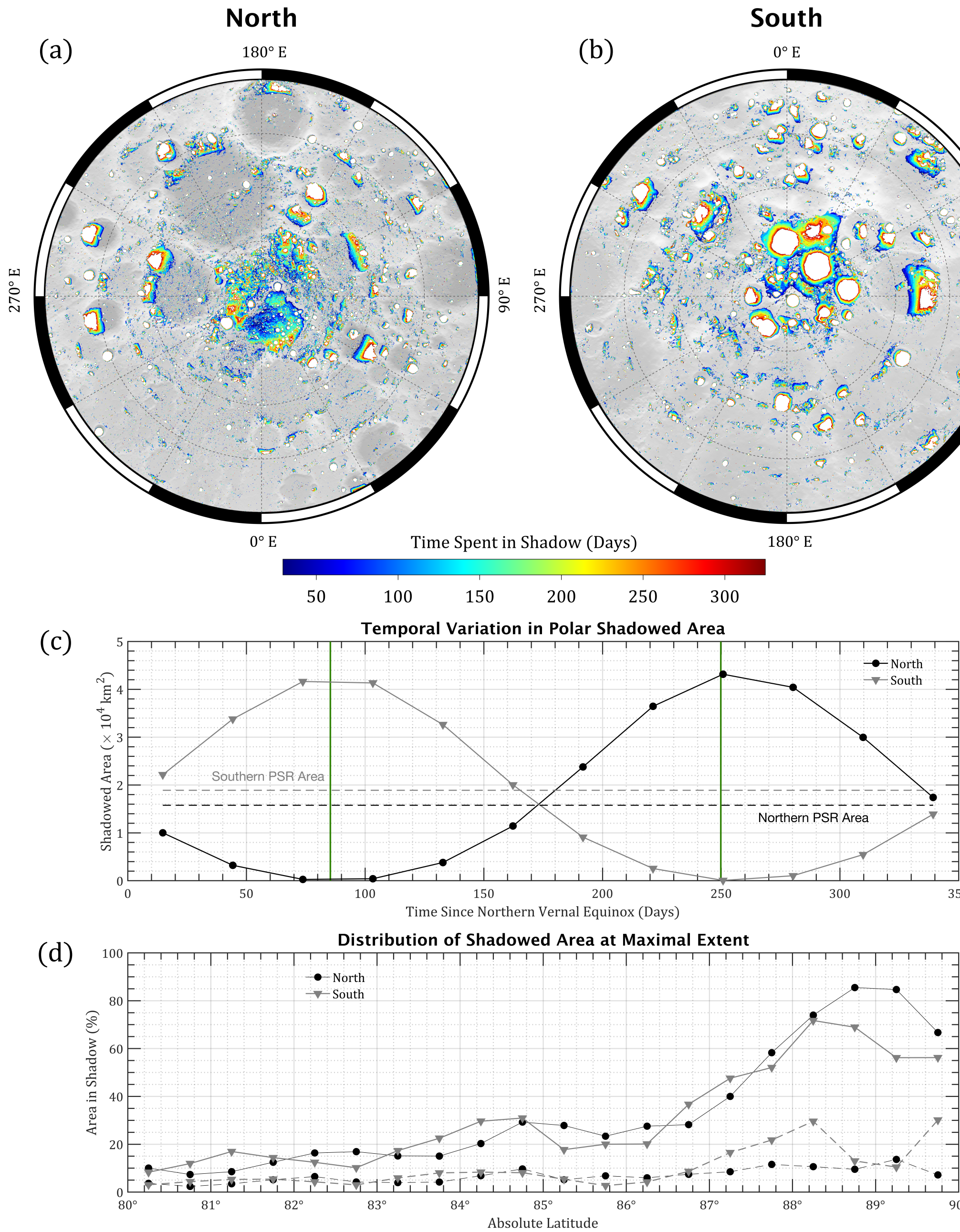

Figure 5.4: Locations of SSRs pole-ward of ±80° within the northern (a) and southern (b) hemisphere. Color denotes the number of Earth days spent in shadow over the course of 12 lunations (354 days) while PSRs are shown in white. Lines of latitude are shown every 2.5°. (c) Variation in shadowed area throughout the year. Solid lines represent SSR area while dashed lines show PSR area measured in this work. Green vertical bars show the summer/winter solstices. (d) Geographic distribution of total shadowed area (PSRs + SSRs; solid lines) and PSRs (dashed lines) at its maximal extent. Data are binned using a 0.5° latitude bin spacing.

5.3.2 Geotemporal Trends in PSR Water Deposition

Figure 5.5 shows the resulting spatial and temporal trends in water accretion within northern (panel a) and southern (panel b) hemisphere PSRs. Here, the color axis corresponds to the PSR particle concentration, σ_p, which is given by the PSR particle count per unit permanently shadowed area (km^2) within a 0.5° latitude bin; data are normalized by the production rate, γ, which is defined as the quotient of the total number of particles simulated per lunation and the surface area of the Moon. In the following discussion, we restrict the start location of particles to latitudes equatorward of ±65° to avoid bias in the latitudinal trends of PSR water capture.

Variance in PSR water delivery is observed throughout the year, manifesting most strongly near the pole owing to the growth and decay of seasonal shadow. Near the equinox (time = 0–29.5 days), southern hemisphere PSRs exhibit a flat latitudinal distribution, whose mean concentration σ_p is ∼102 times larger than the production rate γ. As time progresses and the trapping area broadens in the south, water en route to the pole is more likely to become trapped, resulting in a build up of water within seasonally shadowed terrain and an associated reduction in water reaching high-latitude PSRs. When trapping area is at its largest expanse in the south (time = 59–118 days), 8.5% of particles simulated were seasonally trapped – a 49% increase from the amount seasonally trapped near the equinox (time = 0–29.5 days). Examining the region pole-ward of 80° S for which seasonal trapping area is modeled, σ_p decreases steadily moving toward the pole between time = 59–118 days, reaching a

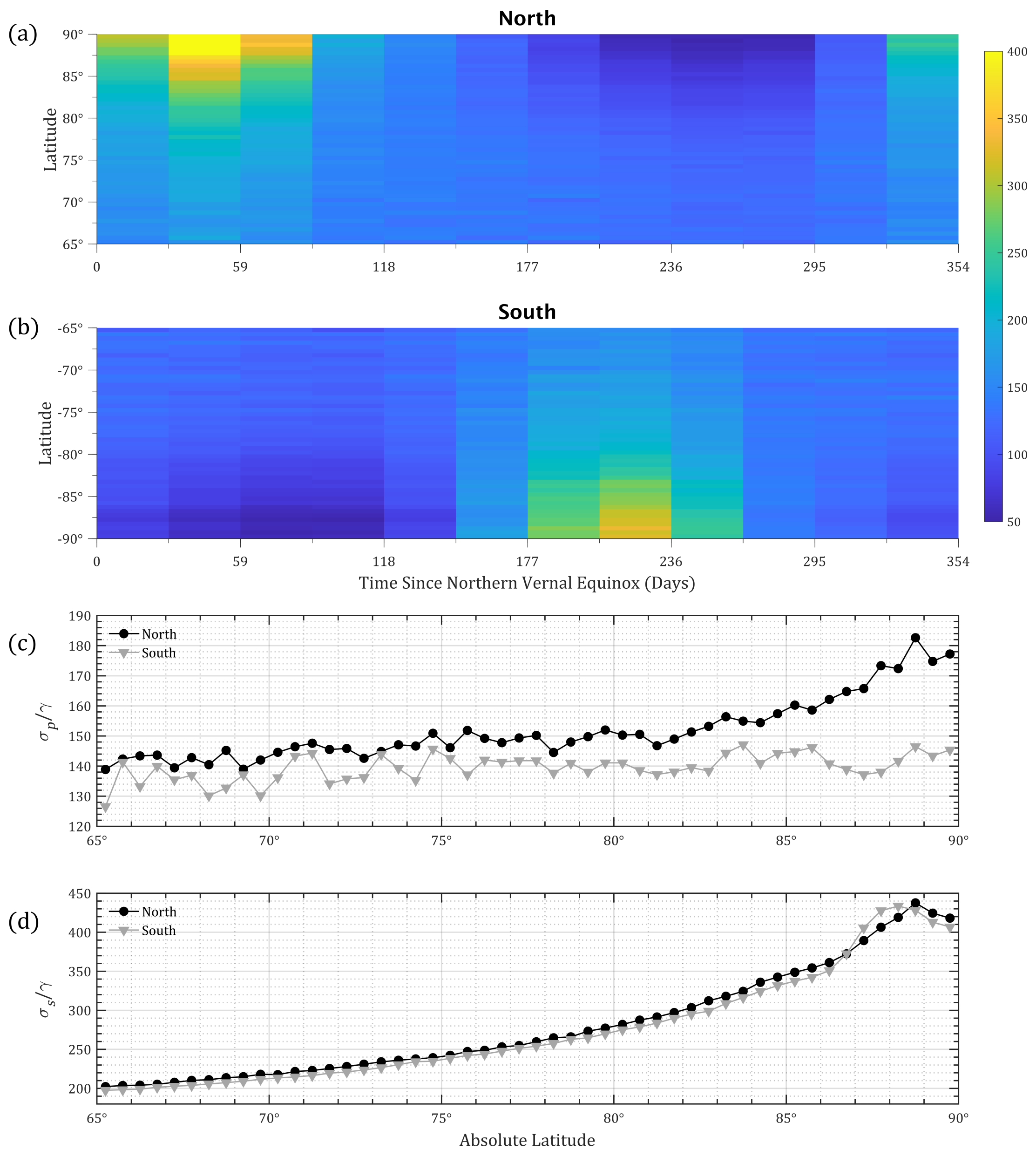

Figure 5.5: Geotemporal variations in volatile cold-trapping within northern (a) and southern (b) hemisphere PSRs spanning 12 lunar days. The color axis corresponds to the PSR particle concentration σ_p normalized by the production rate γ. (c) Accumulated latitudinal distribution of PSR water after one lunar year. (d) Latitudinal dependence of the infall rate. σ_s is given by the particle count divided by the area within each 0.5° latitude band.

minimum of 47γ.

While the high-latitude PSRs accrete less water during the winter months, the surrounding SSRs are temporarily enriched in adsorbed water. Assuming a steady supply, water gradually builds up within seasonally shadowed terrain, where the quantity of water accumulated is proportional to the length of time spent in shadow; SSRs at the periphery of PSRs thereby have the highest seasonal concentrations given their prolonged collection span. As SSRs deteriorate and the sunlight returns to the surface, seasonally trapped particles are eventually released into the exosphere and continue their migration. The reduced polar temperatures produce relatively short hop distances (on the order of 100–150 km pole-ward of $\pm80°$ compared to $\sim$200 km at the equator), which has two implications for liberated water: (1) the short flight time decreases the probability of loss per hop, as only $\sim$42% of all seasonally trapped particles were eventually photolyzed or escaped (compared to the 75% of non-seasonally trapped particles that were lost or destroyed); and (2) the decreased hop distance serves to increase the amount of time and the number of jumps that a particle will make at the pole. Given that this is the highest density region of PSRs at both poles (see Figure 5.4), the majority of liberated water quickly become trapped within a high-latitude PSR, while a minority migrate equator-ward and become captured by a lower-latitude PSR. As shown in Figure 5.5, water is liberated sequentially as the seasonal trapping area contracts; in the south, this can be observed as a gradual increase in σ_p between time = 118–236 days after the equinox, reaching a peak near the summer solstice ($\sigma_p = 301\gamma$ at time = 206.5-236 days) when the majority of seasonally trapped water is extricated.

The overall temporal trend in PSR accretion is the same in the north as it is in the south, however there are notable differences in magnitude. Northern hemisphere PSRs, particularly those nearest the pole, accumulate more water per unit area than those in the south. Despite less permanently shadowed area, a similar percentage of the total number of particles simulated were captured in the north as in the south. In total, northern and southern hemisphere PSRs collected 10.7% and 11.0% of the particles simulated, respectively – consistent with previous exospheric models (Moores, 2016; Schorghofer, 2014; Schorghofer, Lucey, & Williams, 2017). The greatest PSR influx in the north occurs shortly after the vernal equinox (time = 29.5–59 days), where $\sigma_p = 404\gamma$ – about 34% larger than the peak observed in the south. The north/south asymmetry will be discussed in more detail in section 5.4.1.

5.4 Discussion

5.4.1 Implications for North and South Polar Frost Distribution

When PSR water deposition is totaled across the lunar year, clear latitudinal trends are observed (Figure 5.5c). In both hemispheres, the PSR water concentration σ_p increases moving from $\pm 65^{\circ}$ toward the pole, however, as discussed below, the latitudinal trends in deposition are markedly different in the north and south. The increased polar concentrations indicate that lower-latitude traps, given their relatively low fractional coverage, do not pose significant barriers to the pole-ward migration of water. As such, the ability of water to reach high-latitudes where flight paths are diminished enable PSRs nearest the pole to efficiently capture water.

The broad-scale trends in delivery and accretion shown in Figure 5.5c are qualitatively consistent with latitudinal trends in surface ice concentration detected from orbit (Fisher et al., 2017; Hayne et al., 2015; Li & Milliken, 2017) as well as hydrogen abundance (and perhaps water ice abundance) within the upper 1–2 meters of the surface as seen from neutron data (Feldman et al., 2000; Mitrofanov et al., 2010). With the exception of two south polar craters and one north polar crater, however, hydrogen enhancements are not coincident with areas of permanent shadow where the surface water ice is confined (Sanin et al., 2012). While the extent and distribution of cold traps would be different for a palaeopole than for the modern era, the depositional trends shown in Figure 5.5c support the notion that volatiles may preferentially be delivered to, and accumulate within, cold traps near the rotational poles.

The PSR depositional patterns can be better understood by examining the latitudinal dependence of the infall rate of water at the surface without PSRs present. This is shown in figure 5.5d, where σ_s is obtained by counting the number of particles that fall within a 0.5° latitude band, which is then divided by the latitudinal area;

as before, data are normalized by the global production rate γ. As shown here, σ_s varies by a factor of $\sim$2.25 from 65° to the pole, reaching a maximum of $\sim 450\gamma$ at 88–89° N and S. The increased flux of water at high latitudes is a result of its temperature dependent migration pattern; the diminished surface temperatures at high polar latitudes yield shorter and more numerous hops, resulting in a higher infall rate. The inclusion of sub-pixel temperature variations introduced by unresolved topography may preferentially reduce the infall rate at lower latitudes (65°–70°), as Prem et al. (2018) found higher rates of escape at low latitudes when transport was modeled with a rough surface compared to a smooth surface. These authors also found that, in comparison to a smooth surface, introducing a stochastic rough surface temperature model slightly increased the number of molecules that were cold-trapped and correspondingly decreased the number of molecules that were photolyzed. Thus, with surface roughness effects accounted for in our model, the percentage of molecules cold-trapped is expected to be larger than the 10.7% and 11.0% figures reported in section 5.3.2.

At all latitudes, northern hemisphere PSRs accumulate more water per unit area than those in the south, however the north/south difference becomes especially prominent nearest the pole; analyzing the region pole-ward of 85°, the mean PSR water concentration σ_p is $\sim$19% larger in the north than in the south. To understand the cause of this disparity, we examined the influence of SSRs on north/south PSR accretion by performing an additional Monte Carlo simulation without SSRs present (using 2 million particles and identical model parameters as before). The results of this simulation, however, revealed no statistically significant difference in the total number of particles trapped in either hemisphere without SSRs present. As well, the north and south broad-scale latitudinal trends in PSR accretion without SSRs were unchanged from those with SSRs. This is more likely due to a bias, however, than a true result. Without the inclusion of seasonal polar temperatures in our model, our model releases seasonally trapped particles at annual average temperatures that are not reflective of the true values at the release times. Thus, the current version of this model is not properly equipped to study this problem, however the following chapter will explore this issue in greater detail.

What is the cause, then, of the north/south asymmetry if not SSRs? The asymmetry can be explained by a combination of two factors: (1) the high efficiency of PSR capture of water at high latitudes and (2) hemispheric disparities in the PSR size-frequency distributions. As previously described, water molecules migrating at high latitudes have a high probability of becoming cold-trapped due to a confluence of the diminished temperatures producing shorter and more numerous jumps and relatively dense trapping area. This process is so effective that, despite there being less PSR area in the north, water molecules are captured with roughly equal efficiency in both hemispheres, resulting in larger concentrations in the northern hemisphere after the area is accounted for.

5.4.2 Implications for Polar Frost Variability

Numerous orbital datasets have provided evidence for a diurnally varying surface concentration of H_2O/OH, implying that H_2O/OH is produced at the surface via solar wind implantation and subsequent oxygenation, and, furthermore, undergoes a temperature dependent migration over the course of a lunar day (Clark, 2009; Hendrix et al., 2019; Hendrix et al., 2012; Li & Milliken, 2017; Pieters et al., 2009; Sunshine et al., 2009). If a continual source of mobile water is assumed, the expansion and contraction of seasonal shadow at the poles should give way to a seasonal variation in the surface hydration in addition to a diurnal one. While the magnitude of the seasonal variation would be largest at the polar regions where SSRs are concentrated, variation should also be present to a lesser degree at low latitudes as seasonal water released from the pole migrates toward the equator. The seasonal variation in exospheric Argon observed by the Lunar Atmosphere and Dust Environment Explorer (LADEE) spacecraft was attributed to the presence of seasonal cold traps, in which maxima and minima occur at the solstices and equinoxes, respectively (Hodges Jr, 2018).

In Figure 5.6a we present a model of how the polar concentration of water varies throughout the year assuming a continual source of constant magnitude. Here, σ_s represents the surface concentration that is given by the bulk particle density poleward of $\pm 80°$. As shown here, σ_s varies throughout the year, where the peak occurs at time = 340 days and 162 days for the north and south, respectively – significantly

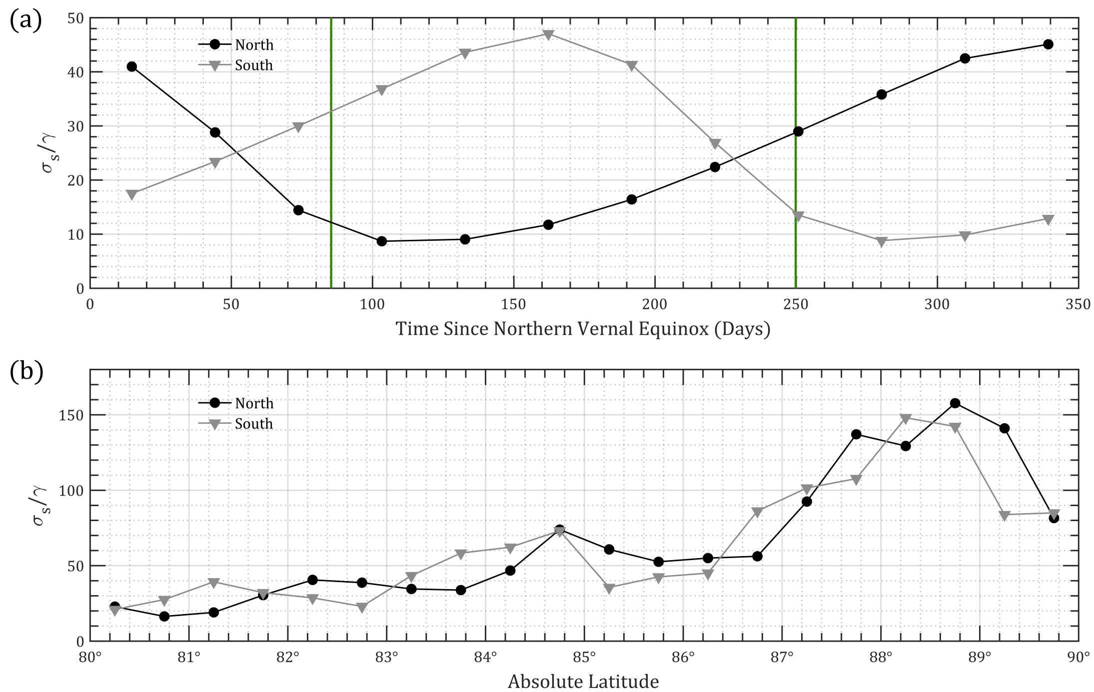

Figure 5.6: (a) Seasonal variation in the bulk surface concentration σ_s pole-ward of $\pm 80°$ assuming a steady supply of water. Data are normalized by the production rate γ. Green vertical lines represent the summer/winter solstices. (b) Geographic distribution in water for the north and south pole at their respective peak abundances. Data include water captured within SSRs and PSRs.

offset from the solstices where the seasonal trapping area is greatest – due to the retention of seasonal water. The peaks represent a turning point where the loss rate, regulated by the release of seasonally captured water, begins to outpace the rate of water deposition. The overall temporal variation is identical in the north and south, where the maximum concentration reached is $\sim 45\gamma$ in both hemispheres. Figure 5.6b displays the latitudinal distribution when the polar concentration of water is largest; as can be seen here, a rapid increase in σ_s occurs at 87° in both hemispheres where the seasonal trapping area is densest.

6 The Exospheric Transport of Cometary Volatiles on the Moon

6.1 Chapter Overview

Although water has received most of the attention in current theoretical and observational studies, it is not the only volatile expected to exist on the Moon. In addition to water, the LCROSS impact experiment identified a range of volatile compounds abundant in comets and micrometeorites (Bockelée-Morvan & Biver, 2017; Colaprete et al., 2010), including CO_2, CO, NH_3, SO_2, H_2S and CH_4. The Apollo missions detected CO, CO_2, NH_3 and CH_4 in the lunar exosphere (Hoffman & Hodges, 1975; Stern, 1999), and these same species were later observed by the LADEE mission (Benna, Mahaffy, & Hodges, 2014; Hodges Jr, 2016). LRO-LAMP has identified signatures of CO_2 within a few of the coldest south polar craters (Hayne et al., 2019), although beyond these few limited studies there is little information about the abundance and near-surface distribution of non-H_2O volatiles on the Moon.

The fact that these volatiles are sourced to the Moon, however, is unambiguous. The moon is continually bombarded by meteoroids and interplanetary/interstellar dust grains containing a large range of volatile materials (Gibson Jr, 1992), including those noted above. Upon striking the surface, vaporized material is injected into the exosphere and transported about the surface, potentially accumulating within cold traps if temperatures are suitably low. Alternative sources for LCROSS volatiles are solar wind (Hodges Jr, 1976). The estimated carbon influx to the Moon is 1.6×10^5 cm^{-2} s^{-1}, and Hodges Jr (1976) noted that the gardening rate is not significant enough to assimilate the carbon into the regolith. Even if meteoroids are not sources of volatiles in and of themselves, they may release solar-wind generated species during impact, similar to what was proposed to occur for H_2O (Benna et al., 2019). The efficiency with which subsequent vapor transport occurs is not well known, although positive exospheric detection of some species suggests that it is a non-zero fraction.

In this chapter, we explore the thermal ballistic migration of the aforementioned volatile compounds (see also Table 6.1) in a collisionless setting. Our goal is to quantify the efficiency with which these volatiles are delivered to the polar regions, as well as the infall rates within PSR craters.

6.2 Updates to the Monte Carlo Model

To explore the diffusive lateral migration of volatiles on the Moon, the Monte Carlo model described in Chapter 5 is employed with several noteworthy adaptations. A significant update to the model is the manner in which data is output. While the previous model output only key elements of the simulation outcome, such as the fate of the molecule, start and end locations, migration time and number of jumps, the updated version returns statistics in increments of 48 hours, allowing the time evolution of surface densities to be examined. Simulation outputs include global surface particle densities, which are segmented into polar (poleward of ±80°) and non-polar (equatorward of ±80°) regions. Non-polar binning is performed at 4° and 1° for latitudes and longitudes, respectively, while polar binning is performed at 0.5° and 1°.

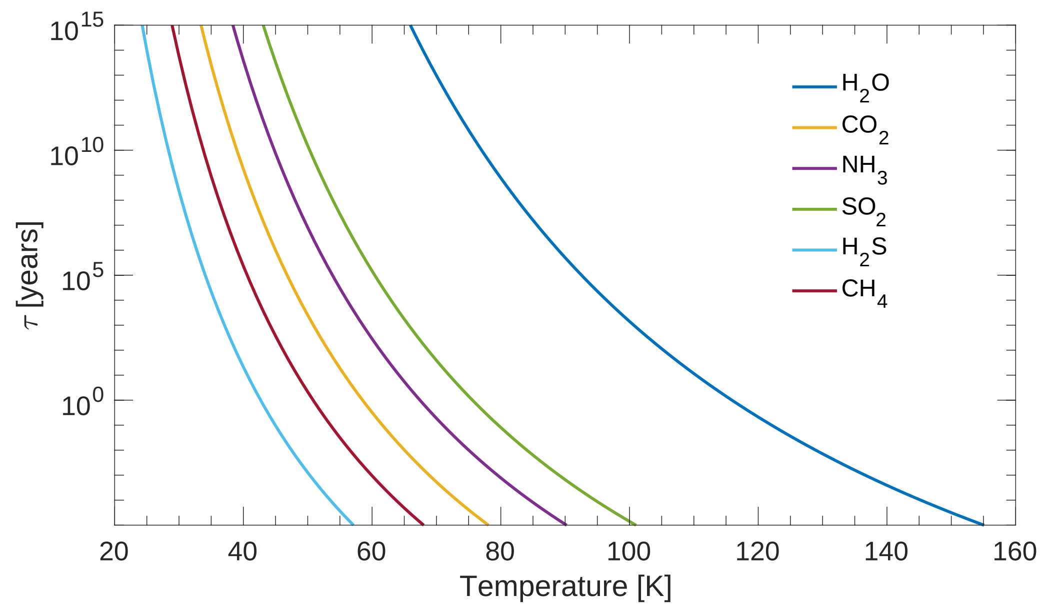

Figure 6.1: Adsorption residence time (years) plotted as a function of temperature.

The residence time for adsorbed species is computed using activation energies for single component ices, derived by Sandford and Allamandola (1993) and tabulated in Table 6.1. Figure 6.1 provides a visual comparison of the adsorption residence

Table 6.1: Physical constants for the volatiles examined in this study.

Species	[a]E_a [eV]	Q [J mol^{-1}]	T_t [K]	P_t [kg m^{-1} s^{-2}]	μ [g mol^{-1}]	ρ [kg m^{-3}]	[b]τ_{photo} [Hours]	T_v [K]
H_2O	0.46	51060	273.2	612	18.0	920	22.1	101
NH_3	0.27	31200	195.4	6090	17.0	817	1.54	63
SO_2	0.30	24900	197.6	1670	64.1	1920	1.32	55
H_2S	0.17	22500	187.6	22900	34.1	1360	0.87	48
CH_4	0.20	9700	90.7	11696	16.0	900	25.2	30
CO	0.08	7600	68.1	15300	28.0	1700	3.86	30
CO_2	0.23	27200	216.6	518500	44.0	1500	139	54

[a]Activation energies for all species with the exception of CH_4 are derived for single-component ices by Sandford and Allamandola (1993). The activation energy of CH_4 was given by Hodges Jr (2016).

[b]Values of τ_{photo} come from Huebner, Keady, and Lyon (1992), with the exception of H_2O which is derived by Crovisier (1989). All values are for normal Sun activity.

time (computed using equation 2.1) as a function of temperature for the compounds considered in this study. The photolysis rate of each molecular gas is taken from Huebner, Keady, and Lyon (1992), derived for normal Sun activity at a mean-Sun distance of 1 AU.

A second modification is the implementation of cold trap capture. In the prior model described in Chapter 5, it is assumed that PSRs act as cold traps for H_2O; this, however, is a dubious assumption given the relatively warm surfaces (T_{max}>150 K) of some – particularly low-latitude – PSRs. While residence times within low latitude PSRs may be enhanced relative to normal sunlit areas, it is unlikely that ice may accumulate there over long timescales. Moreover, due to differences in their vapor pressures, the species listed in Table 6.1 are thermodynamically stable at different temperatures (e.g. Zhang and Paige, 2009). Thus, to incorporate more realistic thermal trapping, we implement cold trap capture using the classically defined volatility temperatures T_v, or the temperature at which a 1 mm thick ice deposit would evaporate in 1 Gyr. This temperature is meant to reflect stable conditions for each species, such that long term preservation is possible. T_v can be found by computing the rate of sublimation into vacuum, $\dot{E}_{sub}$ (kg m^{-2} s^{-1}), as a function of ice temperature, T, using the well-known relationship:

$$\dot{E}_{sub} = P_v(T)\sqrt{\mu/2\pi RT}, \tag{6.1}$$

where μ is the molar mass, R is the universal gas constant and P_v is the saturation vapor pressure, given by:

$$P_v = p_t \exp\left[\frac{-Q}{R}\left(\frac{1}{T} - \frac{1}{T_t}\right)\right]. \tag{6.2}$$

Here, p_t, T_t and Q are the triple point pressure, triple point temperature and the sublimation enthalpy, respectively, which vary for each compound (see Table 6.1). t_{sub}, the length of time needed to sublimate an ice layer of a given thickness Δz, can then be found using the density of the ice, ρ:

$$t_{sub} = \frac{\rho}{E_{sub}}\Delta z \tag{6.3}$$

Figure 6.2 displays the calculated volatility temperatures along with the maximum PSR temperature distributions at each pole (Williams et al., 2019). It is noteworthy that the north and the south exhibit markedly different temperature distributions owing to differences in topographic relief and crater size-frequency distributions, with

Table 6.2: Cold trap area at the north and south pole based on volatility temperatures.

Species	Trap Area (N) [km^2]	Trap Area (S) [km^2]
H_2O	3484	9531
NH_3	52	309
SO_2	2.6	21.4
H_2S	0	1
CH_4	0	0
CO	0	0
CO_2	2	16

the south polar PSRs being on average much colder. This in turn leads to significant hemispheric asymmetries in the cold trap area, although for many non-H_2O species there is very little or no stable area set by the stability threshold T_v (Table 6.2). Methane, carbon monoxide and hydrogen sulfide, for example, have virtually no stable area at either pole, meaning that LCROSS likely observed adsorbed molecules within Cabeus crater as opposed to crystalline ices. Meanwhile CO_2 has a meager 2 and 16 km^2 of cold-trapping area at the north and south pole, respectively. Ammonia and sulfur dioxide have marginally higher trapping areas, although the calculated values still occupy only a tiny fraction of the lunar surface. Given the relatively coarse scale of the temperature data used here (240 m $pixel^{-1}$), these cold trap estimates are likely to be lower bounds as sub-pixel topography and secondary shadowing from indirect sunlight within PSRs should enhance the trapping area at scales below the available data (Hayne, Aharonson, & Schörghofer, 2020). The small fractional cold trap area of CO_2, NH_3 and SO_2 would suggest that these areas may be highly concentrated.

Yet another revision to the model is the incorporation of newly generated seasonal polar temperatures from the Diviner instrument (Williams et al., 2019). Although the

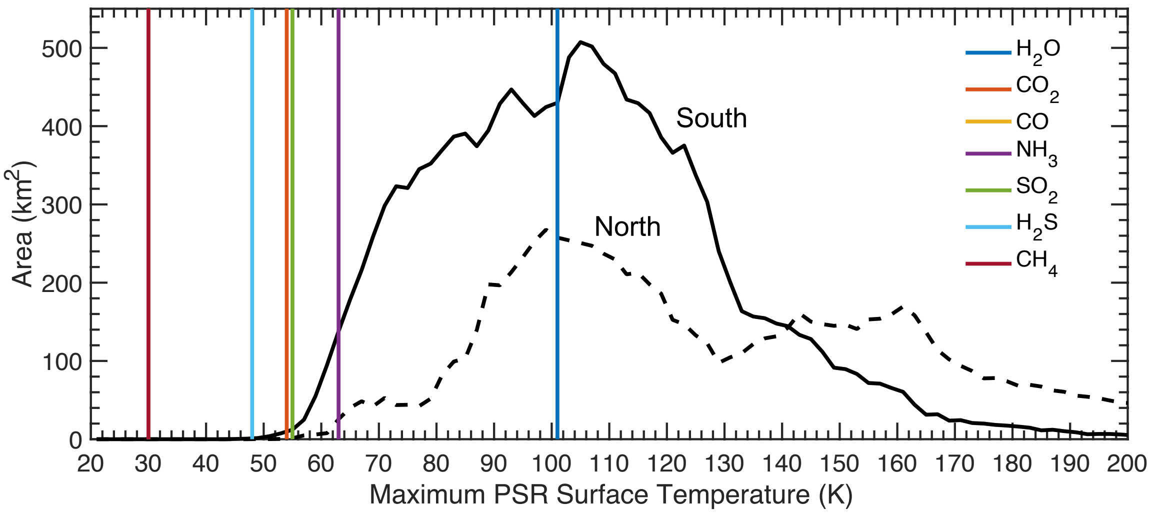

Figure 6.2: Histograms of maximum temperatures for PSRs at the lunar north and south pole. Vertical bars mark the volatility temperature for various ices detected within the LCROSS impact plume. PSR temperature data are derived from Diviner thermal-IR measurements (Williams et al., 2019).

previous model incorporated seasonality through shadowing, the inclusion of seasonal temperatures allows a temperature-based, and therefore more realistic, approach to examining the phenomenon of seasonal condensation. Diviner polar data are split into winter and summer seasons, which are defined to be the temporal period when the subsolar point is, respectively, above or below the equator for each pole. In total, 24 maps (240 m pix^{-1}) exist for each hemisphere and for each season. Each map represents the seasonal average temperature at a given subsolar longitude (thus 24 time steps through a lunation in each season). As before, temperature profiles are interpolated using a 1-hr time step.

Finally, a smaller change that bears mentioning is the velocity distribution: in place of a Maxwell-Boltzmann distribution, we adopt the use of an Armand distribution as recommended by Hodges Jr and Mahaffy (2016). While this change will not significantly influence the model results, Hodges Jr and Mahaffy (2016) found better agreement in the Argon vertical density profiles using this distribution, and others have argued that an Armand distribution is appropriate for surface-bound exospheres (Smith et al., 1978). As noted by Schorghofer (2018), the Armand distribution includes an extra factor in front of v_z in order to account for the non-uniform emission produced by roughness effects, thus making it appropriate for exospheres interfaced with a rough surface. Figure 6.3 plots the Armand velocity distribution for $T = 200$ K for the gasses examined in this study. Differences in the probability density functions are related to differences in the molecular weights of different molecules (table 6.1), where the distribution becomes more narrow and shifts toward lower temperatures with increasing molecular weight.

Simulations begin at the northern vernal equinox and are carried out over two lunar years, allowing one year for the model to equilibrate. For each species, models were executed with and without the inclusion of seasonal polar temperatures to gauge their prospective influence on trapping and destruction efficiencies. In both implementations, particles are assigned random initial positions on the surface, and here we assume a continuous source distribution, with 5,000 computational particles added to the surface at each time step ($\sim$1.8 million particles in total). This results in a modeled source rate of $\gamma = 7.6 \times 10^{-16}$ particles m^{-2} s^{-1}. Particles remaining on the surface at the end of the simulation are allowed to finish their migration until they are cold-trapped or destroyed; however only the fate, migration time and

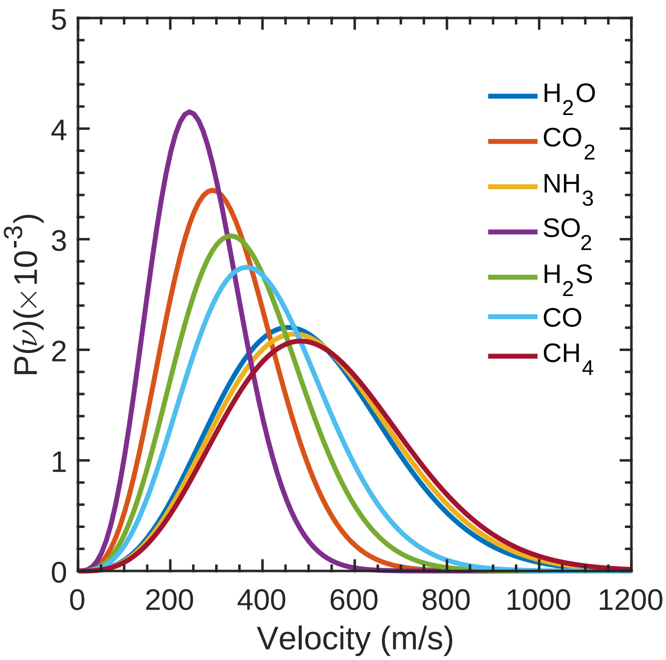

Figure 6.3: Armand velocity distribution computed at T = 200 K for different volatile species.

end location are stored for these particles (not the intermediary statistics). This allows statistical comparisons between simulations with and without the inclusion of seasonal temperatures to be accurately made.

6.3 Results and Discussion

6.3.1 The Influence of Seasonal Temperatures on Volatile Migration

Table 6.3 gives comparative trapping and photolysis statistics for simulations with and without seasonal cold traps. Examination of this table shows that in both cases, the vast majority ($> 99\%$) of all non-H_2O gasses are photolyzed, and thus cold trapped in very small quantities. In each case, the number of molecules that escape is negligible, but is shown for completeness. As a result of its significantly larger trapping area, H_2O has the highest trapping fraction, with $\sim 3\%$ and $\sim 6\%$ captured in the north and south, respectively. This is reduced from the values reported in Chapter 5 due to the more stringent trapping threshold employed here, as it means that molecules must make more hops prior to being sequestered. Due to its relatively long photolytic lifetime (139 hours), CO_2 has the second largest trapping fraction, with $\sim$0.03% captured in the north and $\sim$0.3% captured in the south. Note that this is substantially less than the CO_2 trapping fractions of 13% reported by Butler (1997) or the 35% reported by Schorghofer et al. (2017), whose CO_2 trapping area was significantly larger than ours. The remaining species in Table 6.1 have shorter lifetimes in the exosphere and are trapped in even smaller quantities due to a combination of low stable area and high photolysis rates.

A convenient way to express the effectiveness with which a particular gas is trapped is the "trapping efficiency" (Schorghofer et al., 2017), defined as the ratio of the fraction of molecules trapped to the fractional cold trap area. Table 6.3 shows that these efficiencies vary significantly between different species, primarily as a result of differences in their photolytic lifetimes. CO_2 makes many jumps prior to photolysis and thus has a disproportionately greater probability of landing within a cold trap. On this basis, CO_2 cold traps, which are cold to enough to also preserve H_2O,

Table 6.3: Trapping statistics with and without the inclusion of seasonal polar temperatures. CH_4 and CO have been omitted as they are unable to be cold-trapped in the classical sense.

Species		**Trapped in North** (%)	**Trapped in South** (%)	[a]**Photolyzed** (%)	**Escaped** (%)	[b]**Trapping Efficiency**
H_2O	w/ SSRs	3.18	6.28	90.5	5.00×10^{-5}	276
	w/o SSRs	3.05	5.92	91.0	5.00×10^{-5}	262
NH_3	w/ SSRs	3.45×10^{-3}	2.39×10^{-2}	99.9	0	29
	w/o SSRs	3.35×10^{-3}	1.98×10^{-2}	99.9	5.00×10^{-5}	24
SO_2	w/ SSRs	3.00×10^{-4}	5.55×10^{-3}	99.9	0	92
	w/o SSRs	3.50×10^{-4}	3.40×10^{-3}	99.9	0	59
H_2S	w/ SSRs	0	1.00×10^{-4}	99.9	0	39
	w/o SSRs	0	5.00×10^{-5}	99.9	0	19
CO_2	w/ SSRs	0.03	0.33	99.6	0	7622
	w/o SSRs	0.03	0.27	99.7	0	6400

[a]Photodissociation rates are derived by Huebner, Keady, and Lyon (1992) and assume normal Sun activity.

[b]Trapping efficiency is defined by Schorghofer et al. (2017) as the ratio of the fraction of molecules trapped to the fractional cold trap area. This can also be thought of as the average particle concentration of a cold trap normalized by the source rate.

SO_2 and NH_3 over long timescales, should be highly concentrated. H_2S, NH_3, and SO_2, in contrast, have relatively lower efficiencies and make fewer hops prior to being being broken apart. The fact that these three species have such a low trapping efficiency is curious given that they were the second, third and fourth most abundant volatiles detected by LCROSS, respectively. In addition, as Colaprete et al. (2010) points out, sulfur-bearing compounds such as H_2S and SO_2 typically comprise <1% of the H_2O mass fraction of a cometary nucleus, while CO_2/H_2O can be as large as 20–30% (Bockelée-Morvan & Biver, 2017) but was observed in lower quantities by LCROSS. Colaprete et al. (2010) proposes that molecular formation on cold-grain surfaces within a PSR may alter the chemistry over time, such that the ice distribution is no longer compositionally representative of a single source.

We find that simulations executed with seasonal polar temperatures resulted in a higher trapping efficiency and capture rate than those without. This enhancement was observed for all species[1], although the difference is small: for H_2O, the inclusion of seasonal temperature data resulted in a 0.13 and 0.36 percentage point increase for the north and south, respectively; for CO_2 the increase was only 0.06 percentage points in the south and 0 in the north. These differences are driven by the relatively colder temperatures within the seasonal data, as molecules launched from colder surfaces tend to make shorter hops and spend less time in the exosphere exposed to high energy UV radiation (decreasing the probability of photolysis). Seasonal traps

[1] Due to the low trapping fractions of NH_3, SO_2 and H_2S, disparities between seasonal and non-seasonal data should be interpreted with caution.

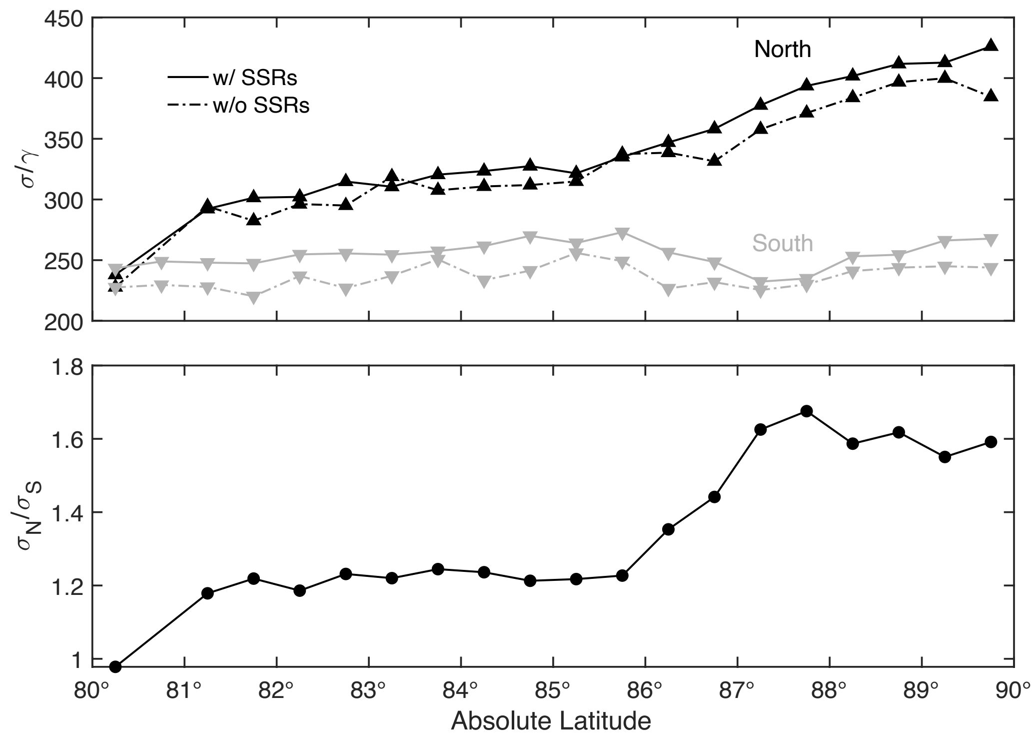

Figure 6.4: Top: Concentration of cold trapped H_2O as a function of latitude. Solid lines show model results with the inclusion of seasonal polar temperatures while dashed-dotted lines the results with annual average temperatures. Bottom: ratio of the north and south concentration of cold trapped molecules as a function of latitude.

are shown to have a larger influence over the short-term infall rate as they impede the progress of particles to the polar regions and prolong the migration timescale, and thus their inclusion within exosphere models is essential for examining the instantaneous surface and exospheric concentrations, as would be needed for model/observational comparisons. SSRs, however, are unlikely to have a significant effect in the long-term capture and infall rates.

With respect to the depositional trends, Figure 6.4 shows the latitudinal dependence of the infall rate for H_2O with and without seasonal temperature data. Note

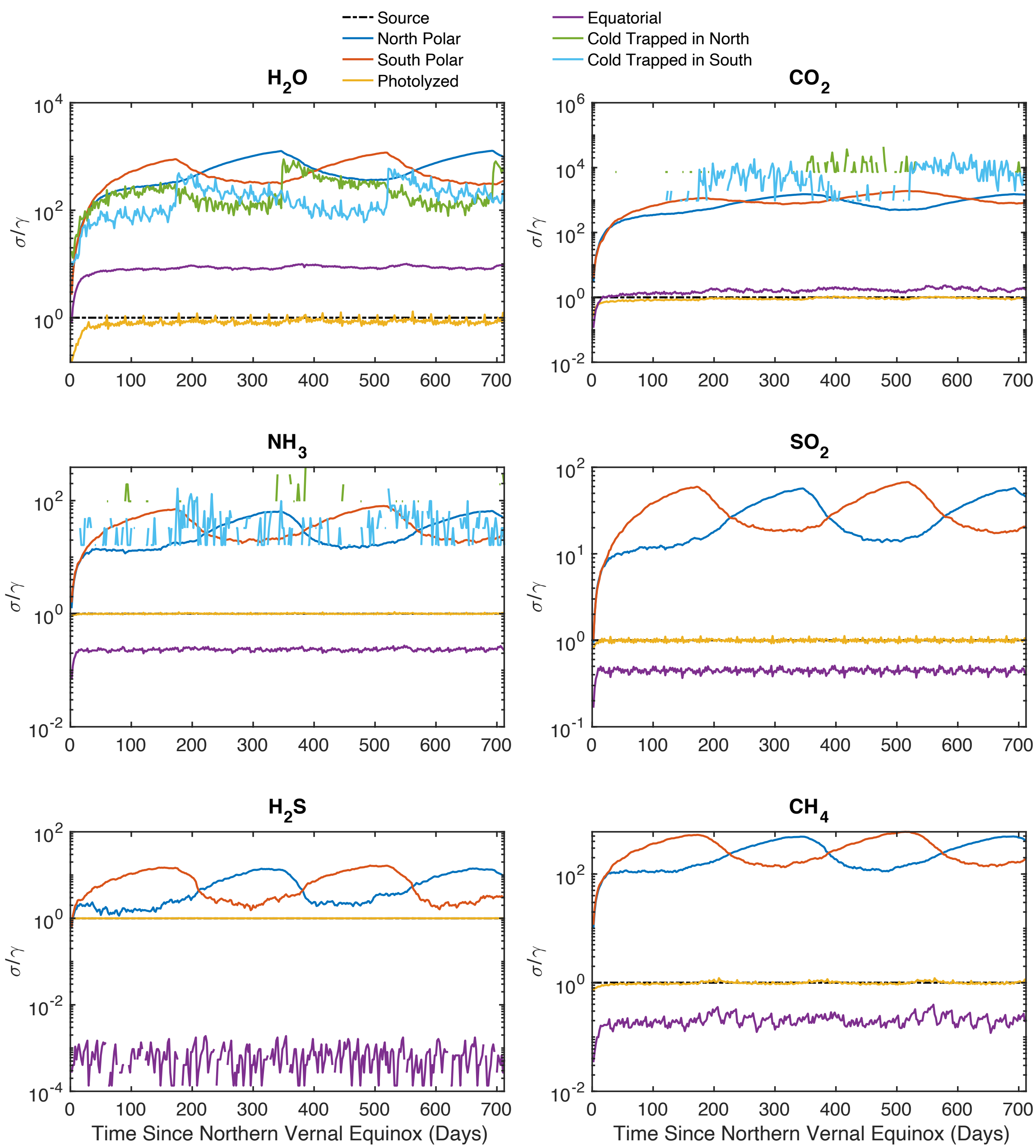

Figure 6.5: Time evolution of the surface densities, cold trapping and photolysis statistics.

that these data differ from those shown in Figure 5.5c as the updated model includes only cold trapping surfaces ($T_{max} < T_v$), and thus provides a more robust look at patterns of long-timescale accumulation. There are several notable points here. The first is that although SSRs marginally increase the quantity of cold-trapped particles, they do not have a significant effect on the latitudinal dependence of the infall (i.e. the overall shape of the curves with and without SSRs is roughly the same). Second, given the differences in trapping area, the modeled concentrations here are larger than those reported in Chapter 5, which is an expected result given the efficiency of cold trap capture at high latitudes discussed earlier. Finally, and most interestingly, the north/south asymmetries reported in Chapter 5 are augmented when capture is restricted to cold trapping regions. In the north, the infall increase from 250γ at 80° up to 400γ near the pole, while the in the south the infall remains fairly steady at 250γ. At latitudes pole-ward of 85°, σ is $\sim$60% larger in the north than in the south. It is intriguing to note that some orbital data bear evidence for a north/south asymmetry in volatile content. Spectral IR measurements from the Moon Mineralogy Mapper observed up to 750 parts per million (ppm) H_2O at northern high latitudes and only 500 ppm at southern high latitudes (Li & Milliken, 2017), although due to low signal-to-noise data were unable to be interpreted pole-ward of 85° where we observe the largest north/south difference. Neutron data also show asymmetric polar hydrogen distributions: the Lunar Prospector Neutron Spectrometer found lower epithermal neutron counts (higher hydrogen abundances) at northern high latitudes (Feldman et al., 1998). These data, however, are in contrast with LOLA measurements which show temperature-reflectance correlations in the south but not in the north (Fisher et al., 2017).

Figure 6.5 plots the modeled time variation in the aggregate surface density, cold trapping and photolysis statistics over the two year examination period. The polar curves are given as the total particle count poleward of 80° weighted by the polar area, and the equatorial curve is the same for the region of the surface equatorward of 80°. In all cases the data are normalized by the supply rate γ. Seasonal respiration is observed at the polar regions as a natural result of the lunar obliquity, highlighting that seasonal temperature variations influence not only H_2O but other condensible species as well. The timing of the peak abundance is shown to be independent of the vapor species, although differences in the seasonal amplitude are apparent. As observed with H_2O in Chapter 5, a lag in the annual peak surface density occurs due to seasonal retention, with the peak occurring 94 Earth days (3.2 lunar days) after the summer solstices. For cold trapping species such as H_2O, CO_2 and NH_3, the liberation of particles from seasonal cold traps corresponds to a surge in the flux entering the permanent cold traps.

It is also worth noting that seasonal condensation influences the surface concentration away from the poles as well, as a fraction of the particles released from seasonal cold traps migrate toward the equator. Figure 6.6 shows the infall rate at latitudes between 66° and 78° N and S. Surges in the surface concentration occur during periods of seasonal release, where the amplitude of the surge is more than twice the background concentration at 78° N and S. The seasonal amplitude quickly decays moving away from the pole as molecules diffuse across the surface, and is almost entirely

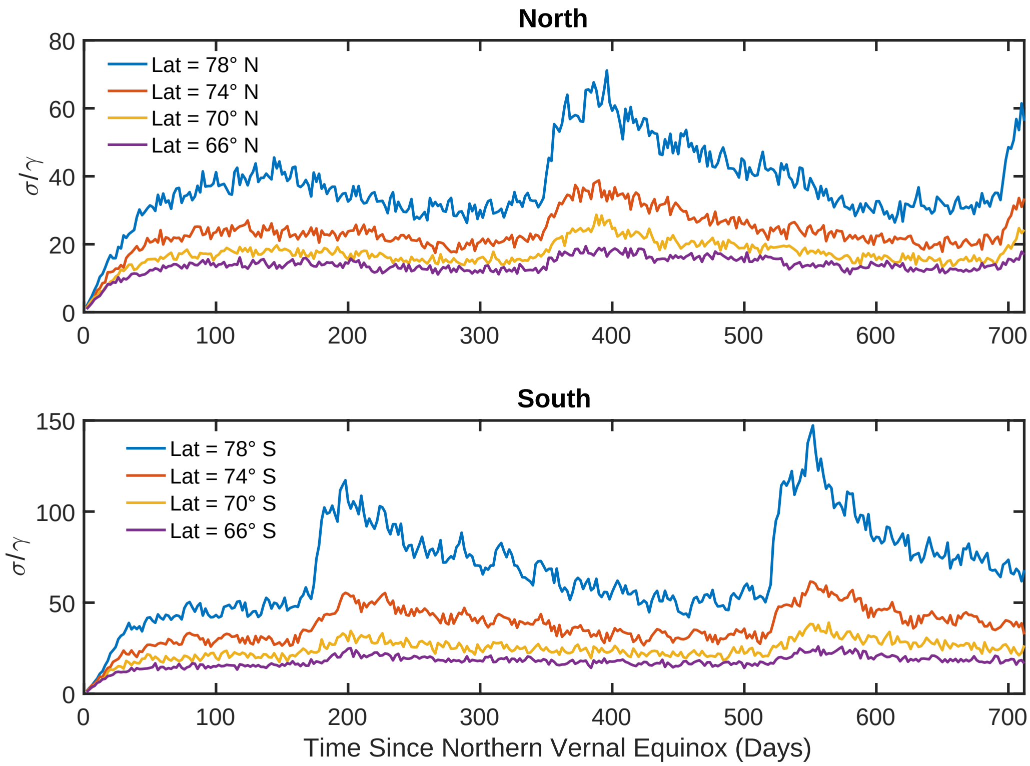

Figure 6.6: H_2O infall rate at non-polar latitudes showing seasonal spikes in the surface concentration as a result of large release of seasonally trapped water.

absent at 66° latitude. These results may have relevance for future missions seeking to observe time-varying (i.e. diurnal or seasonal) densities on the surface or in the exosphere.

6.3.2 Surface Mass Flux Within Permanently Shadowed Craters

In addition to surface densities, the model tracks the flux of particles entering selected[2] PSR craters; Figure 6.7 displays the resulting infall rates for four craters of interest for exploration, including the LCROSS impact site Cabeus. For clarity, only CO_2,

[2]The selected craters are the same as those discussed in Chapter 3 and are listed in Appendix Table A.1.

H_2O and CH_4 are shown.

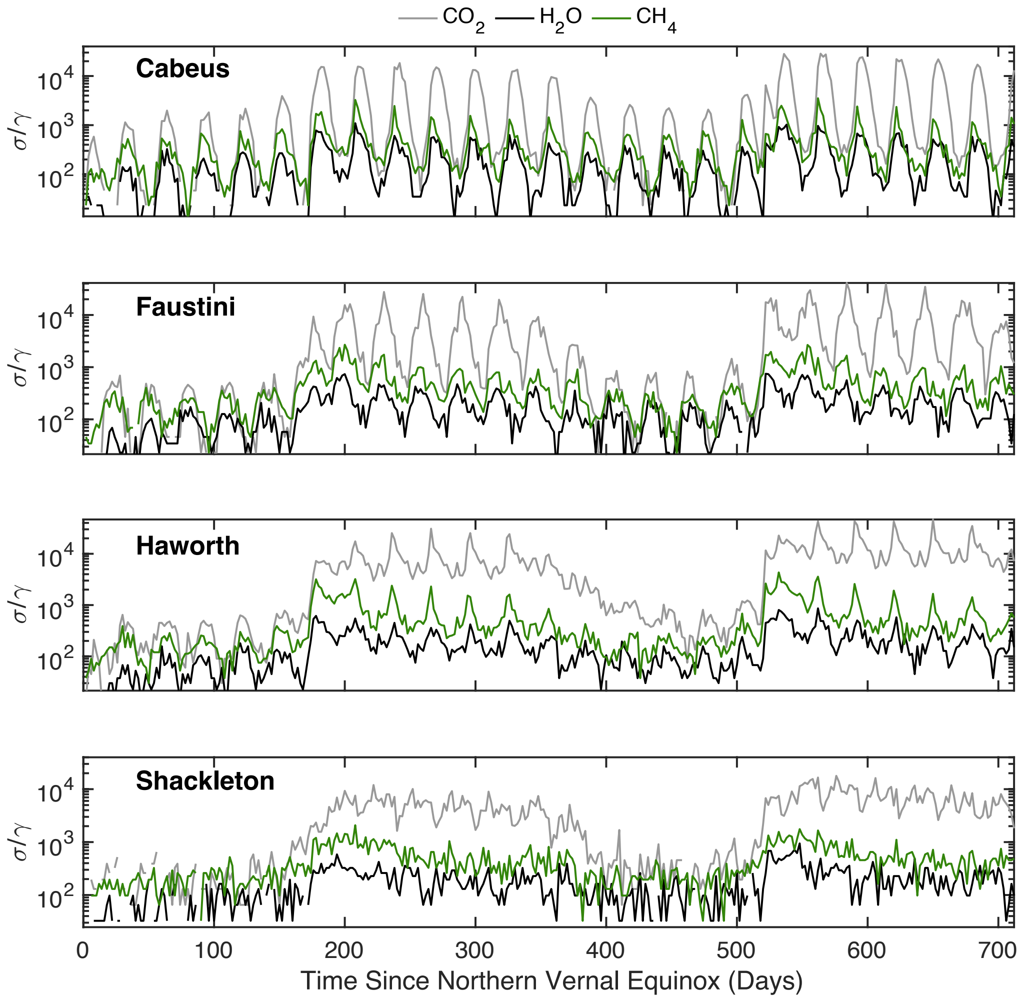

Figure 6.7: Time variation in the infall rate for selected craters at the lunar south pole. For clarity, only three of the studied volatiles are shown.

In effect, Figure 6.7 shows the supply rate from a steady state exosphere to different locations on the lunar surface, and because these data are normalized by the modeled source rate γ, the absolute infall rate can be deduced if the delivery/production rate of a given species is known. As noted above, the infall from meteoritic material is of particular interest as it represents a quasi-continuous source of volatiles to the Moon, both in delivering exogenous material and liberating solar-wind generated species. Morgan, Zook, and Potter (1989) and Horanyi and Szalay (2017) estimate a meteoritic supply rate of 1.5×10^{-15} kg m^{-2} s^{-1} to the Moon, and that the composition of this material resembles that of interplanetary dust particles (IDPs). IDPs are small, primitive materials derived primarily from volatile-rich bodies such as comets and asteroids, although their volatile makeup may not necessarily be representative of their parent bodies due to their continual exposure to UV radiation in the inner solar system. Laser microprobe studies of chondritic IDPs have detected H_2O and CO_2 in quantities of 1% by mass (Gibson Jr, 1992), in addition to CH_4, SO_2 and H_2S in lower relative abundances (Gibson & Sommer, 1986), although it is unclear whether these studies accounted for the volatile loss during atmospheric entry. Previous investigators have assumed slightly larger H_2O and CO_2 mass fractions of 3-5% (Arnold, 1979; Morgan & Shemansky, 1991).

Of course, only a fraction of the impacting meteoritic material will survive as a result of the high impact velocities. Benna et al. (2019) calculate that up to two-thirds of the impact vapor will exceed the lunar escape velocity and be immediately lost, while the remaining one-third will be redeposited on the surface. Farrell et al. (2019) suggests that the survival fraction may be larger than 33%, however, again to be conservative, we will assume that 33% of the impacting material survives and is capable of diffusive lateral transport. Taking this into account and assuming a 1% mass fraction, we estimate the meteoritic supply rate, $\dot{S}$, for CO_2 to be $\dot{S}_{CO_2} \approx$

5×10^{-18} kg m^{-2} s^{-1}. This is about an order of magnitude smaller than the calculated supply rate for H_2O, $\dot{S}_{H_2O} \approx 6.6 \times 10^{-17}$ kg m^{-2} s^{-1} (Benna et al., 2019), perhaps as a result of more efficient production of H_2O molecules via solar wind relative to CO_2, or a larger mass fraction within IDPs.

The principal source for methane, given its relatively low abundances in IDPs (Gibson & Sommer, 1986), is the solar wind. Hodges Jr (2016) discusses the formation of CH_4 from solar wind-derived carbon, calculating that 25-75% of the global carbon influx is converted to methane and diffuses upward into the exosphere. This amounts to a methane source rate of $\dot{S}_{CH_4} \approx 2.1 \times 10^{-18}$ kg m^{-2} s^{-1}, similar to that calculated above for CO_2. It is reasonable to assume that some of the incoming solar-wind carbon forms other carbon-bearing species such as CO and CO_2 as well, although the efficiency with which this occurs is not well documented and/or understood. Here, we will make a conservative estimate and assume only exogenous delivery of CO_2 to the lunar surface and solar wind generated CH_4. Unfortunately the supply rates for H_2S, SO_2 and NH_3 are also difficult to quantify with the available data, and due to the difficulty in constraining the source rates for these species the remaining analysis will focus on H_2O, CO_2 and CH_4.

The annual average infall rate modeled for each crater is plotted as a function of latitude in Figure 6.8; scaling these by the supply rate, $\dot{S}$, for each species calculated above, Figure 6.8 also shows the estimated annual average mass flux entering each crater. With the exception of the south polar H_2O data, the infall rate is generally

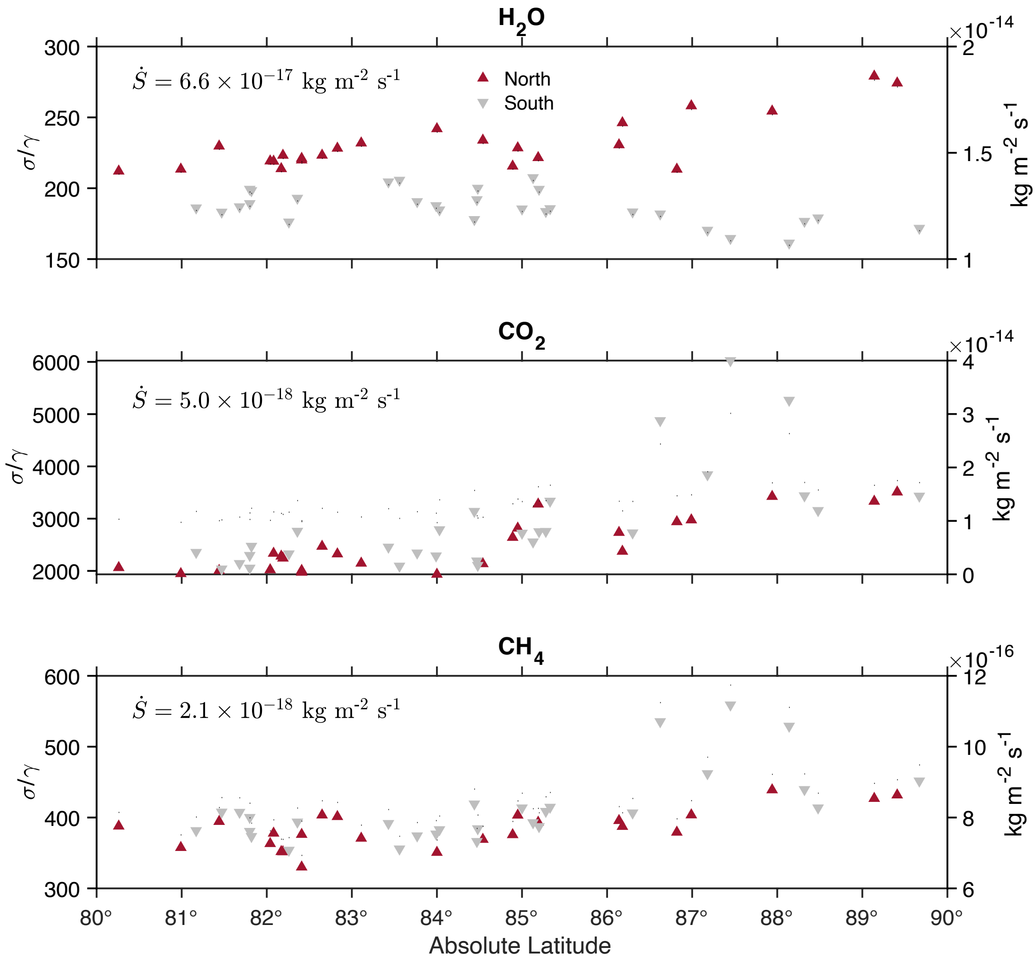

Figure 6.8: Variability in the annual average infall rate for different impact craters containing PSR. Each data point represents a different crater.

increased within high latitude craters as a result of the colder temperatures, which produce shorter and more numerous ballistic hops. The H_2O data in the south are exceptional due to the significantly larger cold trap area for water in the southern hemisphere (see Table 6.2). In the south, the lower-latitude cold traps act as barriers to the poleward migration of H_2O (Moores, 2016), which reduces the number of particles hopping at high southern latitudes and leads to significant north/south asymmetries in the infall rate. As the Moon contains little to no trapping area for CO_2

and CH_4, these gasses travel largely unimpeded to the high latitude polar regions. Differences in the infall rate of CO_2 and CH_4 are principally due to differences in their photolytic lifetimes. The average mass flux for H_2O, CO_2 and CH_4 is 1.40×10^{-14} kg m^{-2} s^{-1}, 1.35×10^{-14} kg m^{-2} s^{-1}, and 8.37×10^{-16} kg m^{-2} s^{-1}, respectively.

To determine the implications of these data in terms of the surface mass balance, the supply rate to the permanently shadowed regions must be weighed against sources of loss such sublimation, sputtering, impact vaporization and impact gardening. Following Hayne et al. (2015), the mass balance can be written as:

$$\frac{dm}{dt} = \dot{S} - \dot{E}_{sub} - \dot{E}_{*} - \dot{E}_{IV} - \dot{E}_{g} \tag{6.4}$$

where $\dot{E}_{sub}$ is the loss rate due to sublimation, $\dot{E}_{*} \approx 2.4\times10^{-18}$ kg m^{-2} s^{-1} is the loss rate due to sputtering (Farrell et al., 2019), $\dot{E}_{IV} \approx 7\times10^{-16}$ kg m^{-2} s^{-1} is the loss rate due to impact vaporization (Cintala, 1992; Pokorný et al., 2020) and $\dot{E}_{g} \approx 10^{-15}$ kg m^{-2} s^{-1} is the burial rate due to impact gardening (Hurley et al., 2012). Figure 6.9 plots the thermal and non-thermal loss rates. Due to the exponential dependence on temperature, $\dot{E}_{sub}$ will dominate at temperatures $> T_v$. For example, for CO_2, the sublimation rate at T = 100 K is 3×10^{-5} kg m^{-2} s^{-1}, or $\sim$13 orders of magnitude greater than the supply rate. At lower temperatures, however, sublimation becomes less important. At T = 50 K, the rate of sublimation drops to approximately 3×10^{-19} kg m^{-2} s^{-1} (see Figure 6.9), which is $\sim$4 orders of magnitude less than the average infall rate.

Whether or not burial via impact gardening is a loss depends on the whether the inventory being considered is surficial or subsurficial. For impacting probes such as LCROSS which excavated several meters into the surface (Colaprete et al., 2010), or neutron spectra which are sensitive to several meters in depth (Feldman et al., 2000; Mitrofanov et al., 2010), burial is not necessarily a loss. In fact, the process of burial would have a protective effect on PSR ices both by shielding them against sublimation loss and impact vaporization. For instruments that are only sensitive to the uppermost regions of the surface, however, burial serves to remove ice beyond the detection threshold, and therefore functions as a loss. Positive identification of surface-exposed H_2O and CO_2 (Fisher et al., 2017; Hayne et al., 2015; Hayne et al., 2019; Li et al., 2018) would therefore suggest that the supply rate at least locally exceeds the loss rates (including $\dot{E}_g$) in equation 6.4, although it would not imply a source mechanism.

For CO_2 and H_2O, we find that the meteoritic supply rate, coupled with the modeled infall rates into polar craters, exceeds the loss rates over a specified thermal range determined by the sublimation rate. For CO_2, $dm/dt > 0$ for surfaces with $T_{max} < 60$ K, and for H_2O $dm/dt > 0$ for surfaces with $T_{max} < 112$ K (Figure 6.9). For locations that meet these thermal criteria, net deposition of meteoritic H_2O and CO_2 is expected to be an ongoing process, such that these surfaces would maintain fresh ice deposits. Moreover, the calculated average filling rate $\overline{dm}/dt$ is reasonably large: for H_2O and CO_2, $\overline{dm}/dt \approx 1.3\times10^{-14}$ kg m^{-2} s^{-1}, which is equivalent to 4.6

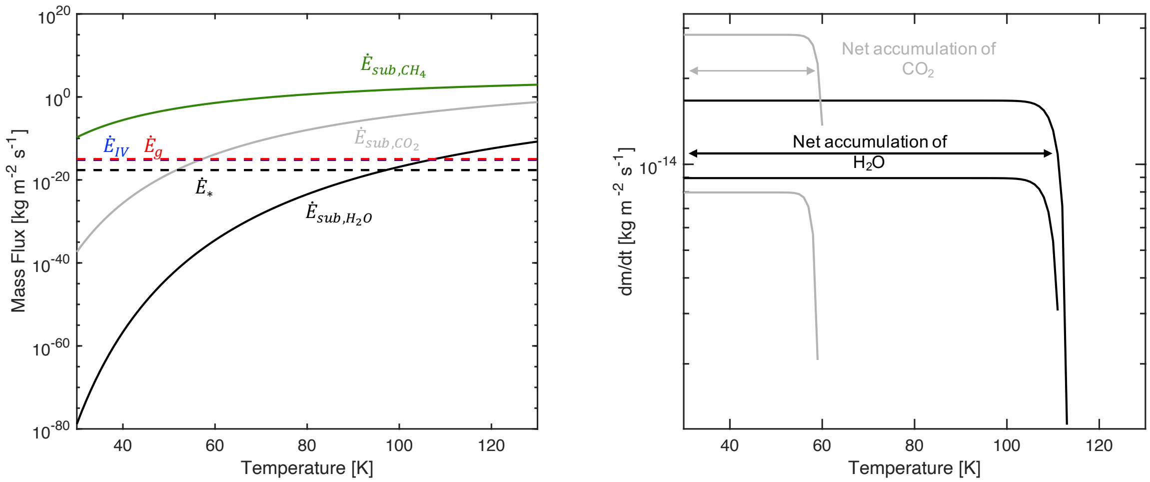

Figure 6.9: Left: comparison of the mass loss rates including sublimation (solid lines) and sputtering, impact gardening and impact vaporization (dashed lines). Note that impact vaporization (blue; $\dot{E}_{IV} \approx 7{\times}10^{-16}$ kg m^{-2} s^{-1}) and the gardening rate (red; $\dot{E}_g \approx 10^{-15}$ kg m^{-2} s^{-1}) appear approximately equal on the y-axis scale. Right: change in mass flux as a function of temperature for H_2O (black) and CO_2 (gray). The two lines shown for each species represent the upper and lower boundaries of the supply rate (i.e. the maxima and minima from Figure 6.8). The arrows show the temperature range for which $dm/dt > 0$.

$\times 10^{11}$ and $1.8{\times}10^{11}$ molecules m^{-2} s^{-1}, respectively. At this filling rate, it would take only 35,000 years to reach the H_2O concentration detected by LCROSS ($5.4{\times}10^{23}$ molecules m^{-2}), and only ∼2,000 years to match the CO_2 concentration ($1.1{\times}10^{22}$ molecules m^{-2}). Given that cold traps have been stable for ∼2 billion years (Siegler et al., 2015; Ward, 1975) and assuming the meteoritic supply rate to be constant over this timescale, significantly larger molecular surface concentrations ($\times 10^5$) would be expected based on the filling rates calculated above. The discrepancy would be even greater is subsurface deposits were considered.

A number of factors can be invoked to explain these inconsistencies. A relatively straightforward explanation could be that supply/loss rates are over/under predicted.

As for the loss rates, the above calculations assume constant rates for $\dot{E}_*$ and $\dot{E}_{IV}$, although in reality the sputtering and impact vaporization yield should scale according to the ice concentration (Farrell et al., 2019). Farrell et al. (2019) argues that these set a limiting rate for ice accumulation, and that the age of the exposed ices at the polar regions may not exceed 1,500 years. These estimates, however, assume equal exposure to micrometeoroid bombardment and solar wind plasma, which, as these authors acknowledge, is not necessarily the case. Secondary impact craters, which are often the coldest locations within PSRs as they are doubly shadowed from reflected sunlight, have restricted fields of view and may be partially shielded from incoming meteoroids. Furthermore, in addition to vaporizing material, impacting meteoroids are also bringing volatiles to the surface, although the fraction of volatiles that are implanted into the surface at the impact site (as opposed to ejected outward and transported to another location) would be difficult to estimate. There is, of course, a degree of uncertainty in the supply rates that are estimated for H_2O, CO_2 and CH_4, although it is unlikely that the uncertainty in this parameter is large enough to the sole cause. An additional source of uncertainty in the calculations above is the efficiency of lateral transport to the polar regions. As described in Chapter 2, Hodges (2002) has argued based on the behavior of Argon in the lunar exosphere that lateral transport of H_2O is inefficient due to the high adsorption potentials of soil grains, and that only 3–6% of water accumulated in the regolith may be moved to the polar cold traps. In this case, the computed infall rates (Figure 6.8), at least for H_2O, would be substantially smaller. The repeated exospheric detection of CH_4 by LADEE (Hodges Jr, 2016) would suggest that the transport efficiency is larger for CH_4 than it is for H_2O, particularly given its smaller source rate. A similar argument could be made for CO_2, which has been observed more prominently in the exosphere (Stern, 1999) relative to H_2O.

The detection of CH_4 by LCROSS is more difficult to explain with the modeled source rates and infall rates. The average mass flux into a polar crater for CH_4 is $\sim 8.4\times10^{-16}$ kg m^{-2} s^{-1}, which is equivalent to 1×10^{9} molecules m^{-2} s^{-1}. Examination of Figures 6.8 and 6.9 show that the infall rate for methane never exceeds the loss rates (dm/dt is always < 0), meaning that even short-term preservation of methane is difficult due to its high volatility, and for the fact that $\dot{E}_{sub} > \dot{E}_g$ (i.e. it will be sublimated away faster than it can be buried and protected from sputtering and impact vaporization). If high activation energy grain sites exist for methane, the residence times for CH_4 may be significant enough to explain the concentrations detected by LCROSS. Additionally, as noted above, chemical reactions taking place within a PSR would further complicate the mass balance calculations presented here (Colaprete et al., 2010).

7 Surface Roughness Effects of Volatile Migration

7.1 Chapter Overview

The behavior of atoms and molecules at grain-scales is a largely unexplored aspect of exospheric migration, and, due to the computational complexity, is often neglected in models of surface transport. Yet, as was noted in the Introduction, roughness at grain scales may influence the vertical and lateral transport of exospheric species in a number of ways. One way in which this roughness is expected to play an important role is through the alteration of the velocity distribution of upwelling particles at the exobase. As will be shown, topographic obstruction is considerable at grain scales, and the barriers posed to particles emitted at large emission angles lead to non-uniformities in the vertical velocity distribution. These trajectory modifications in turn have consequences for the vertical structure of a thermalized exosphere.

In this chapter, we examine the effects of exobase collisions on the thermal, upwelling velocity distribution. To perform this work, a roughness model is developed that is intended to simulate the lunar landscape at scales of regolith grains, and the illumination and thermal environment of these artificial surfaces are modeled using ray-tracing and a 1-D thermal model, respectively. Due to the difficulty in obtaining analytic solutions, we employ a Monte Carlo approach to simulate the gas-surface collisions that occur at the exobase and examine the role that these collisions play in the expected vertical exospheric density profiles.

7.2 Methods

7.2.1 Generation of Gaussian Rough Surfaces

A convenient way to simulate surface topography is to assume a Gaussian height and slope distribution (Rubanenko et al., 2020; Shepard & Campbell, 1998; Smith, 1967), where the degree of roughness is often characterized using the root mean square (RMS) slope, σ_s, of the surface. σ_s varies depending on the horizontal scale being considered: using Apollo imagery, Helfenstein and Shepard (1999) measured the RMS slope of undisturbed regolith at submillimeter scales to be up to 55°; for comparison, σ_s was measured to be $5° - 10°$ at a 240 meter baseline (Rosenburg et al., 2011).

In this work, Gaussian surfaces are generated following the procedures outlined in the Appendix material of Jacobs, Junge, and Pastewka (2017). A 150×150 pixel matrix is seeded with a random Gaussian field with zero mean and $\sigma = 1$. The

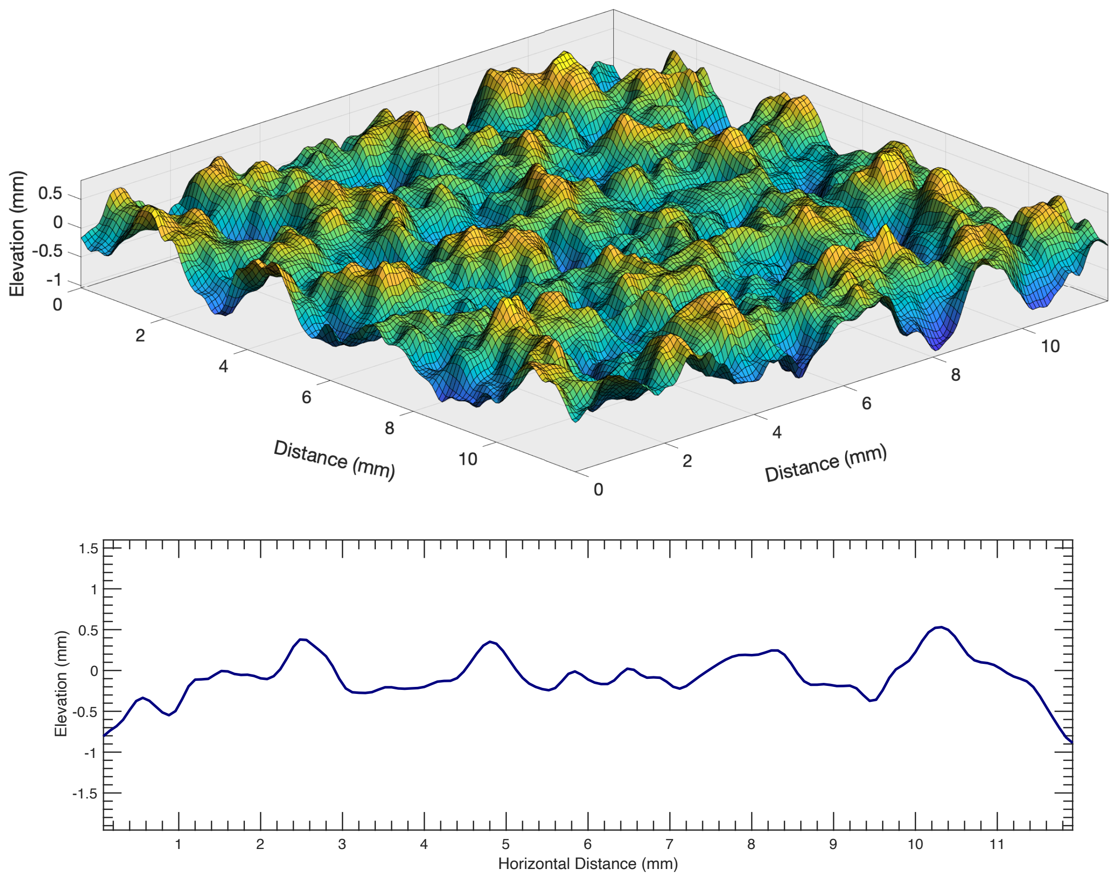

Figure 7.1: Top: Gaussian rough surface created with 0.5 m/pixel resolution and an RMS slope of 45°. Bottom: transect through the center of the DEM. The profile is shown without vertical exaggeration.

power spectral density (PSD) is obtained using a 2D Fast Fourier Transform, and the magnitude of the PSD is subsequently scaled by a power law using a Hurst exponent, H ($0 < H < 1$), which describes how the degree of roughness changes with lateral scale. A Hurst exponent of 0.95 has been measured for the lunar regolith (Cai & Fa, 2020; Rosenburg et al., 2011), and is adopted in this work. To imitate the surface at micro-scales, the PSD is filtered to eliminate short and long-wavelength topographic features beyond a specified threshold. The surface is then transformed into an elevation map using an inverse FFT, and the magnitude is subsequently scaled to the desired RMS slope. A resulting elevation map of a Gaussian rough surface is shown in Figure 7.1 for $\sigma_s = 45°$. Each side of the surface measures 12 mm in length, resulting in a map resolution of 80 μm pix^{-1}. This resolution was intended to mimic the lunar surface at the grain scale, which has a median particle size of 40-130 μm (Carrier, 1973).

7.2.2 Illumination and Thermal Modeling

To model the temperature of the surface, we must first obtain the input energy due to solar radiation. This is achieved using techniques already described in this thesis. Horizon profiles are computed for the Gaussian surface using a ray tracing algorithm and a 1° azimuthal spacing. The surface is modeled at latitudes between 0° and 80° north at 10° increments, and the solar irradiance is computed over a two lunar year time frame using a 1-hr step size. Modeling the indirect flux received by shadowed surfaces proved to be a computationally intractable problem for the number of surfaces and time steps needed. Thus, to simplify the problem, we adopt the method from Prem et al. (2018) and fill in shadowed surfaces using a constant 250 W m^{-2} scaled according to the cosine of the latitude at which the surface resides. Figure 7.2a-c shows three examples of the irradiance calculation at various latitudes. To verify our illumination results, we compare our ray-tracing output with an analytical expression derived by Smith (1967) in panel d of Figure 7.2. This figure shows the fraction of

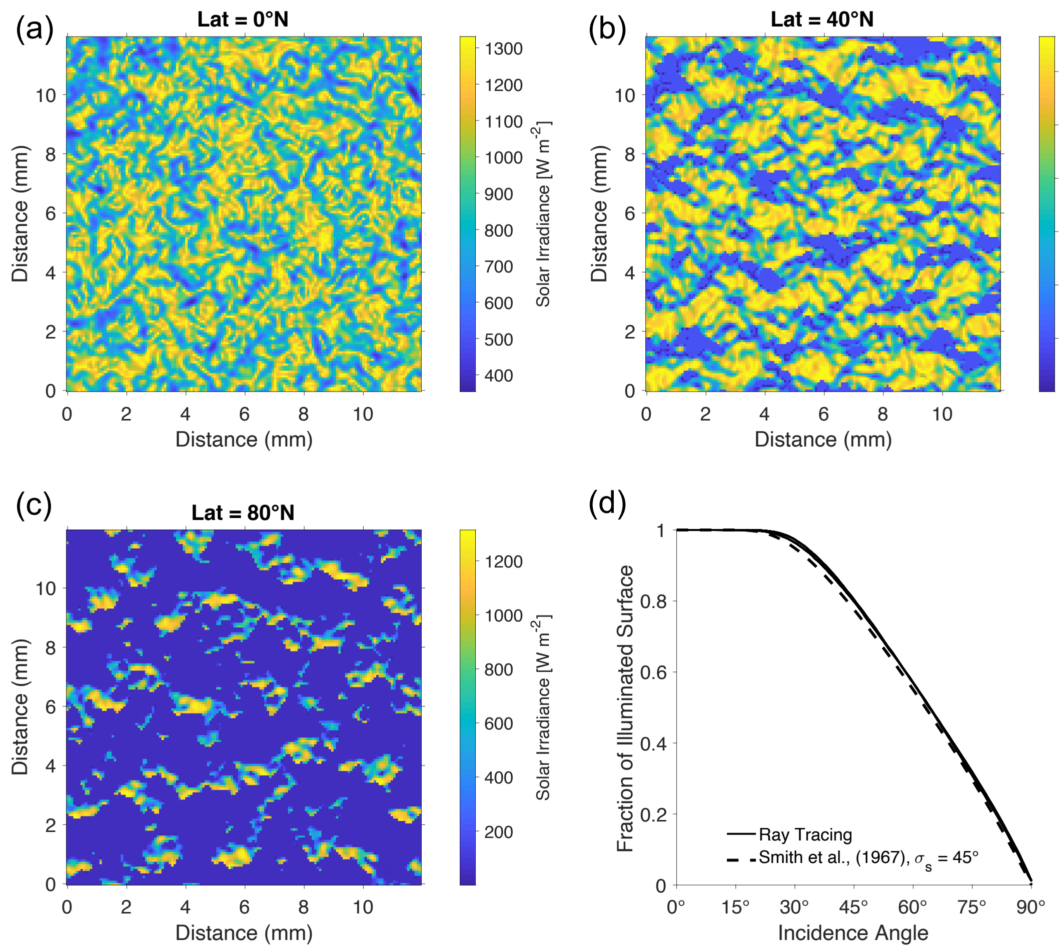

Figure 7.2: (a-c) Modeled solar irradiance (W m^{-2}) for a Gaussian rough surface at various latitudes. Data are shown for local noon when the irradiance is maximized. (d) Comparison the fraction of the illuminated surface of ray-tracing results and shadow hiding expression of Smith (1967).

the surface that is illuminated by the Sun as a function of incidence angle. As seen here, good agreement is found at all incidence angles.

Using the modeled solar irradiance the surface temperature is determined by applying a Crank-Nicolson scheme (Crank & Nicolson, 1947) to the 1-D heat equation:

$$\rho c \frac{\partial T}{\partial t} = \frac{\partial}{\partial z}\left(k \frac{\partial T}{\partial t}\right). \tag{7.1}$$

Here, $\rho c = 10^6$ J m^{-3} K^{-1} is the volumetric heat capacity, T is temperature, t is time, z is depth and $k = 2.5\times10^{-3}$ W m^{-2} K^{-1} is the thermal conductivity. Thermal boundary conditions are set using Stefan-Boltzmann law, and the model is allowed to equillibrate for 1 year prior to emplacing particles on the surface.

Thermal instabilities can sometimes occur in the model as shadowed surfaces abruptly emerge into sunlight, causing a large change in the input energy and unrealistically high temperatures. To minimize these irregularities, we subdivide the input energy using an artificial flux smoothing technique, which consists of averaging together two adjacent flux maps on a pixel-by-pixel basis. This was found to drastically reduce instabilities, although it did not eliminate them entirely. An improvement to this technique could consist of a linear flux interpolation between adjacent time steps for each pixel, and this may be incorporated into a future version of the thermal model. Here, however, pixels with modeled temperatures exceeding the maximum thermal IR temperature measured by Diviner (397 K) are filled in using the temperature average of its 8 neighboring pixels which lie below this threshold.

Figure 7.3a-c shows the modeled temperatures at local noon for the same latitudes shown in Figure 7.2; panel d shows the mean of the surface at local noon as a function of latitude, with Diviner data (Williams et al., 2017) shown for comparison. When surfaces are averaged, modeled temperatures are reduced relative to Diviner data as a result of the inclusion of small-scale shadows and highly sloped surfaces. These discrepancies may, in part, be explained by the omission of lateral heat conduction in

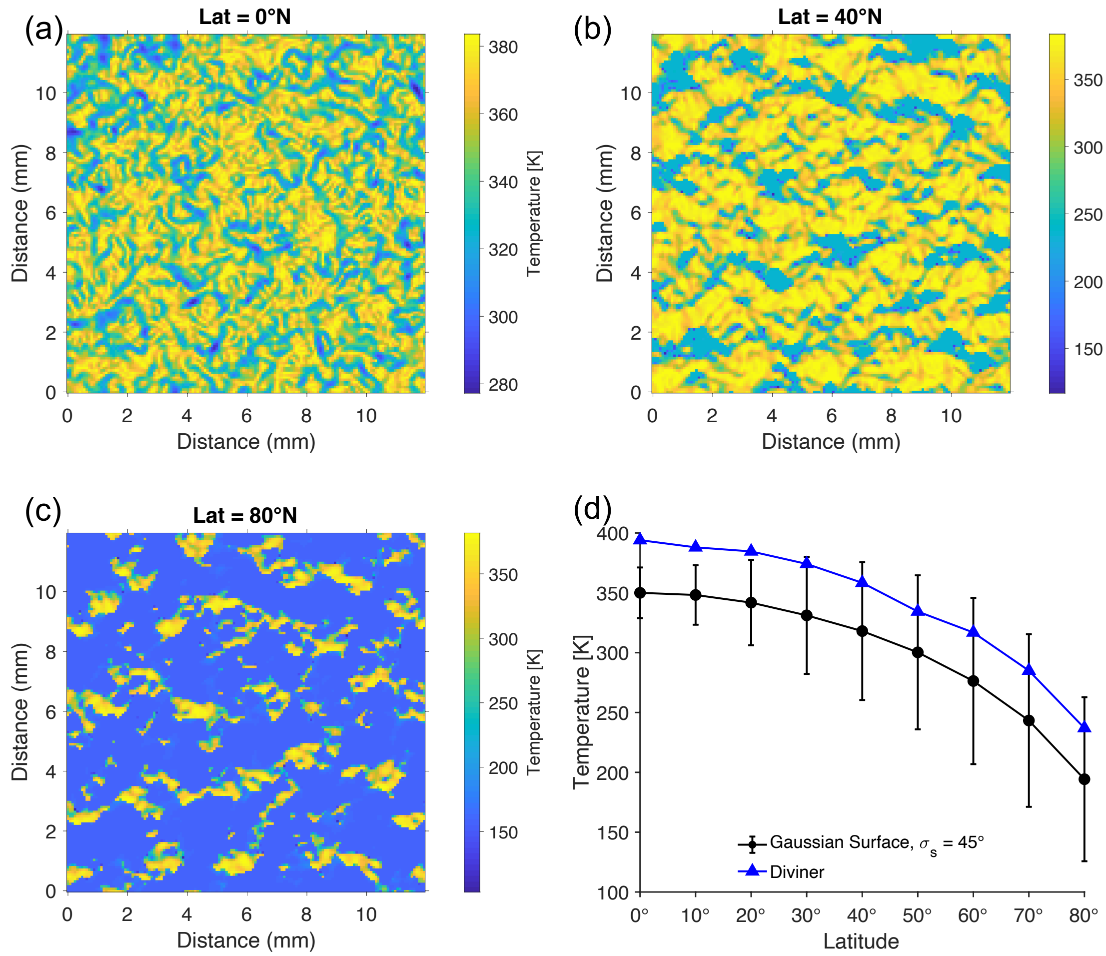

Figure 7.3: (a-c) Modeled temperature distributions for a Gaussian rough surface with $\sigma_s = 45^{\circ}$. Temperatures were computed using a 1-D thermal model which includes subsurface conduction. Data are shown at local noon. (d) Comparison of Diviner and modeled noon-time temperatures. Modeled data are shown with 1-σ error bars.

the thermal model, which is important at the scales considered in this work (Hayne, Aharonson, & Schörghofer, 2020). With the inclusion of lateral conduction, the thermal environment at micro scales is expected to be significantly more uniform than is modeled here, which will ultimately have implications for the upwelling velocity distributions. While future work will explore the effects of lateral conduction on the small scale temperature gradients, here we examine the extreme case of large thermal variations and its effect on the vertical velocity exospheric profiles.

7.2.3 Monte Carlo Model

Molecules are initialized at local noon and are assigned random map coordinates on the DEM. Residence times τ are updated using a 1-hr time step (Δt), and, as before, molecules are released when $\tau < \Delta t$. The azimuthal angle of the velocity vector, θ, is determined first and is drawn from a uniform probability distribution between 0 and 2π. The azimuthal angle is used to ascertain the topographic profile in the direction of the jump by tracing a great circle arc from the particle location to the DEM boundary. To deal with particles residing at the edge of the DEM, the topographic landscape is assumed isotropic and is expanded to a 3×3 grid where each grid quadrant contains a copy of the DEM (Figure 7.4). Due to the symmetry produced by the Fourier transform, the elevation profile is continuous between neighboring quadrants (i.e. no artifacts occur using this technique).

The zenith angle, ϕ, of the velocity vector is drawn from a uniform probability distribution weighted by a cosine factor to account for the decreasing spherical area moving toward the zenith point. In theory, ϕ may exceed 90° if a particle resides on local topographic maximum, and thus ϕ_{max} is determined as 90° - dy/dx where dy is the change in elevation between the particle and the adjacent grain and dx is the change in horizontal distance. The speed of the particle is drawn from an

Armand distribution (Equation 2.4) evaluated using the local surface temperature. The trajectory of an emitted particle is tracked using a fourth order Runga-Kutta scheme using a time step of 4×10^{-8} seconds to model the flight path at μm–mm scales.

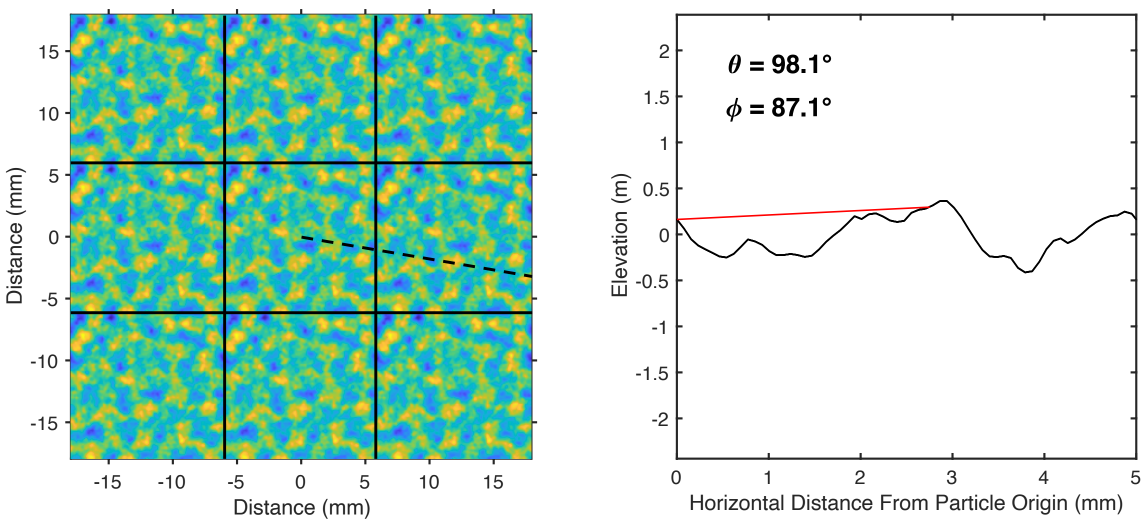

Figure 7.4: Left: Expanded Gaussian surface segmented into a 3×3 grid. Each quadrant of the grid is a copy of the 12×12 mm DEM shown in Figure 7.1. The central quadrant is where particles are sourced in the simulations. The dashed line shows the flight path of particle launched at $\theta = 98.1°$. Right: topographic profile (black) at $\theta = 98.1°$ shown with the particle flight path (red) launched at $\phi = 87.1°$.

The elevation of the particle and its horizontal distance from the origin location are tracked at each modeled time step and cross-referenced with the elevation of the surface at the corresponding lateral distance (i.e. sub-particle point). If the elevation of the particle is less than the elevation of the topographic profile at the sub-particle point, the impact location is recorded and the process is repeated for the particle at its new location (the impact site). Particles hopping to an outer quadrant of the DEM grid are relocated to the counterpart coordinates within the central quadrant. The particle is allowed to hop as many times as needed until it travels beyond the confines of the DEM. Once this occurs, the simulation is terminated and the model returns the number of jumps required to escape, the Cartesian velocity components of the escape jump, and the temperature at which the particle was launched. Each simulation was conducted using 500,000 particles using the cometary species discussed in Chapter 6.

7.3 Results and Discussion

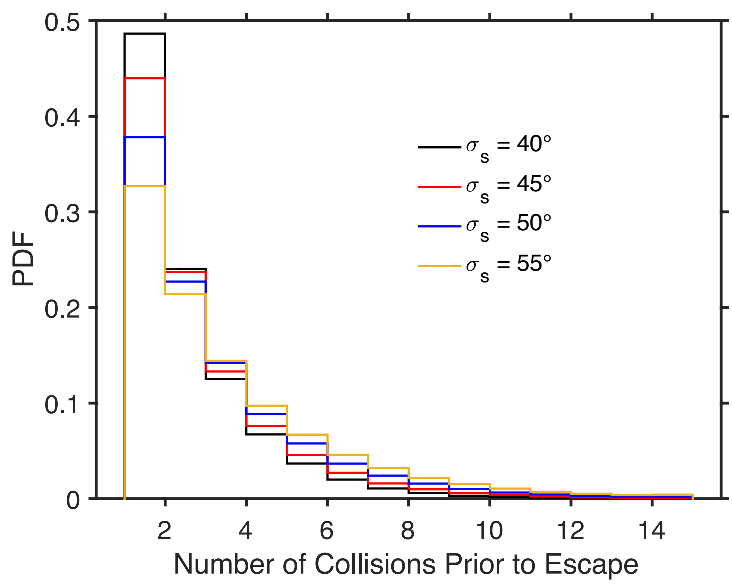

Figure 7.5: Histogram showing the number of particle-regolith collisions prior to emergence into the exosphere. Data were modeled using a rough Gaussian surface with varying RMS slope between $\sigma_s = 40° - 55°$.

A histogram of the resulting number of collisions prior to emergence from the soil is shown in Figure 7.5, where the data are normalized as a probability density function (PDF) such that the area under the curve is equal to 1. The results here are shown for H_2O only, as variance in these data are not observed between molecular species. A significant majority of the particles escape the regolith immediately, where the probability of making numerous collisions before emergence decreases exponentially from 1. Of course, at increasing roughness scales particles experience more regolith encounters before escaping owing to the more extreme dynamic range of the topography. At $\sigma_s = 40°$, the mean and median number of collisions are 2.1 and 2.0, respectively; at $\sigma_s = 55°$, the mean and median are 3.3 and 2.0. Increasing the number of particle-regolith encounters will raise the chances of a particle finding a high activation energy adsorption grain site, micro cold trap or seasonal cold trap. All of these would serve to prolong the migration timescale (and decrease the transport efficiency); however, examining these effects is beyond the scope of this work.

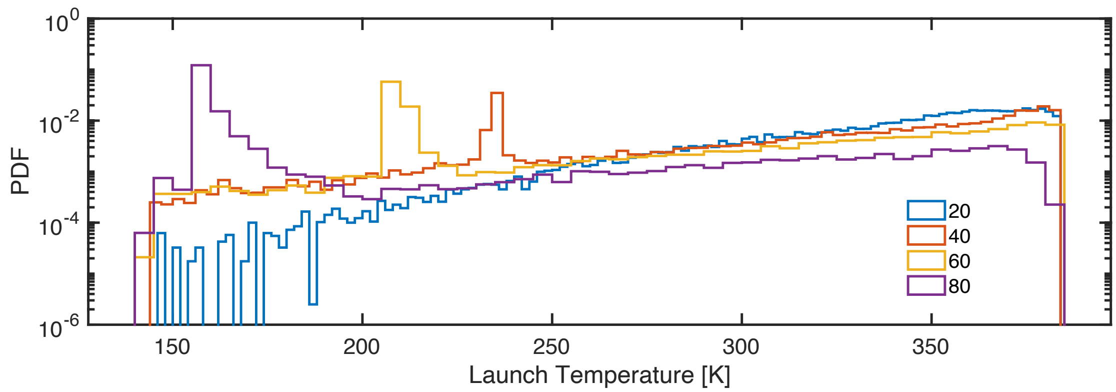

Figure 7.6: Probability distribution of the launch temperature, defined as the temperature at which a particle is released from the regolith on an escape trajectory. Data are shown for H_2O for a Gaussian surface with $\sigma_s = 45°$.

Figure 7.6 shows the temperature at which particles are launched from the regolith on an escape trajectory. Peaks are observed in the distribution at lower temperatures (T<250 K) as a result of release from shadowed surfaces, although this does not apply to the lower latitude regions ($\lambda = 0° - 20°$) where shadowing effects are reduced. As well, an increase in the probability distribution is observed moving toward higher temperatures, demonstrating that particles are preferentially released from warmer regions of the surface. This trend is visible at all latitudes, and can be explained using the following topographic and geometric arguments: (1) particles are more likely to be liberated from local topographic peaks where fewer obstructions exist, and (2) through examination of Figures 7.1–7.3, these local peaks also correspond to warmer regions of the surface. These two effects result in a bimodal temperature distribution with peaks at extreme high and low temperatures for non-equatorial surfaces.

The vertical velocity distribution for a rough exobase is shown in Figure 7.7a. Relative to a smooth surface (i.e. $\sigma_s = 0°$; also shown), roughness distributions are shifted toward the zenith as a result of topographic blocking at high emission angles, where the median value of ϕ for a smooth and rough surface is 60° and 44°, respectively. Because the vertical velocity determines the the trajectory of the particle and the flight duration, t_d, the shift in the angular distribution results in divergent near-surface vertical density profiles for rough and smooth exobases. Panels b and c of Figure 7.7 show the time-averaged profiles for H_2O, CO_2, CH_4, SO_2 and NH_3; these curves were generated through computational binning of the particle trajectories using a 50 meter and 1 second bin spacing. Examination of these two graphs show that the directional uniformity in the smooth exobase distribution produces a "ground-hugging" behavior at low altitudes that is inconsistent with a hydrostatic atmosphere,

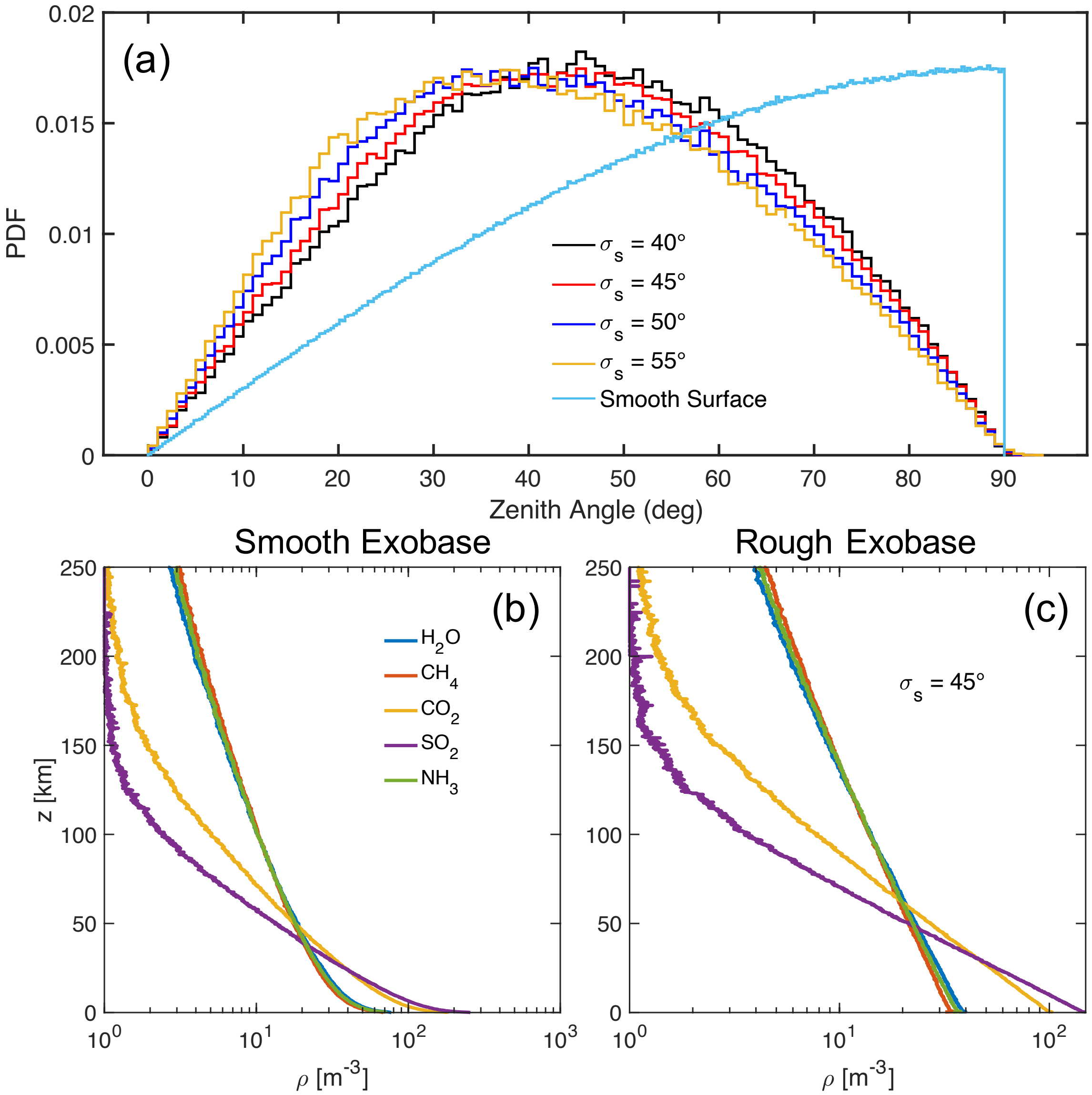

Figure 7.7: (a) Modeled directional distribution of upwelling particles from rough Gaussian surfaces. The directional distribution of a smooth surface ($\sigma_s = 0°$) is shown for comparison. (b) Time-averaged vertical density profiles for exospheric molecules computed with a uniform directional distribution (i.e. no topographic obstructions). (c) vertical density profiles computed with a rough surface. Rough surface distributions show an exponential dependence.

as the density fall off is greater than an exponential. In contrast, particle densities for rough surfaces decrease exponentially with increasing altitude.

Table 7.1: Calculated scale heights for smooth and rough exobase velocity distributions.

Species	$\mathbf{H_S}$ **[km]**	$\mathbf{H_R}$ **[km]**	$\mathbf{H_B}$ **[km]**	$\mathbf{H_R/H_S}$
H_2O	22.5	100.3	99.5	4.5
CH_4	26.6	116.3	111.6	4.4
CO_2	10.5	37.3	40.7	3.6
SO_2	7.5	25.9	27.9	3.5
NH_3	25.3	106.3	105.2	4.2

To appreciate these differences, Table 7.1 tabulates the scale heights, H, for the density profiles shown in Figure 7.7a and 7.7b. The exospheric scale height represents the vertical height above the surface at which the atmospheric density is reduced by a factor of $1/e$. For a barometric atmosphere, the scale height, H_B, is given by:

$$H_B = \frac{kT}{mg} \tag{7.2}$$

where k is the Boltzmann constant, T is the temperature associated with the source velocities, m is the molecular mass and g is the gravitational acceleration. As is shown in Table 7.1, the calculated scale heights for a rough exobase, H_R, agree well with the exponential scale heights, and are larger than the scale heights calculated for a smooth surface, H_S, by a factor of 3.5-4.5. These data have relevance for interpretation of past and future exospheric measurements, such as those of LADEE on the Moon and BepiColombo on the planet Mercury.

8 Conclusions

8.1 Illumination Within Lunar PSRs

In Chapter 3, a survey of the primary illumination sources reaching the permanently shadowed regions of the Moon is detailed. We conclude that with respect to the overall magnitude, scattered sunlight is the largest source of illumination to reach the PSRs within the visible and IR regimes, and is a considerable source of FUV photons as well – exceeding the flux emanating from IPM/starlight within low latitude and high d/D craters. The enhanced FUV flux incident on the permanently shadowed crater floors suggests a higher rate of photodesorption than previously thought, as former estimations were made on the basis of IPM/starlight alone. This finding suggests enhanced photodesorption and lower adsorption residence times for water molecules than previously suggested, and, furthermore, indicates that this rate fluctuates diurnally, seasonally and geographically owing to the variability of the incoming solar flux. The conclusions reached by Gladstone et al. (2012), therefore, may be overstated for two reasons. First, the IPM is not the only significant source of FUV photons to the

PSRs. As demonstrated in this work, FUV scattered solar photons are also appreciable, and may even surpass the background IPM in magnitude at certain times of the year within certain craters. In addition, however, maximum summer and winter PSR surface temperatures are typically greater than 35 K (Williams et al., 2019), and given that the photodesorption yield (H_2O photon^{-1}) is positively correlated with the ice temperature (Westley et al., 1995), enhanced photodesorption is expected for a majority of regions.

Temporal variation in scattered sunlight occurs across diurnal and seasonal timescales, with the seasonal variation enhanced for near-polar craters. Appreciable differences in the received scattered solar energy exists between different craters, with the variance maintained by a combination of crater geometry and latitude. With respect to spatial trends within individual PSR craters, we find that equator-facing PSR slopes receive only $\sim$60% of the scattered solar energy at visible and IR wavelengths relative to those oriented toward the pole while in the FUV the disparity is increased due to enhanced backscattering of regolith particles (Liu et al., 2018), with equator-facing slopes receiving only $\sim$40% of the total energy. This inequality is a result of the alignment of pole-facing, PSRs slopes with the predominantly equator-facing, sunlit topographic facets that are scattering light into the PSRs; this alignment allows pole-oriented PSR terrain to receive more direct scattered light rays.

The results from the illumination modelling are used to estimate the signal-to-noise ratios for a camera imaging the permanently shadowed crater floor. Reduced illumination in the FUV and a large angular dependence on the observed surface brightness present serious challenges for a vis/FUV frost-detection approach, and demonstrate the need for accurate photometric correction tools in conjunction with laboratory work to substantiate model results. The solar variability at Ly-α presents an added challenge for a vis/FUV filter pairing, as it necessitates an additional correctional factor. At the observational geometries encountered for in-situ imaging of PSRs, a camera operable in the visible, IR 1500 nm and 2000 nm may be an ideal configuration as it would enable water ice properties, namely grain size, to be more accurately retrieved than with a single IR filter pair. As well, given an enhanced upwelling flux from the surface, greater SNR can be achieved with a vis/IR-sensitive camera.

8.2 Exospheric Volatile Migration

In Chapter 5 we map the extent and distribution seasonally shadowed regions at the lunar poles in order to gauge their influence on the lateral transport of water at the polar regions. In both hemispheres, PSR concentration increases moving from low latitudes ($\pm 65^{\circ}$) toward the pole, a pattern that is consistent with broad-scale trends of the putative water ice deposits observed from orbit (Feldman et al., 2000; Hayne et al., 2015; Li & Milliken, 2017). While temperature is likely the dominant parameter controlling the overall stability (and therefore distribution) of water ice on the surface (Fisher et al., 2017; Hayne et al., 2015; Vasavada, Paige, & Wood, 1999), the ability of water to reach high-latitudes where stability is enhanced may have important implications for the long-term evolution of polar volatile abundance and distribution.

In addition, we find that the northern hemisphere PSRs accumulate more water per unit area than those in the south, a disparity which is especially prominent beyond 85°. The north/south asymmetry arises from differences in the poleward migration of water between the two hemispheres, which in turn is a consequence of their unique PSR size-frequency distributions and the efficiency of PSR capture at high latitudes. While it has been shown that a hemispheric asymmetry can be caused by shifting the source of water to either side of the equator (Crider & Vondrak, 2000; Moores, 2016; Schorghofer, 2014), the model results shown here suggest that, even for a uniformly distributed source of lunar water, asymmetries in concentration between northern and southern hemisphere PSRs are found due to underlying differences in their ability to capture water.

Our model reveals that for a continual source of water, the growth and decay of shadow at the polar regions gives rise to a variation in the polar surface H_2O density. A seasonal lag is observed due to polar retention of seasonally trapped water, where the concentration of cold-trapped water peaks near the hemispheric vernal equinox – offset 2-3 lunations from the solstice where the seasonal trapping area is most expansive. Seasonal variation should occur on other airless bodies in the solar system with non-zero axial tilt such as Ceres, where in fact the variation may be even more pronounced given its current $\sim 4°$ obliquity (Schorghofer et al., 2017).

Chapter 6 extends this work and examines the lateral transport of other cometary volatiles on the Moon, including CO_2, CO, NH_3, SO_2 and H_2S and CH_4. We use Diviner thermal IR temperature to constrain the regions within PSRs where these volatiles may be thermodynamically stable over long timescales. We find that the south polar region contains up to 309 km^{-2}, 21 km^{-2} and 16 km^{-2} of cold trapping area for NH_3, SO_2 and CO_2, respectively, while the north pole contains only 52 km^{-2}, 3 km^{-2} and 2 km^{-2}.

The model is used to quantify the annual average infall rate of H_2O, CO_2 and CH_4 at the polar regions. Due to its relatively long lifetime against photolysis, CO_2 is shown to have the largest infall rate of the species examined, where surface concentrations near the poles exceed 2000γ; H_2O and CH_4 are photolyzed more easily and have lower infall rates, in the range of 200-400γ. Using estimated meteoritic supply rates as well as thermal and non-thermal loss rates, we show that net deposition of CO_2 and H_2O may be ongoing process within some of the coldest PSR locations. Assuming the meteoritic supply rate to be constant over time, we calculate that up to 1.5×10^{10} g of meteoritic CO_2 would be trapped over a 2 billion year timescale, most of which would reside at the lunar south pole due to the lower temperatures (see Figure 6.2). With enhanced cold trapping area, up to 1.1×10^{13} g of H_2O would have been trapped at the poles across the same time interval.

Finally, Chapter 7 investigates the influence of micro-scale roughness on the exospheric velocity distributions. We show that roughness effects at the exobase produce a non-uniform vertical velocity distribution and a barometric atmosphere. As a result, relative to a smooth surface, larger scale heights are expected for a rough exobase. These results can help to inform future exospheric measurements, such as those of LADEE on the Moon and BepiColombo on the planet Mercury.

8.3 Future Work

There are number of ways in which the work detailed here can be advanced. One such way is to further examine the H_2O photodesorption due to downwelling, high energy UV photons. As noted earlier, the discovery that scattered sunlight contributes a relatively significant flux of UV photons to the lunar PSRs (Chapter 3) has implications for the erosional rate (and thus lifetime) of surface-exposed ices. Laboratory investigations of FUV photodesorption of H_2O, CO and CO_2 ices have been conducted by Öberg et al. (2009). The yield curves, along with their temperature dependencies, can be used in conjunction with the FUV fluxes derived in this work to constrain the time-averaged rate at which adsorbed molecules are removed from surface grains. This work can ultimately determine the significance of this loss mechanism relative to others that have been identified, such as plasma sputtering, impact vaporization and meteoritic gardening.

In addition, the work reported in Chapter 7 can be further advanced through more accurate modeling of the thermal environment at micro scales, namely by including lateral heat conduction in the thermal model. Doing so will refine the estimations of the upwelling vertical velocity distributions and, in turn, the vertical density profiles. As well, future work in this area will examine how the velocity distribution changes as the thermal accommodation coefficient is varied between 0 (perfectly elastic collisions) and 1 (perfectly diffuse emission).

Bibliography

Acton Jr, C. H. (1996). Ancillary data services of nasa's navigation and ancillary information facility. *Planetary and Space Science*, *44*(1), 65–70.

Andreas, E. L. (2007). New estimates for the sublimation rate for ice on the moon. *Icarus*, *186*(1), 24–30.

Araki, H, Tazawa, S, Noda, H, Ishihara, Y, Goossens, S, Sasaki, S, Kawano, N, Kamiya, I, Otake, H, Oberst, J, Et al. (2009). Lunar global shape and polar topography derived from kaguya-lalt laser altimetry. *Science*, *323*(5916), 897–900.

Armand, G. (1977). Classical theory of desorption rate velocity distribution of desorbed atoms; possibility of a compensation effect. *Surface Science*, *66*(1), 321–345.

Arnold, J. R. (1979). Ice in the lunar polar regions. *Journal of Geophysical Research: Solid Earth*, *84*(B10), 5659–5668.

Bandfield, J. L., Hayne, P. O., Williams, J.-P., Greenhagen, B. T., & Paige, D. A. (2015). Lunar surface roughness derived from lro diviner radiometer observations. *Icarus*, *248*, 357–372.

Barker, M., Sun, X, Mazarico, E, Neumann, G., Zuber, M., & Smith, D. (2016). Lunar phase function at 1064 nm from Lunar Orbiter Laser Altimeter passive and active radiometry. *Icarus*, *273*, 96–113.

Benna, M, Hurley, D., Stubbs, T., Mahaffy, P., & Elphic, R. (2019). Lunar soil hydration constrained by exospheric water liberated by meteoroid impacts. *Nature Geoscience*, *12*(5), 333–338.

Benna, M, Mahaffy, P., & Hodges, R. (2014). Early results from exospheric observations by the neutral mass spectrometer (NMS), In *Lunar and planetary science conference*.

Bertaux, J., Kyrölä, E, Quémerais, E, Pellinen, R, Lallement, R, Schmidt, W, Berthé, M, Dimarellis, E, Goutail, J., Taulemesse, C, Et al. (1995). Swan: A study of solar wind anisotropies on SOHO with lyman alpha sky mapping, In *The soho mission*. Springer.

Binder, A. B. (1998). Lunar prospector: Overview. *Science*, *281*(5382), 1475–1476.

Bockelée-Morvan, D, & Biver, N. (2017). The composition of cometary ices. *Philosophical Transactions of the Royal Society A: Mathematical, Physical and Engineering Sciences*, *375*(2097), 20160252.

Bohren, C. F., & Huffman, D. R. (2008). *Absorption and scattering of light by small particles*. John Wiley & Sons.

Bussey, D. B. J., Fristad, K. E., Schenk, P. M., Robinson, M. S., & Spudis, P. D. (2005). Planetary science: Constant illumination at the lunar north pole. *Nature*, *434*(7035), 842.

Bussey, D. B. J., Spudis, P. D., & Robinson, M. S. (1999). Illumination conditions at the lunar south pole. *Geophysical Research Letters*, *26*(9), 1187–1190.

Butler, B. J. (1997). The migration of volatiles on the surfaces of Mercury and the Moon. *Journal of Geophysical Research: Planets*, *102*(E8), 19283–19291.

Cai, Y., & Fa, W. (2020). Meter-scale topographic roughness of the moon: The effect of small impact craters. *Journal of Geophysical Research: Planets*, *125*(8), e2020JE006429.

Carrier, W. D. (1973). Lunar soil grain size distribution. *The moon*, *6*(3-4), 250–263.

Chabot, N. L., Shread, E. E., & Harmon, J. K. (2018). Investigating mercury's south polar deposits: Arecibo radar observations and high-resolution determination of illumination conditions. *Journal of Geophysical Research: Planets*, *123*(2), 666–681.

Chin, G., Brylow, S., Foote, M., Garvin, J., Kasper, J., Keller, J., Litvak, M., Mitrofanov, I., Paige, D., Raney, K., Et al. (2007). Lunar Reconnaissance Orbiter overview: The instrument suite and mission. *Space Science Reviews*, *129*(4), 391–419.

Cintala, M. J. (1992). Impact-induced thermal effects in the lunar and mercurian regoliths. *Journal of Geophysical Research: Planets*, *97*(E1), 947–973.

Cisneros, E., & the LROC Team. Lroc permanently shadowed regions atlas.

Clark, R. N. (2009). Detection of adsorbed water and hydroxyl on the Moon. *Science*, *326*(5952), 562–564.

Cohen, B. A., Hayne, P. O., Greenhagen, B. T., & Paige, D. A. (2015). Lunar flashlight: Exploration and science at the moon with a 6u cubesat. *AGUFM*, *2015*, EP52B–07.

Colaprete, A., Andrews, D., Bluethmann, W., Elphic, R. C., Bussey, B., Trimble, J., Zacny, K., & Captain, J. E. (2019). An overview of the volatiles investigating polar exploration rover (viper) mission. *AGUFM*, *2019*, P34B–03.

Colaprete, A., Schultz, P., Heldmann, J., Wooden, D., Shirley, M., Ennico, K., Hermalyn, B., Marshall, W., Ricco, A., Elphic, R. C., Et al. (2010). Detection of water in the LCROSS ejecta plume. *science*, *330*(6003), 463–468.

Crank, J., & Nicolson, P. (1947). A practical method for numerical evaluation of solutions of partial differential equations of the heat-conduction type, In *Mathematical proceedings of the cambridge philosophical society*. Cambridge University Press.

Crider, D. H., & Vondrak, R. (2002). Hydrogen migration to the lunar poles by solar wind bombardment of the Moon. *Advances in Space Research*, *30*(8), 1869–1874.

Crider, D. H., & Vondrak, R. R. (2000). The solar wind as a possible source of lunar polar hydrogen deposits. *Journal of Geophysical Research: Planets*, *105*(E11), 26773–26782.

Crovisier, J. (1989). The photodissociation of water in cometary atmospheres. *Astronomy and Astrophysics*, *213*, 459–464.

Deutsch, A. N., Chabot, N. L., Mazarico, E., Ernst, C. M., Head, J. W., Neumann, G. A., & Solomon, S. C. (2016). Comparison of areas in shadow from imaging and altimetry in the north polar region of mercury and implications for polar ice deposits. *Icarus*, *280*, 158–171.

Farrell, W., Hurley, D., Poston, M., Hayne, P., Szalay, J., & McLain, J. (2019). The young age of the lamp-observed frost in lunar polar cold traps. *Geophysical Research Letters*, *46*(15), 8680–8688.

Feldman, W., Barraclough, B., Fuller, K., Lawrence, D., Maurice, S, Miller, M., Prettyman, T., & Binder, A. (1999). The Lunar Prospector gamma-ray and neutron spectrometers. *Nuclear Instruments and Methods in Physics Research Section A: Accelerators, Spectrometers, Detectors and Associated Equipment*, *422*(1-3), 562–566.

Feldman, W., Lawrence, D., Elphic, R., Barraclough, B., Maurice, S, Genetay, I, & Binder, A. (2000). Polar hydrogen deposits on the Moon. *Journal of Geophysical Research: Planets*, *105*(E2), 4175–4195.

Feldman, W., Maurice, S, Binder, A., Barraclough, B., Elphic, R., & Lawrence, D. (1998). Fluxes of fast and epithermal neutrons from Lunar Prospector: Evidence for water ice at the lunar poles. *Science*, *281*(5382), 1496–1500.

Feldman, W. C., Maurice, S., Lawrence, D. J., Little, R. C., Lawson, S., Gasnault, O, Wiens, R. C., Barraclough, B. L., Elphic, R. C., Prettyman, T. H., Et al. (2001). Evidence for water ice near the lunar poles. *Journal of Geophysical Research: Planets*, *106*(E10), 23231–23251.

Fisher, E. A., Lucey, P. G., Lemelin, M., Greenhagen, B. T., Siegler, M. A., Mazarico, E., Aharonson, O., Williams, J.-P., Hayne, P. O., Neumann, G. A., Et al. (2017). Evidence for surface water ice in the lunar polar regions using reflectance measurements from the Lunar Orbiter Laser Altimeter and temperature measurements from the Diviner Lunar Radiometer Experiment. *Icarus*, *292*, 74–85.

Gibson, E., & Sommer, M. (1986). Laser microprobe study of cosmic dust (idps) and potential source materials, In *Lunar and planetary science conference*.

Gibson Jr, E. K. (1992). Volatiles in interplanetary dust particles: A review. *Journal of Geophysical Research: Planets*, *97*(E3), 3865–3875.

Gladstone, G. R., Retherford, K. D., Egan, A. F., Kaufmann, D. E., Miles, P. F., Parker, J. W., Horvath, D., Rojas, P. M., Versteeg, M. H., Davis, M. W., Et al. (2012). Far-ultraviolet reflectance properties of the Moon's permanently shadowed regions. *Journal of Geophysical Research: Planets*, *117*(E12).

Gladstone, G. R., Stern, S. A., Retherford, K. D., Black, R. K., Slater, D. C., Davis, M. W., Versteeg, M. H., Persson, K. B., Parker, J. W., Kaufmann, D. E., Et al. (2010). Lamp: The Lyman Alpha Mapping Project on NASA's Lunar Reconnaissance Orbiter mission. *Space Science Reviews*, *150*(1-4), 161–181.

Gläser, P, Oberst, J, Neumann, G., Mazarico, E, Speyerer, E., & Robinson, M. (2018). Illumination conditions at the lunar poles: Implications for future exploration. *Planetary and Space Science*, *162*, 170–178.

Gläser, P, Scholten, F, De Rosa, D, Figuera, R. M., Oberst, J, Mazarico, E, Neumann, G., & Robinson, M. (2014). Illumination conditions at the lunar south pole using high resolution digital terrain models from LOLA. *Icarus*, *243*, 78–90.

Glenar, D. A., Stubbs, T. J., Schwieterman, E. W., Robinson, T. D., & Livengood, T. A. (2019). Earthshine as an illumination source at the Moon. *Icarus*, *321*, 841–856.

Godin, P. J., Kloos, J. L., Seguin, A., & Moores, J. E. (2020). Laboratory investigations of lunar ice imaging in permanently shadowed regions using reflected starlight. *Acta Astronautica*.

Hapke, B. (2012). *Theory of reflectance and emittance spectroscopy*. Cambridge university press.

Hapke, B., Denevi, B., Sato, H., Braden, S., & Robinson, M. (2012). The wavelength dependence of the lunar phase curve as seen by the Lunar Reconnaissance Orbiter wide-angle camera. *Journal of Geophysical Research: Planets*, *117*(E12).

Hapke, B., & Sato, H. (2016). The porosity of the upper lunar regolith. *Icarus*, *273*, 75–83.

Haruyama, J., Ohtake, M., Matsunaga, T., Morota, T., Honda, C., Yokota, Y., Pieters, C. M., Hara, S., Hioki, K., Saiki, K., Et al. (2008). Lack of exposed ice inside lunar south pole shackleton crater. *Science*, *322*(5903), 938–939.

Hayne, P. O., Aharonson, O., & Schörghofer, N. (2020). Micro cold traps on the moon. *arXiv preprint arXiv:2005.05369*.

Hayne, P. O., Hendrix, A., Sefton-Nash, E., Siegler, M. A., Lucey, P. G., Retherford, K. D., Williams, J.-P., Greenhagen, B. T., & Paige, D. A. (2015). Evidence for exposed water ice in the Moon's south polar regions from Lunar Reconnaissance Orbiter ultraviolet albedo and temperature measurements. *Icarus*, *255*, 58–69.

Hayne, P., Siegler, M., Paige, D., Lucey, P., & Fisher, E. (2019). Carbon dioxide frost at the poles of the moon: Thermal stability and observational evidence from the lunar reconnaissance orbiter. *LPI*, (2132), 2628.

Helfenstein, P., & Shepard, M. K. (1999). Submillimeter-scale topography of the lunar regolith. *Icarus*, *141*(1), 107–131.

Helfenstein, P., Veverka, J., & Hillier, J. (1997). The lunar opposition effect: A test of alternative models. *Icarus*, *128*(1), 2–14.

Hendrix, A. R., & Hansen, C. J. (2008). Ultraviolet observations of phoebe from the cassini uvis. *Icarus*, *193*(2), 323–333.

Hendrix, A. R., Hurley, D. M., Farrell, W. M., Greenhagen, B. T., Hayne, P. O., Retherford, K. D., Vilas, F., Cahill, J. T., Poston, M. J., & Liu, Y. (2019). Diurnally-migrating lunar water: Evidence from ultraviolet data. *Geophysical Research Letters*.

Hendrix, A. R., Retherford, K. D., Randall Gladstone, G, Hurley, D. M., Feldman, P. D., Egan, A. F., Kaufmann, D. E., Miles, P. F., Parker, J. W., Horvath, D., Et al. (2012). The lunar far-UV albedo: Indicator of hydration and weathering. *Journal of Geophysical Research: Planets*, *117*(E12).

Hillier, J. K., Buratti, B. J., & Hill, K. (1999). Multispectral photometry of the Moon and absolute calibration of the Clementine UV/Vis camera. *Icarus*, *141*(2), 205–225.

Hodges, R. R. (2002). Ice in the lunar polar regions revisited. *Journal of Geophysical Research: Planets*, *107*(E2), 6–1.

Hodges Jr, R. R. (2016). Methane in the lunar exosphere: Implications for solar wind carbon escape. *Geophysical Research Letters*, *43*(13), 6742–6748.

Hodges Jr, R. R. (2018). Semiannual oscillation of the lunar exosphere: Implications for water and polar ice. *Geophysical Research Letters*, *45*(15), 7409–7416.

Hodges Jr, R. R., & Mahaffy, P. R. (2016). Synodic and semiannual oscillations of argon-40 in the lunar exosphere. *Geophysical Research Letters*, *43*(1), 22–27.

Hodges Jr, R. (1976). The escape of solar-wind carbon from the moon, In *Lunar and planetary science conference proceedings*.

Hoffman, J., & Hodges, R. (1975). Molecular gas species in the lunar atmosphere. *The Moon*, *14*(1), 159–167.

Horanyi, M., & Szalay, J. (2017). The effects of interplanetary dust impacts on the accumulation of volatiles in the lunar permanently shadowed regions, In *Dps*.

Huebner, W. F., Keady, J. J., & Lyon, S. (1992). Solar photo rates for planetary atmospheres and atmospheric pollutants, In *Solar photo rates for planetary atmospheres and atmospheric pollutants*. Springer.

Hurley, D. M., Lawrence, D. J., Bussey, D. B. J., Vondrak, R. R., Elphic, R. C., & Gladstone, G. R. (2012). Two-dimensional distribution of volatiles in the lunar regolith from space weathering simulations. *Geophysical research letters*, *39*(9).

Hurley, D. M., Sarantos, M., Grava, C., Williams, J.-P., Retherford, K. D., Siegler, M., Greenhagen, B., & Paige, D. (2015). An analytic function of lunar surface temperature for exospheric modeling. *Icarus*, *255*, 159–163.

Jacobs, T. D., Junge, T., & Pastewka, L. (2017). Quantitative characterization of surface topography using spectral analysis. *Surface Topography: Metrology and Properties*, *5*(1), 013001.

Jones, B. M., Aleksandrov, A., Hibbitts, K, Dyar, M., & Orlando, T. M. (2018). Solar wind-induced water cycle on the moon. *Geophysical Research Letters*, *45*(20), 10–959.

Kennelly, E. J., Price, S. D., Kraemer, K. E., & Aschbrenner, R. (2010). Calibration against the Moon i: A disk-resolved lunar model for absolute reflectance calibration. *Icarus*, *210*(1), 14–36.

Killen, R. M., & Ip, W.-H. (1999). The surface-bounded atmospheres of mercury and the moon. *Reviews of Geophysics*, *37*(3), 361–406.

Kloos, J. L., & Moores, J. E. (2019). Mapping the limited extent of earthshine within lunar PSRs. *Research Notes of the AAS*, *3*(9), 127.

Kloos, J. L., Moores, J. E., Godin, P., & Cloutis, E. (2020). Illumination conditions within permanently shadowed regions of the moon: Implications for in situ passive remote sensing. *Acta Astronautica*, *178*, 432–451.

Kloos, J. L., Moores, J. E., Sangha, J., Nguyen, T. G., & Schorghofer, N. (2019). The temporal and geographic extent of seasonal cold trapping on the moon. *Journal of Geophysical Research: Planets*, *124*(7), 1935–1944.

Koeber, S., Robinson, M., & Speyerer, E. (2014). Lroc observations of permanently shadowed regions on the moon, In *Lunar and planetary science conference*.

Kruzelecky, R., Murzionak, P., Lavoie, J., Sinclair, I., Schinn, G., Underwood, C., Gao, Y., Bridges, C., Armellin, R., Luccafabris, A., Et al. (2018). VMMO Lunar Volatile and Mineralogy Mapping Orbiter. 48th International Conference on Environmental Systems.

Langmuir, I. (1916). The evaporation, condensation and reflection of molecules and the mechanism of adsorption. *Physical Review*, *8*(2), 149.

Lawrence, D. J. (2017). A tale of two poles: Toward understanding the presence, distribution, and origin of volatiles at the polar regions of the Moon and Mercury. *Journal of Geophysical Research: Planets*, *122*(1), 21–52.

Lemelin, M, Lucey, P., Neumann, G., Mazarico, E., Barker, M., Kakazu, A, Trang, D, Smith, D., & Zuber, M. (2016). Improved calibration of reflectance data from the lro lunar orbiter laser altimeter (lola) and implications for space weathering. *Icarus*, *273*, 315–328.

Li, S., Lucey, P. G., Milliken, R. E., Hayne, P. O., Fisher, E., Williams, J.-P., Hurley, D. M., & Elphic, R. C. (2018). Direct evidence of surface exposed water ice in the lunar polar regions. *Proceedings of the National Academy of Sciences*, 201802345.

Li, S., & Milliken, R. E. (2017). Water on the surface of the Moon as seen by the Moon Mineralogy Mapper: Distribution, abundance, and origins. *Science advances*, *3*(9), e1701471.

Liu, Y, Retherford, K., Greathouse, T., Raut, U., Mandt, K., Hendrix, A., Cahill, J., Gladstone, G., Grava, C, Egan, A., Et al. (2018). The far ultraviolet wavelength dependence of the lunar phase curve as seen by LRO LAMP. *Journal of Geophysical Research: Planets*, *123*(10), 2550–2563.

Livengood, T., Chin, G, Sagdeev, R., Mitrofanov, I., Boynton, W. V., Evans, L., Litvak, M., McClanahan, T., Sanin, A., Starr, R., Et al. (2015). Moonshine:

Diurnally varying hydration through natural distillation on the moon, detected by the lunar exploration neutron detector (lend). *Icarus*, *255*, 100–115.

Lucey, P., Neumann, G., Riner, M., Mazarico, E, Smith, D., Zuber, M., Paige, D., Bussey, D., Cahill, J., McGovern, A, Et al. (2014). The global albedo of the moon at 1064 nm from lola. *Journal of Geophysical Research: Planets*, *119*(7), 1665–1679.

Manka, R., & Michel, F. (1970). Lunar atmosphere as a source of argon-40 and other lunar surface elements. *Science*, *169*(3942), 278–280.

Margot, J.-L., Campbell, D. B., Jurgens, R. F., & Slade, M. (1999). Topography of the lunar poles from radar interferometry: A survey of cold trap locations. *Science*, *284*(5420), 1658–1660.

Mazarico, E, Neumann, G., Smith, D., Zuber, M., & Torrence, M. (2011). Illumination conditions of the lunar polar regions using LOLA topography. *Icarus*, *211*(2), 1066–1081.

Mazarico, E., Barker, M. K., & Nicholas, J. B. (2018). Advanced illumination modeling for data analysis and calibration. application to the moon. *Advances in Space Research*, *62*(11), 3214–3228.

McClintock, W. E., Rottman, G. J., & Woods, T. N. (2000). Solar Stellar Irradiance Comparison Experiment II (SOLSTICE II) for the NASA Earth Observing System's Solar Radiation and Climate Experiment mission (W. L. Barnes, Ed.). In W. L. Barnes (Ed.), *Earth observing systems v*, SPIE. International Society for Optics and Photonics. https://doi.org/10.1117/12.494220

McCord, T., Taylor, L., Combe, J.-P., Kramer, G, Pieters, C., Sunshine, J., & Clark, R. (2011). Sources and physical processes responsible for oh/h2o in the lunar soil as revealed by the moon mineralogy mapper (m3). *Journal of Geophysical Research: Planets*, *116*(E6).

McGovern, J. A., Bussey, D. B., Greenhagen, B. T., Paige, D. A., Cahill, J. T., & Spudis, P. D. (2013). Mapping and characterization of non-polar permanent shadows on the lunar surface. *Icarus*, *223*(1), 566–581.

Mellinger, A. (2009). A color all-sky panorama image of the Milky Way. *Publications of the Astronomical Society of the Pacific*, *121*(885), 1180.

Metzger, P., Anderson, S, & Colaprete, A. (2014). Experiments indicate regolith is looser in the lunar polar regions than at the lunar landing sites. *Journal of Aerospace Engineering*.

Mitchell, E., Raut, U, Fulvio, D, Schaible, M., Dukes, C., & Baragiola, R. (2013). Ultraviolet photodesorption as a driver of water migration on the lunar surface. *Planetary and Space Science*, *89*, 42–46.

Mitchell, J., Lawrence, S., Robinson, M., Speyerer, E., & Denevi, B. (2018). Using complementary remote sensing techniques to assess the presence of volatiles at the lunar north pole. *Planetary and Space Science*, *162*, 133–147.

Mitrofanov, I, Litvak, M, Sanin, A, Malakhov, A, Golovin, D, Boynton, W, Droege, G, Chin, G, Evans, L, Harshman, K, Et al. (2012). Testing polar spots of water-rich permafrost on the moon: LEND observations onboard LRO. *Journal of Geophysical Research: Planets*, *117*(E12).

Mitrofanov, I. G., Sanin, A. B., Boynton, W., Chin, G, Garvin, J., Golovin, D, Evans, L., Harshman, K, Kozyrev, A., Litvak, M., Et al. (2010). Hydrogen mapping of the lunar south pole using the LRO neutron detector experiment LEND. *science*, *330*(6003), 483–486.

Moores, J. E. (2016). Lunar water migration in the interval between large impacts: Heterogeneous delivery to permanently shadowed regions, fractionation, and diffusive barriers. *Journal of Geophysical Research: Planets*, *121*(1), 46–60.

Morgan, T., & Shemansky, D. (1991). Limits to the lunar atmosphere. *Journal of Geophysical Research: Space Physics*, *96*(A2), 1351–1367.

Morgan, T., Zook, H., & Potter, A. (1989). Production of sodium vapor from exposed regolith in the inner solar system, In *Lunar and planetary science conference proceedings*.

Needham, D. H., & Kring, D. A. (2017). Lunar volcanism produced a transient atmosphere around the ancient moon. *Earth and Planetary Science Letters*, *478*, 175–178.

Noda, H, Araki, H, Goossens, S, Ishihara, Y, Matsumoto, K, Tazawa, S, Kawano, N, & Sasaki, S. (2008). Illumination conditions at the lunar polar regions by kaguya (selene) laser altimeter. *Geophysical research letters*, *35*(24).

Nozette, S, Lichtenberg, C., Spudis, P, Bonner, R, Ort, W, Malaret, E, Robinson, M, & Shoemaker, E. (1996). The Clementine bistatic radar experiment. *Science*, *274*(5292), 1495–1498.

Nozette, S., Rustan, P, Pleasance, L., Kordas, J., Lewis, I., Park, H., Priest, R., Horan, D., Regeon, P, Lichtenberg, C., Et al. (1994). The clementine mission to the moon: Scientific overview. *Science*, *266*(5192), 1835–1839.

Öberg, K. I., Linnartz, H., Visser, R., & Van Dishoeck, E. F. (2009). Photodesorption of ices. ii. H2O and D2O. *The Astrophysical Journal*, *693*(2), 1209.

Ohtake, M., Matsunaga, T., Yokota, Y., Yamamoto, S., Ogawa, Y., Morota, T., Honda, C., Haruyama, J., Kitazato, K., Takeda, H., Et al. (2010). Deriving the absolute reflectance of lunar surface using SELENE (Kaguya) multiband imager data. *Space science reviews*, *154*(1-4), 57–77.

Ong, L., Asphaug, E. I., Korycansky, D., & Coker, R. F. (2010). Volatile retention from cometary impacts on the moon. *Icarus*, *207*(2), 578–589.

Paige, D. A., Siegler, M. A., Zhang, J. A., Hayne, P. O., Foote, E. J., Bennett, K. A., Vasavada, A. R., Greenhagen, B. T., Schofield, J. T., McCleese, D. J., Et al. (2010). Diviner lunar radiometer observations of cold traps in the Moon's south polar region. *science*, *330*(6003), 479–482.

Pierazzo, E., & Chyba, C. F. (2006). Impact delivery of prebiotic organic matter to planetary surfaces, In *Comets and the origin and evolution of life*. Springer.

Pieters, C. M., Goswami, J., Clark, R., Annadurai, M, Boardman, J, Buratti, B, Combe, J.-P., Dyar, M., Green, R, Head, J., Et al. (2009). Character and spatial distribution of OH/H2O on the surface of the Moon seen by M3 on Chandrayaan-1. *science*, *326*(5952), 568–572.

Pieters, C. M., & Mustard, J. F. (1988). Exploration of crustal/mantle material for the earth and moon using reflectance spectroscopy. *Remote Sensing of Environment*, *24*(1), 151–178.

Pike, R. J. (1977). Size-dependence in the shape of fresh impact craters on the Moon, In *Impact and explosion cratering: Planetary and terrestrial implications*.

Pike, R. J. (1970). Some preliminary interpretations of lunar mass-wasting processes from apollo 10 photography. *NASA Special Publication*, *232*, 14.

Platz, T, Nathues, A, Schorghofer, N, Preusker, F., Mazarico, E, Schröder, S., Byrne, S, Kneissl, T, Schmedemann, N, Combe, J.-P., Et al. (2016). Surface water-ice deposits in the northern shadowed regions of ceres. *Nature Astronomy*, *1*(1), 1–6.

Pokornỳ, P., Sarantos, M., Janches, D., & Mazarico, E. (2020). Meteoroid bombardment of lunar poles. *The Astrophysical Journal*, *894*(2), 114.

Poston, M. J., Grieves, G. A., Aleksandrov, A. B., Hibbitts, C. A., Darby Dyar, M, & Orlando, T. M. (2013). Water interactions with micronized lunar surrogates jsc-1a and albite under ultra-high vacuum with application to lunar observations. *Journal of Geophysical Research: Planets*, *118*(1), 105–115.

Prem, P., Artemieva, N., Goldstein, D., Varghese, P., & Trafton, L. (2015). Transport of water in a transient impact-generated lunar atmosphere. *Icarus*, *255*, 148–158.

Prem, P., Goldstein, D., Varghese, P., & Trafton, L. (2018). The influence of surface roughness on volatile transport on the Moon. *Icarus*, *299*, 31–45.

Qiao, L., Ling, Z., Head, J. W., Ivanov, M. A., & Liu, B. (2019). Analyses of lunar orbiter laser altimeter 1,064-nm albedo in permanently shadowed regions of polar crater flat floors: Implications for surface water ice occurrence and future in situ exploration. *Earth and Space Science*, *6*(3), 467–488.

Raut, U, Karnes, P., Retherford, K., Davis, M., Liu, Y, Gladstone, G., Patrick, E., Greathouse, T. K., Hendrix, A., & Mokashi, P. (2018). Far-ultraviolet photometric response of Apollo soil 10084. *Journal of Geophysical Research: Planets*, *123*(5), 1221–1229.

Robinson, M., Brylow, S., Tschimmel, M, Humm, D, Lawrence, S., Thomas, P., Denevi, B., Bowman-Cisneros, E, Zerr, J, Ravine, M., Et al. (2010). Lunar reconnaissance orbiter camera (lroc) instrument overview. *Space science reviews*, *150*(1-4), 81–124.

Rosenburg, M., Aharonson, O., Head, J., Kreslavsky, M., Mazarico, E, Neumann, G. A., Smith, D. E., Torrence, M. H., & Zuber, M. T. (2011). Global surface slopes and roughness of the moon from the lunar orbiter laser altimeter. *Journal of Geophysical Research: Planets*, *116*(E2).

Rottman, G. J., Woods, T. N., & Sparn, T. P. (1993). Solar-stellar irradiance comparison experiment 1: 1. instrument design and operation. *Journal of Geophysical Research: Atmospheres*, *98*(D6), 10667–10677.

Rubanenko, L, Schorghofer, N, Greenhagen, B., & Paige, D. (2020). Equilibrium temperatures and directional emissivity of sunlit airless surfaces with applications to the moon. *Journal of Geophysical Research: Planets*, *125*(6), e2020JE006377.

Rubanenko, L., Venkatraman, J., & Paige, D. A. (2019). Thick ice deposits in shallow simple craters on the moon and mercury. *Nature Geoscience*, *12*(8), 597–601.

Sandford, S. A., & Allamandola, L. J. (1993). The condensation and vaporization behavior of ices containing so2, h2s, and co2: Implications for io. *Icarus*, *106*(2), 478–488.

Sanin, A., Mitrofanov, I., Litvak, M., Malakhov, A, Boynton, W., Chin, G, Droege, G, Evans, L., Garvin, J, Golovin, D., Et al. (2012). Testing lunar permanently shadowed regions for water ice: LEND results from LRO. *Journal of Geophysical Research: Planets*, *117*(E12).

Sato, H, Robinson, M., Hapke, B, Denevi, B., & Boyd, A. (2014). Resolved hapke parameter maps of the Moon. *Journal of Geophysical Research: Planets*, *119*(8), 1775–1805.

Schorghofer, N. (2014). Migration calculations for water in the exosphere of the Moon: Dusk-dawn asymmetry, heterogeneous trapping, and D/H fractionation. *Geophysical Research Letters*, *41*(14), 4888–4893.

Schorghofer, N. (2018). Thermodynamics of surface-bounded exospheres: Divergent near-surface density. *arXiv preprint arXiv:1810.00165*.

Schorghofer, N., & Aharonson, O. (2014). The lunar thermal ice pump. *The Astrophysical Journal*, *788*(2), 169.

Schorghofer, N., Byrne, S., Landis, M. E., Mazarico, E., Prettyman, T. H., Schmidt, B. E., Villarreal, M. N., Castillo-Rogez, J., Raymond, C. A., & Russell, C. T. (2017). The putative Cerean exosphere. *The Astrophysical Journal*, *850*(1), 85.

Schorghofer, N., Lucey, P., & Williams, J.-P. (2017). Theoretical time variability of mobile water on the moon and its geographic pattern. *Icarus*, *298*, 111–116.

Schorghofer, N., Mazarico, E., Platz, T., Preusker, F., Schröder, S. E., Raymond, C. A., & Russell, C. T. (2016). The permanently shadowed regions of dwarf planet ceres. *Geophysical Research Letters*, *43*(13), 6783–6789.

Schorghofer, N., & Taylor, G. J. (2007). Subsurface migration of H2O at lunar cold traps. *Journal of Geophysical Research: Planets*, *112*(E2).

Shepard, M. K., & Campbell, B. A. (1998). Shadows on a planetary surface and implications for photometric roughness. *Icarus*.

Shkuratov, Y., Starukhina, L., Hoffmann, H., & Arnold, G. (1999). A model of spectral albedo of particulate surfaces: Implications for optical properties of the Moon. *Icarus*, *137*(2), 235–246.

Shoemaker, E., Robinson, M., & Eliason, E. (1994). The south pole region of the Moon as seen by Clementine. *Science*, *266*(5192), 1851–1854.

Siegler, M., Miller, R., Keane, J., Laneuville, M, Paige, D., Matsuyama, I, Lawrence, D., Crotts, A, & Poston, M. (2016). Lunar true polar wander inferred from polar hydrogen. *Nature*, *531*(7595), 480.

Siegler, M., Paige, D., Williams, J.-P., & Bills, B. (2015). Evolution of lunar polar ice stability. *Icarus*, *255*, 78–87.

Slade, M. A., Butler, B. J., & Muhleman, D. O. (1992). Mercury radar imaging: Evidence for polar ice. *Science*, *258*(5082), 635–640.

Smith, B. (1967). Geometrical shadowing of a random rough surface. *IEEE transactions on antennas and propagation*, *15*(5), 668–671.

Smith, D. E., Zuber, M. T., Neumann, G. A., Lemoine, F. G., Mazarico, E., Torrence, M. H., McGarry, J. F., Rowlands, D. D., Head, J. W., Duxbury, T. H., Et al. (2010). Initial observations from the Lunar Orbiter Laser Altimeter (LOLA). *Geophysical Research Letters*, *37*(18).

Smith, G. R., Shemansky, D., Broadfoot, A. L., & Wallace, L. (1978). Monte carlo modeling of exospheric bodies: Mercury. *Journal of Geophysical Research: Space Physics*, *83*(A8), 3783–3790.

Speyerer, E. J., & Robinson, M. S. (2013). Persistently illuminated regions at the lunar poles: Ideal sites for future exploration. *Icarus*, *222*(1), 122–136.

Spudis, P., Bussey, D., Baloga, S., Cahill, J., Glaze, L., Patterson, G., Raney, R., Thompson, T., Thomson, B., & Ustinov, E. (2013). Evidence for water ice on the Moon: Results for anomalous polar craters from the LRO Mini-RF imaging radar. *Journal of Geophysical Research: Planets*, *118*(10), 2016–2029.

Stacy, N., Campbell, D., & Ford, P. (1997). Arecibo radar mapping of the lunar poles: A search for ice deposits. *Science*, *276*(5318), 1527–1530.

Stern, S. A. (1999). The lunar atmosphere: History, status, current problems, and context. *Reviews of Geophysics*, *37*(4), 453–491.

Stewart, B. D., Pierazzo, E., Goldstein, D. B., Varghese, P. L., & Trafton, L. M. (2011). Simulations of a comet impact on the moon and associated ice deposition in polar cold traps. *Icarus*, *215*(1), 1–16.

Sunshine, J. M., Farnham, T. L., Feaga, L. M., Groussin, O., Merlin, F., Milliken, R. E., & A'Hearn, M. F. (2009). Temporal and spatial variability of lunar hydration as observed by the Deep Impact spacecraft. *Science*, *326*(5952), 565–568.

Taylor, S. (1975). Lunar science: A post-apollo view(book). *New York, Pergamon Press, Inc., 1975. 390 p.*

Ulrich, G. E., Hodges, C. A., & Muehlberger, W. R. (1981). *Geology of the apollo 16 area, central lunar highlands*. US Government Printing Office.

Urey, H. C. (1952). *The planets: Their origin and development.* Yale Univ. Press.

Vasavada, A. R., Paige, D. A., & Wood, S. E. (1999). Near-surface temperatures on Mercury and the Moon and the stability of polar ice deposits. *Icarus*, *141*(2), 179–193.

Ward, W. R. (1975). Past orientation of the lunar spin axis. *Science*, *189*(4200), 377–379.

Warren, S. G., & Brandt, R. E. (2008). Optical constants of ice from the ultraviolet to the microwave: A revised compilation. *Journal of Geophysical Research: Atmospheres*, *113*(D14).

Watson, K., Murray, B. C., & Brown, H. (1961). The behavior of volatiles on the lunar surface. *Journal of Geophysical Research*, *66*(9), 3033–3045.

Westley, M., Baragiola, R., Johnson, R., & Baratta, G. (1995). Ultraviolet photodesorption from water ice. *Planetary and Space Science*, *43*(10-11), 1311–1315.

Williams, J.-P., Greenhagen, B., Paige, D., Schorghofer, N, Sefton-Nash, E, Hayne, P., Lucey, P., Siegler, M., & Aye, K. M. (2019). Seasonal polar temperatures on the moon. *Journal of Geophysical Research: Planets*, *124*(10), 2505–2521.

Williams, J.-P., Paige, D., Greenhagen, B., & Sefton-Nash, E. (2017). The global surface temperatures of the Moon as measured by the Diviner Lunar Radiometer Experiment. *Icarus*, *283*, 300–325.

Williams, J., Boggs, D., & Folkner, W. (2008). De421 lunar orbit, physical librations, and surface coordinates. *Rep. IOM 335-JW, DB, WF-20080314*, *1*.

Wiscombe, W. J., & Warren, S. G. (1980). A model for the spectral albedo of snow. i: Pure snow. *Journal of the Atmospheric Sciences*, *37*(12), 2712–2733.

Zhang, J. A., & Paige, D. A. (2009). Cold-trapped organic compounds at the poles of the moon and mercury: Implications for origins. *Geophysical Research Letters*, *36*(16).

Zuber, M. T., Head, J. W., Smith, D. E., Neumann, G. A., Mazarico, E., Torrence, M. H., Aharonson, O., Tye, A. R., Fassett, C. I., Rosenburg, M. A., Et al. (2012). Constraints on the volatile distribution within shackleton crater at the lunar south pole. *Nature*, *486*(7403), 378–381.

Appendices

A | PSR Crater Summary

Table A.1: PSR craters for which scattered sunlight is modeled (Chapter 3).

Crater	[a]Latitude (deg)	[a]Longitude (deg)	[a]Diameter (km)	d/D	[b]PSR Area (km^2)
		Northern Hemisphere			
Bosch	86.8 N	133.5 E	19.6	0.13	28
Erlanger	87.0 N	28.6 E	10.9	0.20	57
Gibiger	86.1 N	37.1 E	21.1	0.12	118
Gore	86.2 N	62.3 W	9.4	0.20	31
Grignard	84.5 N	75.8 W	13.0	0.20	48
Hermite A	87.9 N	51.0 W	19.9	0.13	211
Hinshelwood	89.4 N	51.9 W	13.4	0.20	59
Houssay	83.1 N	98.5 E	31.4	0.09	118
Lenard	85.2 N	109.7 W	47.7	0.07	287
Lovelace	82.1 N	109.5 W	57.1	0.06	347
Lovelace E	82.0 N	96.8 W	21.7	0.12	140
Main L	81.4 N	22.7 E	14.3	0.20	86
Mouchez M	80.3 N	50.1 W	17.3	0.14	107
Nansen A	82.8 N	65.0 E	44.9	0.07	133
Nansen F	85.0 N	62.4 E	61.6	0.06	334
Plaskett S	81.0 N	150.6 E	16.8	0.15	107
Plaskett U	82.4 N	162.3 E	15.9	0.15	93
Plaskett V	82.2 N	120.9 E	49.1	0.07	123
Rozhdestvenskiy K	82.2 N	147.0 W	42.9	0.08	254
Rozhdestvenskiy N	84.0 N	156.5 W	9.2	0.20	29
Rozhdestvenskiy U	84.9 N	152.1 E	44.1	0.07	388
Sylvester	82.7 N	81.2 W	59.3	0.06	319
Sylvester N	82.4 N	68.7 W	20.0	0.13	153
Whipple	89.1 N	120.0 E	14.5	0.20	87
		Southern Hemisphere			
Amundsen	84.4 S	83.1 E	103.4	0.04	670
Braude	81.8 S	158.9 E	11.3	0.20	44
Cabeus	85.3 S	42.1 W	100.6	0.04	651
Cabeus B	82.3 S	54.6 W	59.6	0.06	368
de Gerlache	88.5 S	88.3 W	32.7	0.09	239
Demonax B	81.5 S	72.0 E	23.2	0.12	89
Faustini	87.2 S	84.3 E	42.5	0.08	660
Haworth	87.5 S	5.2 W	51.4	0.07	1010
Ibn Bajja	86.3 S	75.0 W	12.0	0.20	58
Idel'son L	84.0 S	118.6 E	28.0	0.10	324
Kocher	84.5 S	134.0 W	24.0	0.11	75
Kuhn	84.5 S	152.5 W	16.6	0.15	71
Laveran	81.8 S	159.8 W	12.5	0.20	48
Malapert	85.0 S	11.4 E	72.4	0.05	292
Nobile	85.3 S	53.3 E	79.3	0.05	589
Scott E	81.2 S	35.7 E	29.2	0.10	165
Shackleton	89.7 S	129.8 E	20.9	0.12	233
Shoemaker	88.1 S	45.9 E	51.8	0.07	1070
Svedberg	81.7 S	65.2 E	15.3	0.15	81
Sverdrup	88.3 S	153.4 W	32.8	0.09	541
von Baeyer	81.8 S	61.9 E	13.5	0.20	78
Wiechert	84.0 S	164.7 E	40.8	0.08	190
Wiechert E	83.6 S	176.0 E	20.9	0.12	111
Wiechert J	85.2 S	177.6 W	34.9	0.09	367
Wiechert P	85.1 S	151.8 E	38.6	0.08	67
Wiechert U	83.4 S	149.0 E	30.0	0.10	108

[a]According to the United States Geological Survey.
[b]Derived using data from Mazarico et al. (2011).

B | Annual Maximum Maps of Earthshine

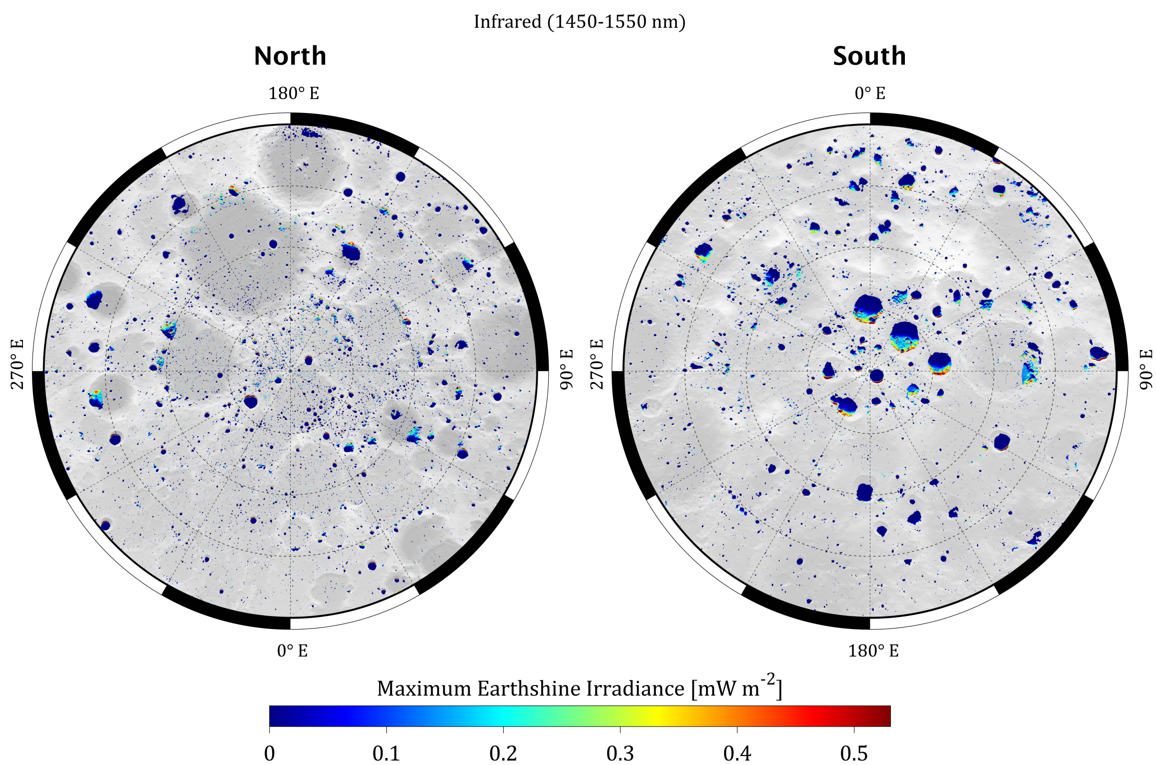

Figure B.1: Maximum Earthshine IR (1450-1550 irradiance (mW m^{-2}) received by areas of permanent shadow at the north and south pole of the Moon over an 18.6 year period.

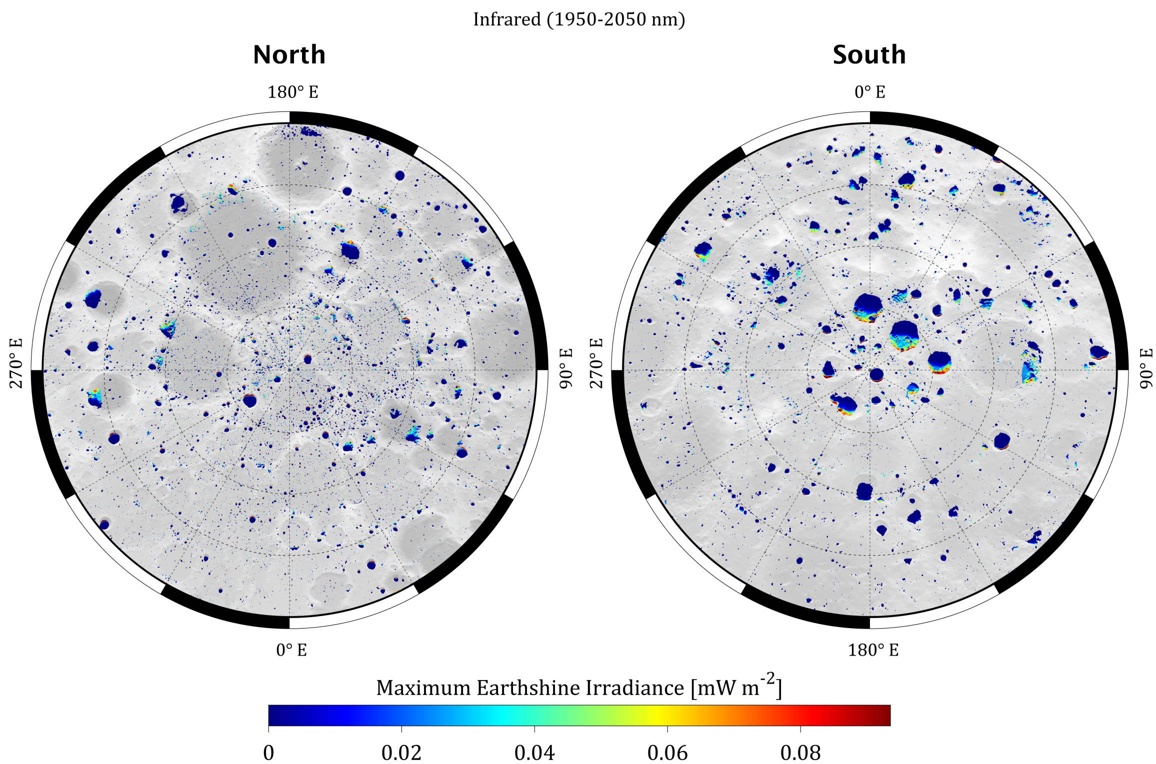

Figure B.2: Maximum Earthshine IR (1950-2050 irradiance (mW m^{-2}) received by areas of permanent shadow at the north and south pole of the Moon over an 18.6 year period.

C | Annual Mean Maps of Scattered Sunlight

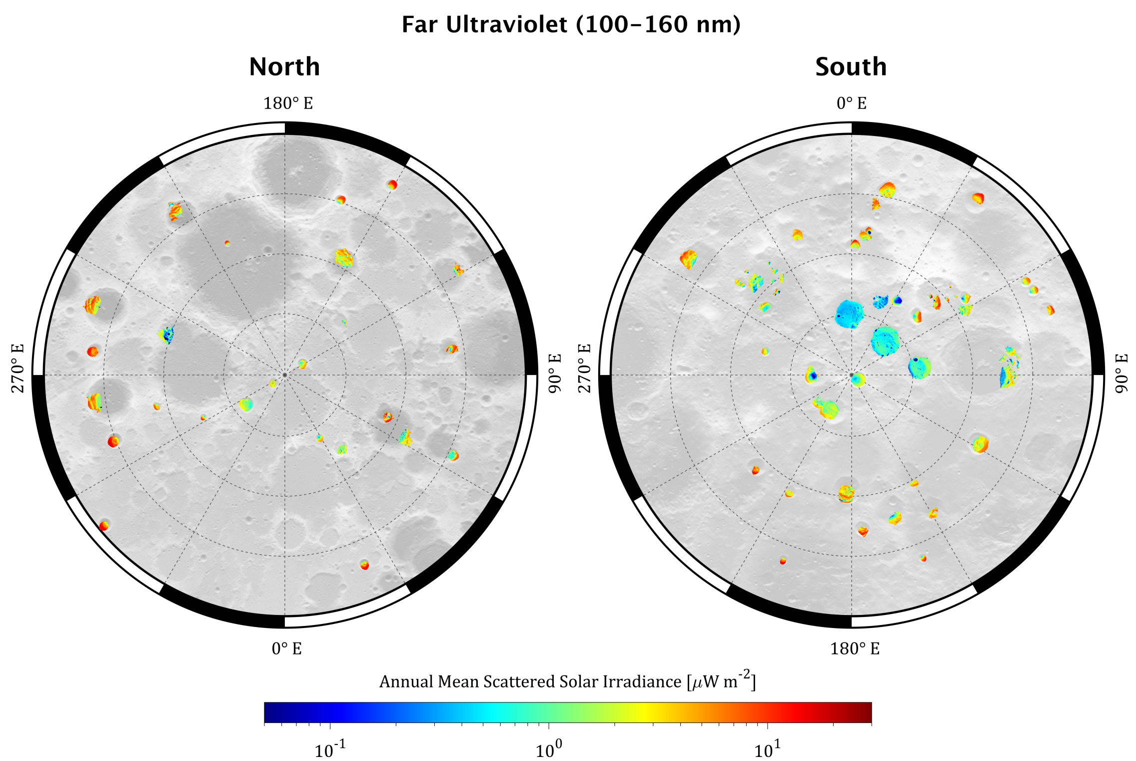

Figure C.1: Annual mean FUV (100–160 nm) scattered solar irradiance (μW m^{-2}) received by areas of permanent shadow at the north and south pole of the Moon.

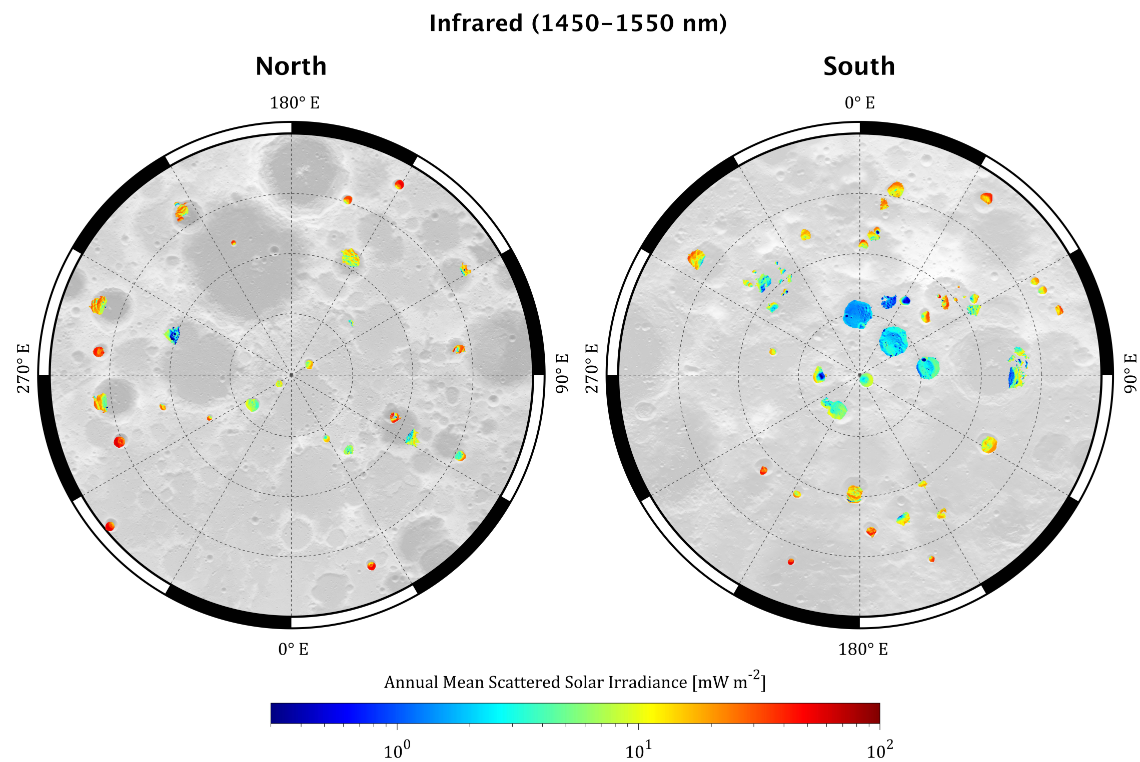

Figure C.2: Annual mean IR (1450–1550 nm) scattered solar irradiance (mW m^{-2}) received by areas of permanent shadow at the north and south pole of the Moon.

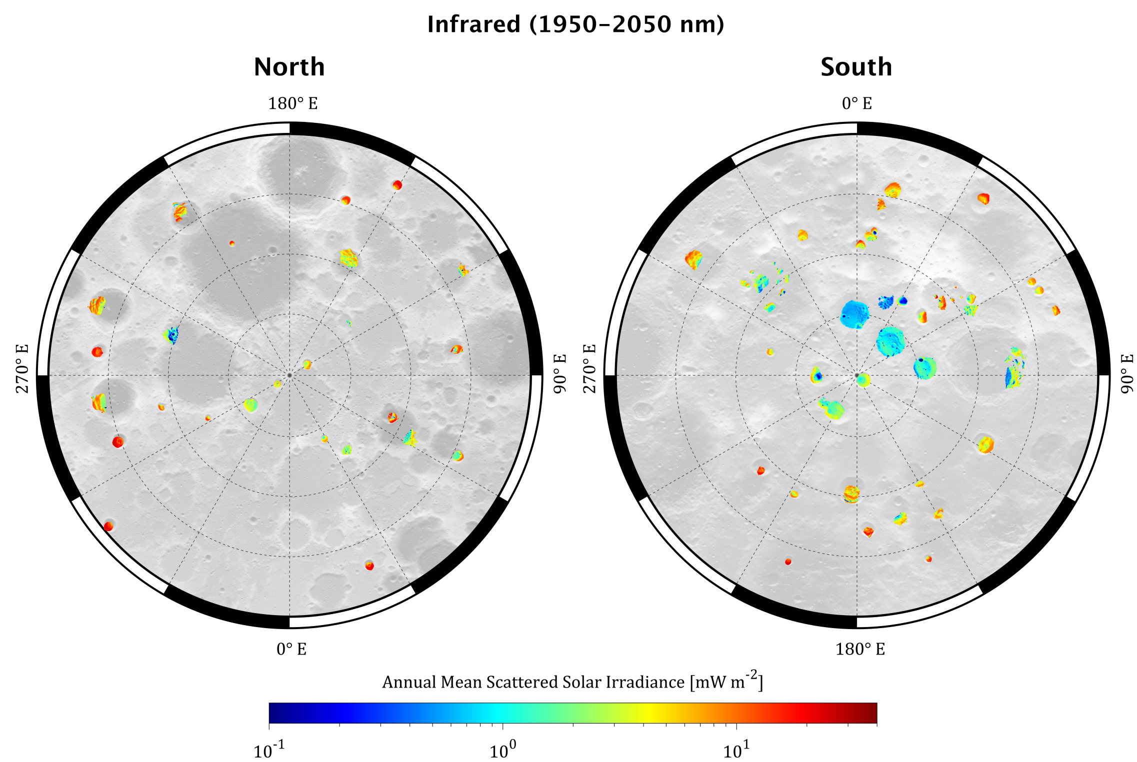

Figure C.3: Annual mean IR (1950–2050 nm) scattered solar irradiance (mW m^{-2}) received by areas of permanent shadow at the north and south pole of the Moon.

D | Model and Data Set Availability

D.1 Chapter 3 Models and Data Sets

The LOLA data products used throughout this work are archived on the Planetary Data System (PDS) and are specified as "version 3" data files; they can be accessed at: https://ode.rsl.wustl.edu/moon/index.aspx. The HEALPix scheme used to calculate the Earthshine illumination was created for MATLAB by Yousuke Naruse and is available at http://sufoo.c.ooco.jp/program/healpix.html. The Mie scattering code used to model the directional hemispheric albedo of water ice was based on the appendix material of Bohren and Huffman (2008) and written for MATLAB by Christian Maetzler; the code can be found at: https://omlc.org/software/mie/. The SORCE-SOLSTICE FUV solar irradiance data (Rottman, Woods, & Sparn, 1993) is made available at: https://lasp.colorado.edu/home/sorce/data/. All SPICE kernels used in this work were the most up to date versions at the time of writing (2020/2021) and can be accessed at: https://naif.jpl.nasa.gov/pub/naif/generic_kernels/. Pl

D.2 Chapter 4 Models and Data Sets

All Narrow Angle Camera images discussed in this chapter can be accessed at: http://wms.lroc.asu.edu/lroc/search. The Lunar Reconnaissance Orbiter SPICE data set is archived at: https://pds-geosciences.wustl.edu/missions/lro/.

D.3 Chapter 5 Models and Data Sets

The Diviner GCP (Global Cumulative Products) data, from which the global temperature maps of Williams et al. (2017) were derived, are available on the PDS and the rasters are made available at: diviner.ucla.edu. The SSR maps and the Monte Carlo model are archived in the Supporting Information of Kloos et al. (2019).

D.4 Chapter 6 Models and Data Sets

The Diviner polar seasonal temperature maps (Williams et al., 2019) are currently archived on the PDS and are available at: diviner.ucla.edu. The exospheric model used here can be found in the Supporting Information of Kloos et al. (2019).

D.5 Chapter 7 Models and Data Sets

The 1-D thermal model was written by Norbert Schorghofer and is made available at: https://github.com/nschorgh/Planetary-Code-Collection.